

Computational hemodynamics in cerebral aneurysms: Robustness of rupture risk indicators under different model assumptions

Øyvind Evju

December 18, 2016

Dissertation for assessment for Ph.D. at the
Faculty of Mathematics and Natural Sciences,
University of Oslo

Contents

1	Introduction	1
1.1	Cerebral aneurysms	1
1.2	Theory and modelling of aneurysm development	2
2	Modelling of cerebral blood flow	6
3	Aim of this thesis	13
4	Summary of papers	14
5	Related work	17
6	Limitations and future work	18
7	Papers	35
7.1	Paper I: A study of wall shear stress in 12 aneurysms with respect to different viscosity models and flow conditions	35
7.2	Book chapter: On the Assumption of Laminar Flow in Physiological Flows: Cerebral Aneurysms as an Illustrative Example	45
7.3	Paper II: Robustness of common hemodynamic indicators with respect to numerical resolution in 38 middle cerebral artery aneurysms	67
7.4	Paper III: Rupture prediction of cerebral aneurysms: a nationwide matched case-control study of hemodynamics at time of diagnosis	89

Acknowledgments

I am very grateful for the support and encouragement given to me by my main supervisor Kent-Andre Mardal, but also for the exciting opportunities I've been given through projects closely related to this Ph.D.-work. I would also like to express my gratitude to all my other supervisors: Martin Sandve Alnæs, Kristian Valen-Sendstad, Angelika Sorteberg and Hans Petter Langtangen. I would also like to thank all my collaborators, both formal and informal. This includes professor Alejandro Frangi and the people at CISTIB in Sheffield, who were very hospitable during my stay there in 2014. For heightening my understanding of the clinical approach to cerebral aneurysms, I must thank Søren Bakke at Rikshospitalet, Oslo, and Jørgen Isaksen and Torbjørn Skodvin at the University Hospital of Northern Norway.

I would also like to thank the people behind the FEniCS Project, for making an outstanding piece of software for solving partial differential equations. There seems to be no end to the possibilities.

My colleagues at Simula and in the BioComp-department have made the day-to-day routines far more enjoyable than it could have been. The open door policy have made it easy for me to get support, vent frustration, and celebrate my successes together with you.

Finally, a special thanks must go to my family, for all their help and support. You have been very understanding of my situation, and done all you can to help me reach my goals. The best support of all has come from my dear Torunn. Words cannot express what your limitless support has meant to me, when self-doubt and slow progress has been the daily tune. This dissertation wouldn't have been finished without you.

1 Introduction

1.1 Cerebral aneurysms

Cerebral aneurysms are abnormal dilations of blood vessels within the skull, that in rare cases may rupture and bleed. They are most common in the arteries in a part of the brains blood supply found at the base of the brain, known as the Circle of Willis. The blood flows through the Circle of Willis at a rate of approximately 0.6L/min [1], thus a rupture of an aneurysm here can cause a significant bleeding into or around the brain (a stroke).

Cerebral aneurysms occur in about 1-6% of the population [2], with more and more aneurysms discovered due to improvements and availability of advanced imaging techniques such as computer tomography and magnetic resonance angiography. Even though there is a high prevalence of cerebral aneurysms, the rupture rate is relatively low, with an incidence rate of about 6 per 100,000 people annually [3].

The causes of cerebral aneurysms are unclear, even though several risk factors have been identified. Smoking and hypertension have been identified as contributing factors, as have having an asymmetric Circle of Willis [4]. Women also have approximately 60% greater risk of developing cerebral aneurysms than men. There are also indications that genetics play a role, as for instance the rupture rate in the Finnish and Japanese population is greater than elsewhere [5], even though the prevalence rate is not [6].

Treatment of cerebral aneurysms was until the 1990s the domain of neurosurgeons, with the procedure of surgical clipping. This is a highly invasive procedure, where the skull is opened, and a clip is attached around the neck of the aneurysm. Since the introduction of Guglielmi detachable coils in 1991

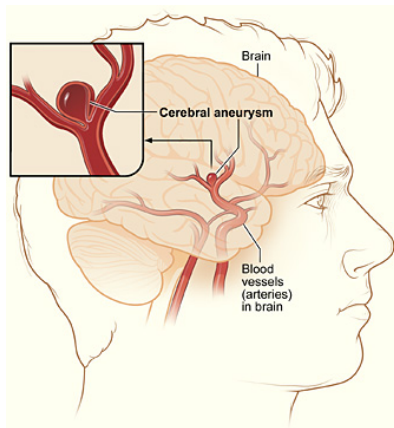


Figure 1: Visualization of a cerebral aneurysm at the internal carotid artery.

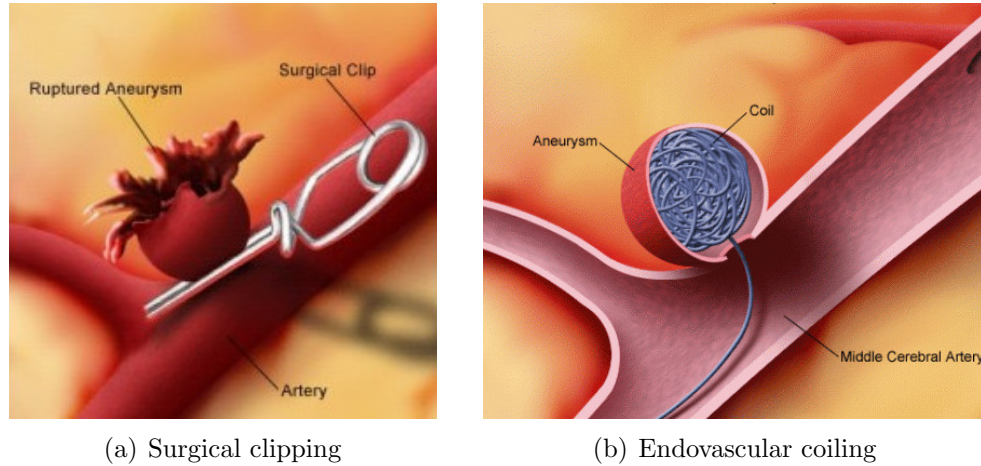


Figure 2: Illustration of the two main methods of cerebral aneurysm treatment. (Image courtesy of <http://www.columbianeurosurgery.org/conditions/aneurysm/>)

[7, 8], endovascular treatment has become more used, with either stents, flow diverters, or coils [9–11]. Treatment using coils and surgical clipping is illustrated in Figure 2.

Either treatment option carries risks, both of procedural complications and late effects. For ruptured aneurysms, the 1 year complications after treatment (death or moderate to severe disability) is reported to be as high as 27.2% [12]. The risks for unruptured aneurysms are lower, with an incidence rate of 6.3% [13]. The 1 year costs of either treatment is estimated to an approximate average of \$45,000 in the US [14]. Andaluz and Zuccarello [9] show a decreasing trend in the risk of mortality with time.

Due to the high incidence of unruptured aneurysms in the population, and the risks and costs associated with the treatment methods, determining which aneurysms to treat is critical.

1.2 Theory and modelling of aneurysm development

The pathogenesis of cerebral aneurysms are to a large degree unknown. Healthy arteries are built up in three layers, the intima, media, and ad-

ventitia. The innermost layer of the intima, bordering the blood flow, are the endothelium. The endothelial cells sense shear forces, and signals the smooth muscle cells of the media to expand and contract in response to the blood flow, in a process known as mechanotransduction [15]. Exactly how this process is controlled, is only partly understood. However, with the shear forces too high [16], too low [17], or with large tangential gradients[36] this process is disturbed, and an inflammatory response causing cell death may occur in the vessel wall. This can typically happen at bifurcations of the cerebral circulation, areas often associated with cerebral aneurysm initiation or growth [18, 19]. In an already established aneurysm, it has been shown that smooth muscle cells are often missing, as is the endothelial layer [20].

Once an aneurysm forms, it grows to reach an apparent stable state. Nonetheless, some aneurysms are unstable, and continue to grow and eventually rupture. Being able to discriminate between stable and unstable aneurysms is considered an important research question.

Ruptured aneurysms are often larger than their unruptured counterparts, but due to the rarity of large aneurysms, most ruptured aneurysms are small [13, 21–23]. This suggest that size alone is not a sufficient criteria for predicting an imminent rupture event. Because of this, other factors including metrics derived from morphology and hemodynamics have been attracting attention ([24–34]), primarily through identifying correlations between different metrics and aneurysm rupture state.

The biological response in the vessel wall to hemodynamics is not independent, but is connected to a multiplum of other factors. As illustrated in Figure 3, the interactions between aneurysm risk factors are many and complex. As the development of an aneurysm is longitudinal (spanning from months to years), different factors are altered, and might trigger different conditions under which aneurysms are prone to growth or rupture. Within Cebra and Raschi [4], the authors have done a review of the literature on risk factors of aneurysms. Although they point to many different factors, they do however highlight the importance of hemodynamics, and the need for large, multi-center studies, and the relevance of studies with established correlations between hemodynamic factors and aneurysm rupture. As they state, *“although correlation does not imply causation, understanding the causes of aneurysm development and progression may help us understand the observed correlations”*. It is clear from this that hemodynamics must be interpreted

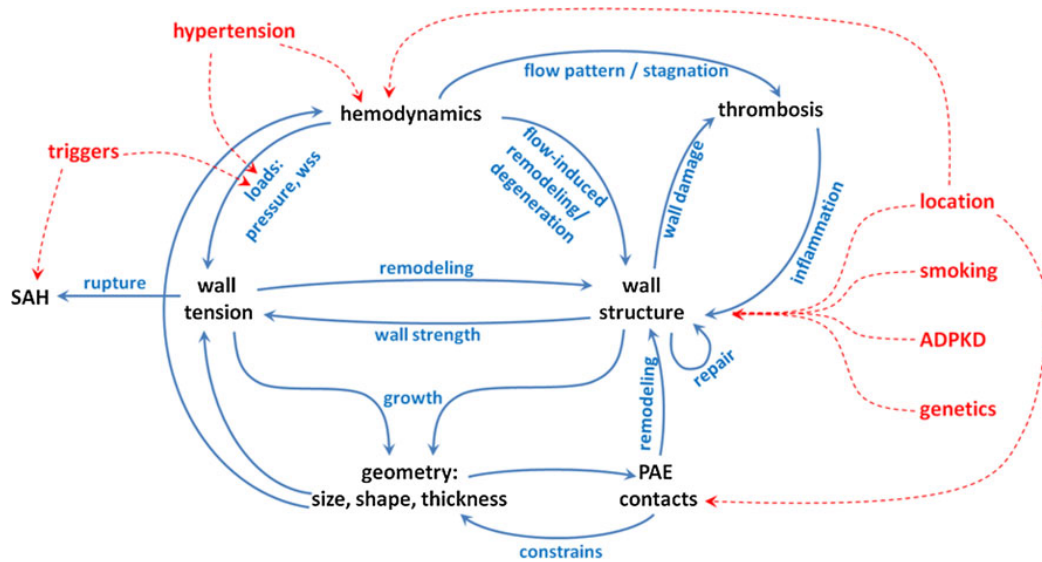


Figure 3: Illustration of the complexity of cerebral aneurysm rupture (SAH) pathogenesis (reprinted with permission from Cebal and Raschi [4])

in context of other factors, such as aneurysm location, wall structure, disposition to aneurysms through e.g. smoking or hypertension, and aneurysm geometry in order to be fully understood.

The potential causality of hemodynamics in cerebral aneurysm development, and eventual rupture, are reviewed by Meng et al. [35]. They hypothesize two possible pathways for an aneurysm to develop, one being high wall shear stress (WSS) and positive WSS gradients, the other being low WSS and high oscillatory shear index (OSI). High WSS and positive gradients are often associated with an impingement zone (where a concentrated “jet” impinges the vessel wall). A resulting pathologic vessel wall may arise from the mural cells, by increased expression of matrix metalloproteinase and loss of internal elastic lamina, but not necessarily damaged endothelium [36]. This is often associated with aneurysm initiation at bifurcations, but could also happen in established saccular aneurysms. This hypothesized pathway may lead to large, thick-walled aneurysms [35]. As an aneurysm develop, the hemodynamic environment inevitably changes, and may trigger the second proposed pathway, caused by low WSS and high OSI, seen in aneurysms with slow, recirculating flow, or disturbed flow [35]. This is known to cause inflammatory

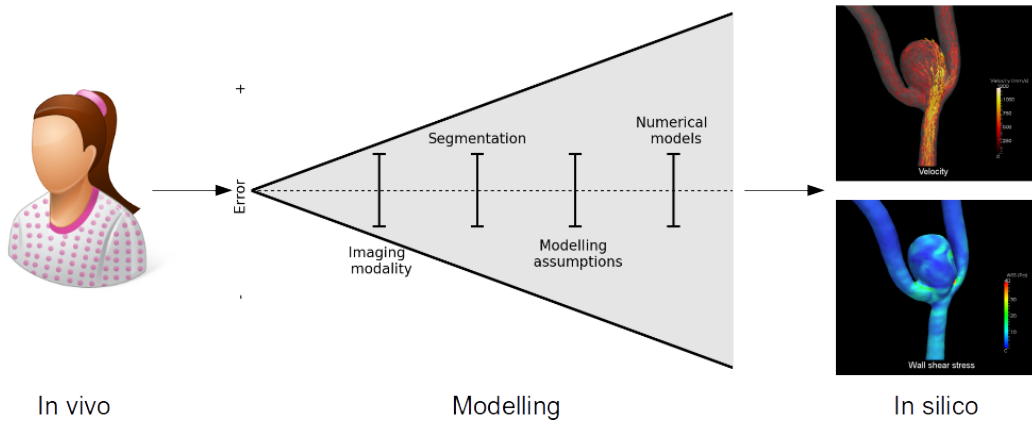


Figure 4: Illustration of the steps taken to model cerebral blood flow, and the potential error propagation in the modelling step.

responses in the endothelium, which facilitates leukocyte infiltration of the wall, causing increased production of MMP, and degrade the extracellular matrix [36]. This is hypothesized to lead to small, thin-walled aneurysms [35].

As the rupture event is caused by tensile stresses not sustainable by the wall, the study of different WSS-derived hemodynamic indicators are only suitable for estimating the “rupture potential” [35]. WSS-induced responses in the wall may leave the aneurysm in a fragile state, where sudden increases in blood pressure caused by for example exercise or emotional excitement, may trigger the rupture event [35]. The fact that the vessel wall structure is essential, has triggered studies on vessel wall mechanics, often in combination with blood flow simulations. For example, Cebal et al. [37], showed that a solid model for the vessel wall can be combined with blood flow simulations to give insight into the effects of wall thinning and wall stiffening/softening. They demonstrate that the location of rupture in nine aneurysms were best identified by a model with thin, stiff walls, in areas of high WSS.

2 Modelling of cerebral blood flow

Studying the hemodynamics can not be done accurately with current imaging tools, due to insufficient resolution of the images, and the noise averaging over many cardiac cycles. This is in particular valid when considering the WSS, as the blood flow gradient at the wall is required. Using computational fluid dynamics (CFD) to study the problem, researchers are able to obtain the flow field with arbitrary resolution in both space and time, at low costs and minimal disturbance to the patient.

This is a field that has attracted a lot of attention in recent years, as computational power has increased and the cost has decreased, and methods and software for both simulations and segmentation have been developed and improved. From early 2D idealized models (e.g. [38, 39]), the field has advanced through 3D idealized geometries (e.g [40]) to large cohort quantitative studies of patient-specific aneurysm models ([27, 28, 41, 42]). These large cohort studies have reached different, and partly conflicting results with regards to what kind of quantities are important for predicting aneurysm rupture. Schneiders et al. [43] reported that hemodynamics does not seem to provide any additional information over traditional parameters, however, other studies suggest otherwise [28, 44].

These conflicting and inconclusive results has resulted in some skepticism, and a debate about CFD as a tool for predicting aneurysm rupture ([45, 46]). In a response by Cebal and Meng [47], the authors argue that the conflicting results might be down to the complexity of the problem, and highlight that *“we need to facilitate the clinical use of computational tools by making them more user-friendly, streamlined, and efficient”*.

Besides the problem of risk prediction, CFD have also been used to simulate the hemodynamic effects of different treatment methods. Several studies have focused on the hemodynamics in coiled aneurysms [48–50], as well as on the hemodynamics around stents and flow diverters [51–56].

In the process from the unknown in vivo blood flow, there are many steps to obtain a simulation, all carrying inherent uncertainty and sources of error, as illustrated in Figure 4. Below follows a brief discussion on the sources of variability of different typical assumptions made in computational studies.

Imaging modalities and segmentation Several imaging techniques are available for volumetric imaging of cerebral vasculature. Most commonly applied are 3D rotational angiography (3DRA, “gold standard”), magnetic resonance angiography (MRA) and computed tomography angiography (CTA). Regardless of technology, the resolution is still insufficient to properly resolve the finer details of the cerebral vasculature. The typical voxel size¹ of images obtained with these technologies are typically of the order 0.2-0.5mm. In comparison, the diameter of the main arteries in and around the circle of Willis range from 4-6mm (internal carotid artery) [57] to 1.5mm (A2, ophthalmic artery) [58]. In addition, several smaller arteries originate from the larger arteries, with diameters less than 1mm [59].

For different scans of the same subject (and same method) Bijari et al. [60] reported a variability of the area of the larger arteries internal, common, and extracranial carotid artery of 5-8%. They concluded that the carotid bifurcation could be accurately characterized even with suboptimal images.

Poethke et al. [61] reproduced a phantom silicon model of a basilar tip aneurysm with three different image modalities (MRI, CT, 3DRA). They reported mean distances of the segmented surfaces of 0.097mm, 0.242mm and .10mm for the MRI, CT and 3DRA images respectively. The computed mean WSS of each model revealed errors of 3% (3DRA), 10% (MRI) and 25% (CTA) compared to the phantom model.

In Geers et al. [62] the variability of 3DRA and CTA imaging, was investigated using CFD. They studied 4 patient models with a total of 10 aneurysms, imaged with both modalities within a 3-day interval. They reported a variability in the mean WSS as high as 44.2%. They also highlighted the large variations in neck width, with the neck width in the CTA models an average of 33% wider. However, the qualitative blood flow characteristics were found to agree excellent.

Accurately determining the neck region of the aneurysm is also considered important to correctly determine hemodynamic indicators. Piccinelli et al. [63] introduced an automated method to do this, but many studies have either performed manual delineation or not mentioned the techniques used. The effects of this is insufficiently studied, but it could likely affect the results of for instance maximal WSS, since the location of the maximum is often

¹Voxel size denotes the edge length of the cubes in the images.

located close to the neck of the aneurysm [41].

Model assumptions For computational modelling of blood flow, several assumptions has to be made. Patient-specific data besides the geometry is rarely available, and therefore usually set from available literature data. How these are chosen will obviously affect the simulation results and computed hemodynamic indicators.

Regardless of which computational model is chosen, the 3D computational domain has to be limited because of computational resources. This implies that boundary conditions must be chosen to as accurately as possible reflect physiological conditions. At the inflow region, this is typically done by specifying flow rates. In [64], the authors describe a flow-area relationship between measured flow rates and cross-sectional areas of vertebral arteries and the internal carotid arteries, together responsible for most of the cerebral blood supply. They propose a power-law relationship between the flow rate Q and area A , of $Q = kA^n$, with $n=1.84$ and $k=48.21$ (area in cm^2). Valen-Sendstad et al. [65] compared a "square-law" (flow rates scale with the radius squared) and a "cube law" (flow rates scale with the radius cubed). By using the Aneurisk database, they found the least variability along the internal carotid artery using the square law, and thus suggest scaling flow rates with the area. Other common modeling choices include constant flow rates (e.g. [28]), constant shear stress (e.g. [27, 62]), or coupling with a 1D-model of the full vascular network [66]. In [67], the authors performed a comparison of different flow rate estimations, comparing 1D models and cube law models with phase contrast magnetic resonance imaging (PCMRI) measurements. They revealed median differences in normalized average WSS of 11-20.5%, 46-69% in maximal WSS, and 17.5-23.5% in OSI.

Because of the suspension of red blood cells, and their interaction, blood behaves as a non-Newtonian shear-thinning fluid. However, these effects are thought to have little effect in large arterial blood flow modelling, such as in the circle of Willis [68]. In [69], the effect on typical hemodynamic indicators were studied using three different non-Newtonian viscosity models, and compared to a typical Newtonian constant viscosity model with the same high-shear asymptotic viscosity on 12 aneurysm models. Within, we found that the hemodynamic indicators studied (average WSS, max WSS and area of low shear, LSA) all correlated strongly under different viscosity

models (correlation coefficient greater than 0.997). Xiang et al. [70] studied three viscosity models (two non-Newtonian) on three different geometries. They found that the Newtonian model predicted higher WSS in regions of slow flow, and that this could underestimate rupture risk based on previous studies by them, indicating that regions of low shear were associated with aneurysm rupture [28]. In a more recent study [71], the authors studied the differences between a Newtonian and a Casson rheological model on 10 patient models of aneurysms with lobulations. They concluded that WSS characterization remained unchanged, and, although the Casson model consistently produced higher WSS in regions of high WSS, they did not find any statistical significance. They concluded that “[t]here is no evidence that Newtonian model overestimates WSS”.

Since aneurysm rupture occur when the mechanical stresses in the vessel wall exceed its strength, the fluid-induced WSS is not sufficient to predict rupture. To estimate the stresses within the wall, the fluid equations needs to be coupled with a (hyper-) elastic model for the vessel wall. The wall tension and displacement is heavily influenced by the blood flow, but is usually disregarded in computational hemodynamics. The fluid-structure interaction (FSI) between the vessel walls and the blood flow require more complex computational models, and are generally much heavier to compute. These computational models also introduce new parameters, such as the wall thickness and structural properties of the wall, as well as more advanced outflow boundary conditions. Several studies have attempted to quantify the effects of assuming rigid walls, by considering both rigid walls and FSI, and looking at the resulting flow patterns and WSS. Bazilevs et al. [72] studied four different aneurysms, and reported rigid wall WSS as high as 152% of the FSI-model. In [73], they also highlighted the need for estimating wall tension, as the results showed high wall tension at locations where aneurysms typically rupture. Torii et al. [74] investigated the influence of the rigid wall assumption by studying two realistic geometries with both FSI and rigid wall simulations. They found an increase in max WSS of up to 50% in the rigid wall models. They also commented that due to the deformation of the aneurysm wall, the flow jet were directed more directly at the aneurysm apex. In [75], two different saccular aneurysm geometries were considered, with two FSI models and rigid walls. In max WSS, they found variations in the rigid wall model between -26% to 59%. For aneurysms in particular, another problem arises as the wall properties of unruptured aneurysms typi-

cally differs from the healthy artery, as well as between different unruptured aneurysms [76]. In [77], the authors studied two different wall models for the aneurysm wall, by using a wall thickness of 0.3mm and 0.05mm (pathological wall). They found a 1.5-2 times larger maximum displacement using the pathological wall model. For the same model, they also found that mean WSS was 37.5% to 65.9% smaller. They also remarked that the regions of low WSS were more pronounced in the pathological wall model.

Murray's principle of minimal work [78] state that volumetric flow rate of blood in the arterial network is proportional to the cube of the radius. It was later restated by Zamir [79] as an hypothesis of constant shear, and a typical value of 1.5Pa is commonly assumed, based on the work of Malek et al. [80]. This has been used in many computational works to estimate both inlet and outlet flow rates (e.g. [27, 71, 81, 82]). For cerebral arteries, the radius ratio has been shown to follow this principle [83]. Recently, Cheng et al. [84] challenged this assumption, stating that the assumption of a constant WSS of 1.5Pa in straight vessels is incorrect, demonstrating that the WSS is not constant throughout the vascular tree. They also state that their findings suggest that the WSS scale with the inverse of radius, meaning that the flow rate is better supported by an r^2 -law than an r^3 -law.

The effects of the flow division at bifurcations can alter the hemodynamics. Besides the principle of minimal work, boundary conditions commonly used are traction-free boundary conditions, resistance boundary conditions, impedance boundary conditions, and Windkessel models. In [69], the differences between traction-free and resistance boundary conditions were studied in 12 realistic geometries. We found that the ranking of typical WSS quantities were not affected by changed boundary conditions. Jansen et al. [85] compared traction-free and patient-specific boundary conditions obtained from 4D PCMRI. Out of 36 geometries studied, they found qualitative differences in 21. They also found statistically significant differences in mean and max WSS values, but not OSI.

Laminar flow is usually assumed in cerebral aneurysms, due to the Reynolds numbers being far lower than the transitional threshold of 2300 in straight tubes. However, the pulsatile nature of the flow and the complex geometry, in particular the sudden expansion of a saccular aneurysm, might significantly alter this critical threshold [86, 87]. Valen-Sendstad et al. [88] found that high-frequency velocity fluctuations were found in bifurcation aneurysms,

but not sidewall aneurysms, under steady (peak systolic) flow, with “*non-negligible fluctuations up to about 900 Hz*”. In [89], the authors showed that high-frequency effects could occur in aneurysms, with energy carrying frequencies as high as 60, 313 and 923Hz at Reynold numbers 250, 500 and 1000, respectively, for a specific geometry. To capture these effects require the use of minimally dissipative schemes, that is at least second order convergent in time and space [90]. Resolving these effects can be computationally expensive, and is therefore less attractive for clinicial use. Furthermore, their effects on aneurysm development, if any, is unclear. Varble et al. [91] studied 56 aneurysms at Reynolds numbers 287 ± 51 , at constant flow rates. They found instabilities in 8 out of 56 aneurysms, but did not find any evidence relating fluctuating kinetic energy to aneurysm rupture.

Numerical models Several numerical models are available to compute the hemodynamics in large arteries. Most are based on the solution of the Navier-Stokes equations, and some are coupled with (hyper-) elasticity models for the arterial walls. Additionally, some novel methods include multi-scale approaches to compute blood cell interactions (e.g. [92, 93]) and thrombus formations (e.g. [94, 95]). Furthermore, fluid-solid-growth models have appeared in order to compute the remodelling of arteries (e.g. [96, 97]).

For the rigid wall fluid dynamics, Steinman et al. launched a challenge for the ASME 2012 Summer Bioengineering Conference [98]. The challenge was motivated by the study by Cebal et al. [51], which attracted attention to the computed pressure drops [99]. The challenge received 27 complete solution for Phase 1, of which 17 used commercial solvers, 5 open source solvers and 5 in-house solvers. The solver methodologies were distributed as 19 finite volume solvers, five finite element solvers, two spectral element solvers, and one finite difference solver. In addition, *in vivo* experiments were performed on the provided geometry. With provided flow rates, viscosity and density, the resulting computed pressure drops “*remarkably consistent, typically differing by less than 10%*”. However, on closer inspection of the flow fields, the challenge organizers observed a wider variation. They chose not to investigate WSS.

The numerical model for rigid wall CFD is also sensitive to modelling choices, such as first- vs second-order accurate schemes, boundary layers, as well as stabilization techniques. In [100], the authors considered the effects of a first

order accurate stabilized scheme with 1,000 timesteps per cycle on coarse meshes, compared to a second-order accurate scheme with 20,000 timesteps per cycle and high spatial resolution. Based on their results, they suggest that the qualitative effects of CFD solution strategy are greater than the assumptions of boundary conditions, Newtonian viscosity models, rigid wall modelling, and imaging techniques. They did however note, that their coarse resolution might be sufficient for fast CFD simulations desired for clinical usage. Khan et al. [90] compared different resolutions in time and space using a “*high-fidelity CFD solver*” as well as a stabilized, first order solver. They found that the high-fidelity solver was able to capture the qualitative flow at surprisingly coarse resolutions, and that computation times of <10 hours could be sufficient to provide accurate solutions. Highlighted was also the need to properly understand the capabilities and limitations of different CFD approaches.

For FSI-applications, many methods have been devised (e.g. [101, 102]). Most of these are very costly compared to rigid wall CFD. However, new approaches decoupling the fluid and structure solves may simplify the computation of FSI [103, 104], making it more feasible to perform simulations on larger patient cohorts.

Study designs Most computational studies to date focus on the models ability to discriminate ruptured from unruptured aneurysms *retrospectively*, with a few exceptions [31, 105–108]. This has been done because of availability of data, and the assumption that the rupture event does not alter the aneurysm morphology. It is also unclear to what degree the authors performing the computations are blinded to the medical outcome of each aneurysm. Furthermore, it is unclear at what stage in the process the study design is finalized, and the hemodynamic indicators to be computed are determined. With the increasing number of hemodynamic indicators available, this methodology is increasingly important, to avoid so-called data-dredging. With the amount of data available, it is often possible to identify correlations, not necessarily related to any causal effect.

In recent years, it has also been observed that the geometry of an aneurysm might change significantly when ruptured [109]. This highlights the need for prospective studies, and is also of clear interest to the clinicians, who make follow-up strategies from the time of diagnosis. The PhD thesis of Retarekar

[105] describes a methodically accomplished analysis, in that the analysis was done prospective, with the author blinded to medical outcome. With 25 pre-selected hemodynamic indicators and 198 aneurysms “chosen by physicians to be kept under watchful waiting”, the author found no statistical significant differences between growing and stable aneurysms.

Brinjikji et al. [110] studied 12 pairs of unruptured aneurysms, with each pair consisting of one stable, and one unstable aneurysm, matched on size. They identified LSA as 2.26 times larger in unstable aneurysms, as the only significantly different computed metric between the two groups. These are similar results to those of a similar study presented in this thesis (see Paper III).

3 Aim of this thesis

This thesis aims to address some of the common assumptions of computational studies, and their effects on the hemodynamic indicators suggested as important for aneurysm development. The previous quantitative studies have undoubtedly required large computational resources, and exhausting all possible sources of error in the current paradigm not feasible in a rigorous manner. This became more clear when studies and comments such as [45, 47, 98] highlighted both the apparent contradictory results of these studies, as well as the large variability in computational hemodynamics from several studies.

In this thesis, we have found that modelling assumptions such as viscosity models or boundary conditions have little impact on the ranking of common hemodynamic metrics. We have also demonstrated that the (often implicit) assumption of laminar flow could underestimate the complexity of the flow, by failing to capture high-frequency, energy carrying flow instabilities. We have investigated the robustness with respect to numerical resolution, of hemodynamic indicators from the two most frequently-cited studies in the field. Here we found that for quantitative studies, strict convergence are not essential, and that some of the hemodynamic indicators require higher resolution to be converged than others.

In addition, a nation-wide matched case-control study was conducted with

controls matched on a variety of factors, with data from both cases and controls were collected from time of diagnosis of an unruptured aneurysm. Here, we again investigated well-known hemodynamic indicators, and found that a high LSA could be an early predictor of later aneurysm rupture.

4 Summary of papers

Paper I: A study of wall shear stress in 12 aneurysms with respect to different viscosity models and flow conditions

Øyvind Evju, Kristian Valen-Sendstad and Kent-Andre Mardal. Journal of Biomechanics 46 (16), 2802-2808

When performing CFD of blood flow in cerebral aneurysms, the viscosity is usually assumed Newtonian in behaviour, even though it is well known that blood exhibits shear thinning properties. In addition, patient-specific boundary conditions for pressure or flow velocities are at best inaccurate, and usually not available at all. This is required to determine how much flow enters the computational domain, but perhaps even more important is that it can highly affect the flow distribution in a branched geometry.

In this paper, we present 4 different viscosity models and 3 different boundary conditions applied to a set of 12 aneurysms geometries. We studied three typical indicators of rupture risk to assess the effects of typical variations in these assumptions.

We found a strong correlation between all sets of parameters, suggesting that in the current paradigm it is unnecessary to complicate the model any more than what is currently the case in most published work in the area.

For all parameters we found a strong correlation in the hemodynamic indicators, when varying a single parameter. This suggest that the sensitivity to different viscosity models or boundary conditions is low, and that changing any of these does not alter the ranking of the cases.

Book chapter: On the Assumption of Laminar Flow in Physiological Flows: Cerebral Aneurysms as an Illustrative Example

Oyvind Evju and Kent-Andre Mardal. In Modeling the Heart and the Circulatory System, volume 14, pages 177– 195. 2015.

Most flows in our human body is believed to be laminar, except for in the heart and aorta, in healthy individuals. A good reason for this is that turbulence introduces extra friction and hence transport in the laminar regime is energy efficient compared to the turbulent regime. Furthermore, laminar flow in arteries ensures a healthy mechanotransduction mediated through the endothelial cells.

Transition to turbulence in steady pipe flow occurs at Reynolds number (Re) 2300, while fully developed turbulence is obtained around $Re=4000$. The Reynolds number in biophysiological flows is usually far below this, and laminar flow is therefore assumed. However, both the pulsatile nature of the flow and deviations from straight pipe geometry might introduce transition to turbulence at lower Reynolds numbers.

This chapter is devoted to a review on the assumption of laminar flow and we use blood flow in cerebral aneurysms as an illustrating example. We also review clinical and biomechanical findings suggesting that blood flow in cerebral aneurysms in some cases might transition.

The raw 4D PCMRI-data, as well as the meshes and scripts used for the simulations in this chapter can be found at <http://folk.uio.no/oyvinev/dog/>.

Paper II: Robustness of common hemodynamic indicators with respect to numerical resolution in 38 middle cerebral artery aneurysms

Submitted

The effects of resolution on hemodynamic computations have received attention in recent years, highlighting that most of the larger CFD studies

on cerebral aneurysms are underresolved [100]. The implications of this is yet unknown, as it is unclear how highly resolved simulations would effect quantitative studies.

In this paper, we investigate the robustness of the hemodynamic indicators suggested to be related to aneurysm rupture in the two most frequently cited studies in the field, namely Xiang et al. [28] and Cebal et al. [27], in addition to spatial and temporal gradients for completeness.

Thirty-eight geometries of middle cerebral arteries were collected from the @neurist database. Simulations were performed at two different refinements, representing coarse and high resolution. The fine resolution was done using 23000 timesteps per cycle and an effective mesh resolution of 0.065mm.

Our main findings suggested that for quantitative studies, all studied hemodynamic indicators were sufficiently resolved at the coarse resolution, even though several outliers were visible for several of the indicators, most notably OSI, LSA, max WSS, WSS gradient and time-derivative WSS. The indicators mean WSS, viscous dissipation ratio (VDR), inflow concentration index (ICI), and shear concentration index (SCI) appeared to be robust with respect to the numerical resolution. This suggest that care should be taken when qualitatively assessing the different indicators, in for example clinical situations.

Paper III: Hemodynamic and morphological cerebral aneurysm rupture predictors at time of diagnosis: a matched case-control study.

Submitted

Hemodynamic rupture predictors in cerebral aneurysms are usually computed using post-rupture imaging data. This might be insufficient, since the rupture event might alter aneurysm shape and hemodynamics. In this study, we have used aneurysms collected during a 10-year period from all Norwegian university hostpitals treating cerebral aneurysms and subarachnoid hemorrhage.

Twelve cases that ruptured at a later point were identified as suitable for the study, with two unruptured controls per case (unruptured and untreated).

Controls were matched by patient age and sex, as well as aneurysm location and size. Segmentations and simulations were performed on all thirty-six geometries, and previously identified hemodynamic rupture indicators were computed.

We found that of the 11 hemodynamic indicators studied, the LSA was the only indicator that showed a significant difference between the two groups, with lower values in the control-group.

Our findings demonstrate that the hemodynamics in unruptured cerebral aneurysms at the time of diagnosis, are different between aneurysms that later rupture, and aneurysms that remain unruptured. However, our findings are insufficient for a conclusive rupture prediction at the time of diagnosis.

5 Related work

During the work of this thesis, I've also been involved in other projects, that have resulted in two submitted articles. The first article is entitled *Numerical study of intrathecal drug delivery to a permeable spinal cord: effect of catheter position and angle* and submitted to *Computer Methods in Biomechanics and Biomedical Engineering*[111]. In this work we study the effect of catheter position and angle in intrathecal drug delivery, with respect to the simulated drug concentration in the spinal cord.

The second article is more closely related to my work in this thesis, namely on data assimilation of blood flow. This article, entitled *Variational data assimilation for transient blood flow simulations*, has been submitted to SIAM Journal on Scientific Computing [112]. The study demonstrates a promising tool for variational data assimilation (4DVar) of blood flow, using 4D PCMRI data, and the open source softwares *dolphin-adjoint* [113] and *FEniCS* [114].

While working on this thesis, I've also presented both parts of this thesis and other works at ASME Summer Bioengineering Conference 2012 in Fajardo, Puerto Rico (poster), the Intracranial Stent Meeting 2012, in Madison, Wisconsin (short podium talk), and at the Modelling of Physiological Flows 2013, at Sardinia, Italy (podium talk).

In addition, the work on this thesis has also resulted in two software pack-

ages. *cbcpost* is a feature-rich postprocessing software based on FEniCS. The software relies on the concept of *fields*, which describes a quantity derived from the solution of a time-dependent problem. Full modularity of the fields means that all fields can be combined, to compute more complex derived fields. The structure of the software also allows for easy verification of solvers for any problem, by allowing batch simulations over a set of parameters. In addition, it provides a *cbcdashboard*, that allows for easy inspection of computed solutions.

cbcflow is a package designed for CFD-computations, and relies on *cbcpost* for postprocessing. Within *cbcflow* is a highly efficient Navier-Stokes solver for incompressible flows, following the principles of the software package *Oasis* [115]. The software has also taken advantage of the modular design of *cbcpost* to implement many of the typical hemodynamic indicators considered in literature.

Both *cbcpost* and *cbcflow* is fully compatible with MPI, and has been successfully tested on hundreds of cores. The main components of *cbcpost* and *cbcflow* is implemented in Python, with the exception of performance-demanding computations and computations relying on software not easily available through Python, which are implemented in C++.

Both packages are open source (licensed under the GNU LGPL, version 3 or any later version), and available from https://bitbucket.org/simula_cbc.

6 Limitations and future work

Some of the limitations of this thesis are obvious from the discussion in section 2. Only a few selected assumptions are studied for their effects on the hemodynamics, and the combined effects have not been addressed, simply due to the vast parameter space that would need to be explored. In addition, some of the results of this thesis would likely be stronger with larger data sets used for analysis.

Due to the many error sources of CFD, it likely requires large patient cohorts to eliminate the inherent noise in the results. If the error could be estimated or controlled, the size of the patient cohort required could likely be dramatically reduced, and thus the required computational resources. With the

increased amount of data collection, and with 4D imaging, new opportunities present themselves, in the directions of for example machine learning and data assimilation. In the current paradigm however, computational hemodynamics is still some way off of being a widespread tool used in the clinic. Automated approaches are desirable for both the image segmentation, boundary conditions, and simulations, in order to limit inter-operator variability, and provide larger amounts of comparable data for possible meta-analysis.

References

- [1] J. Hendrikse, A. F. v. Raamt, Y. v. d. Graaf, et al. Distribution of cerebral blood flow in the Circle of Willis. *Radiology*, 235(1):184–189, 2005.
- [2] G. J. E. Rinkel, M. Djibuti, A. Algra, and J. v. Gijn. Prevalence and risk of rupture of intracranial aneurysms: A systematic review. *Stroke*, 29(1):251–256, 1998.
- [3] F. H. H. Linn, G. J. E. Rinkel, A. Algra, and J. v. Gijn. Incidence of subarachnoid hemorrhage role of region, year, and rate of computed tomography: A meta-analysis. *Stroke*, 27(4):625–629, 1996.
- [4] J. R. Cebral and M. Raschi. Suggested connections between risk factors of intracranial aneurysms: A review. *Annals of Biomedical Engineering*, 41(7):1366–1383, 2013.
- [5] M. J. H. Wermer, I. C. v. d. Schaaf, A. Algra, and G. J. E. Rinkel. Risk of rupture of unruptured intracranial aneurysms in relation to patient and aneurysm characteristics: An updated meta-analysis. *Stroke*, 38(4):1404–1410, 2007.
- [6] M. H. M. Vlak, A. Algra, R. Brandenburg, and G. J. E. Rinkel. Prevalence of unruptured intracranial aneurysms, with emphasis on sex, age, comorbidity, country, and time period: A systematic review and meta-analysis. *The Lancet Neurology*, 10(7):626–636, 2011.
- [7] G. Guglielmi, F. Viñuela, J. Dion, and G. Duckwiler. Electrothrombolysis of saccular aneurysms via endovascular approach. Part 2: Preliminary clinical experience. *Journal of Neurosurgery*, 75(1):8–14, 1991.
- [8] G. Guglielmi, F. Viñuela, G. Duckwiler, et al. Endovascular treatment of posterior circulation aneurysms by electrothrombolysis using electrically detachable coils. *Journal of Neurosurgery*, 77(4):515–24, 1992.
- [9] N. Andaluz and M. Zuccarello. Recent trends in the treatment of cerebral aneurysms: Analysis of a nationwide inpatient database. *Journal of Neurosurgery*, 108(6):1163–9, 2009.

- [10] O. N. Naggara, P. M. White, F. Guilbert, et al. Endovascular treatment of intracranial unruptured aneurysms: Systematic review and meta-analysis of the literature on safety and efficacy. *Radiology*, 256(3): 887–97, 2010.
- [11] W. Brinjikji, M. H. Murad, G. Lanzino, et al. Endovascular treatment of intracranial aneurysms with flow diverters: A meta-analysis. *Stroke*, 44(2):442–447, 2013.
- [12] A. Molyneux. International Subarachnoid Aneurysm Trial (ISAT) of neurosurgical clipping versus endovascular coiling in 2143 patients with ruptured intracranial aneurysms: A randomised trial. *The Lancet*, 360(9342):1267–1274, 2002.
- [13] D. O. Wiebers, J. P. Whisnant, J. Huston, et al. Unruptured intracranial aneurysms: Natural history, clinical outcome, and risks of surgical and endovascular treatment. *The Lancet*, 362(9378):103–110, 2003.
- [14] A. Maud, K. Lakshminarayan, M. F. K. Suri, et al. Cost-effectiveness analysis of endovascular versus neurosurgical treatment for ruptured intracranial aneurysms in the United States. *Journal of Neurosurgery*, 110(5):880, 2009.
- [15] S. Chien. Mechanotransduction and endothelial cell homeostasis: The wisdom of the cell. *American Journal of Physiology - Heart and Circulatory Physiology*, 292(3):H1209–H1224, 2007.
- [16] D. L. Fry. Certain histological and chemical responses of the vascular interface to acutely induced mechanical stress in the aorta of the dog. *Circulation Research*, 24(1):93–108, 1969.
- [17] C. G. Caro, J. M. Fitz-Gerald, and R. C. Schroter. Atheroma and arterial wall shear observation, correlation and proposal of a shear dependent mass transfer mechanism for atherogenesis. *Proceedings of the Royal Society of London. Series B. Biological Sciences*, 177(1046): 109–133, 1971.
- [18] L. Boussel, V. Rayz, C. McCulloch, et al. Aneurysm growth occurs at region of low wall shear stress: Patient-specific correlation of hemodynamics and growth in a longitudinal study. *Stroke*, 39(11):2997–3002, 2008.

- [19] Z. Kulcsár, A. Ugron, M. Marosfoi, et al. Hemodynamics of cerebral aneurysm initiation: The role of wall shear stress and spatial wall shear stress gradient. *American Journal of Neuroradiology*, 32(3):587–594, 2011.
- [20] J. Frösen, A. Piippo, A. Paetau, et al. Remodeling of saccular cerebral artery aneurysm wall is associated with rupture: Histological analysis of 24 unruptured and 42 ruptured cases. *Stroke*, 35(10):2287–2293, 2004.
- [21] T. R. Forget, R. Benitez, E. Veznedaroglu, et al. A review of size and location of ruptured intracranial aneurysms. *Neurosurgery*, 49(6):1322–1325, 2001.
- [22] B. G. Thompson, R. D. Brown, S. Amin-Hanjani, et al. Guidelines for the management of patients with unruptured intracranial aneurysms: A guideline for healthcare professionals from the American Heart Association/American Stroke Association. *Stroke*, 46(8):2368–2400, 2015.
- [23] P. M. White and J. M. Wardlaw. Unruptured intracranial aneurysms. *Journal of Neuroradiology*, 30(5):336–350, 2003.
- [24] R. D. Millán, L. Dempere-Marco, J. M. Pozo, et al. Morphological characterization of intracranial aneurysms using 3-D moment invariants. *IEEE Transactions on Medical Imaging*, 26(9):1270–1282, 2007.
- [25] S. Dhar, M. Tremmel, J. Mocco, et al. Morphology parameters for intracranial aneurysm rupture risk assessment. *Neurosurgery*, 63(2):185–197, 2008.
- [26] C. Valencia, M. C. Villa-Uriol, J. M. Pozo, and A. F. Frangi. Morphological descriptors as rupture indicators in middle cerebral artery aneurysms. In *Engineering in Medicine and Biology Society (EMBC), 2010 Annual International Conference of the IEEE*, pages 6046–6049. IEEE, 2010.
- [27] J. R. Cebral, F. Mut, J. Weir, and C. Putman. Quantitative characterization of the hemodynamic environment in ruptured and unruptured brain aneurysms. *American Journal of Neuroradiology*, 32(1):145–151, 2011.

- [28] J. Xiang, S. K. Natarajan, M. Tremmel, et al. Hemodynamic-morphologic discriminants for intracranial aneurysm rupture. *Stroke*, 42(1):144–152, 2011.
- [29] L.-D. Jou, D. H. Lee, H. Morsi, and M. E. Mawad. Wall shear stress on ruptured and unruptured intracranial aneurysms at the internal carotid artery. *American Journal of Neuroradiology*, 29(9):1761–1767, 2008.
- [30] J. Xu, Y. Yu, X. Wu, et al. Morphological and hemodynamic analysis of mirror posterior communicating artery aneurysms. *PLoS ONE*, 8(1):1–7, 2013.
- [31] H. Takao, Y. Murayama, S. Otsuka, et al. Hemodynamic differences between unruptured and ruptured intracranial aneurysms during observation. *Stroke*, 43(5):1436–1439, 2012.
- [32] Y. Miura, F. Ishida, Y. Umeda, et al. Low wall shear stress is independently associated with the rupture status of middle cerebral artery aneurysms. *Stroke*, 44(2):519–521, 2013.
- [33] A. Can and R. Du. Association of hemodynamic factors with intracranial aneurysm formation and rupture: Systematic review and meta-analysis. *Neurosurgery*, 78(4):510–519, 2016.
- [34] S.-H. You, D.-S. Kong, J.-S. Kim, et al. Characteristic features of unruptured intracranial aneurysms: Predictive risk factors for aneurysm rupture. *Journal of Neurology, Neurosurgery, and Psychiatry*, 81(5):479–84, 2010.
- [35] H. Meng, V. M. Tutino, J. Xiang, and A. Siddiqui. High WSS or low WSS? Complex interactions of hemodynamics with intracranial aneurysm initiation, growth, and rupture: Toward a unifying hypothesis. *American Journal of Neuroradiology*, 35(7):1254–1262, 2014.
- [36] J. Kolega, L. Gao, M. Mandelbaum, et al. Cellular and Molecular Responses of the Basilar Terminus to Hemodynamics during Intracranial Aneurysm Initiation in a Rabbit Model. *Journal of Vascular Research*, 48(5):429–442, 2011.

- [37] J. R. Cebral, M. Vazquez, D. M. Sforza, et al. Analysis of hemodynamics and wall mechanics at sites of cerebral aneurysm rupture. *Journal of Neurointerventional Surgery*, 7(7):530–536, 2015.
- [38] S. Ø. Wille. Pulsatile pressure and flow in an arterial aneurysm simulated in a mathematical model. *Journal of Biomedical Engineering*, 3(2):153–158, 1981.
- [39] K. Perktold, T. Kenner, D. Hilbert, et al. Numerical blood flow analysis: Arterial bifurcation with a saccular aneurysm. *Basic Research in Cardiology*, 83(1):24–31, 1988.
- [40] M. Löw, K. Perktold, and R. Raunig. Hemodynamics in rigid and distensible saccular aneurysms: A numerical study of pulsatile flow characteristics. *Biorheology*, 30(3-4):287–298, 1993.
- [41] M. Shojima, M. Oshima, K. Takagi, et al. Magnitude and role of wall shear stress on cerebral aneurysm: computational fluid dynamic study of 20 middle cerebral artery aneurysms. *Stroke*, 35(11):2500–2505, 2004.
- [42] J. R. Cebral, M. A. Castro, J. E. Burgess, et al. Characterization of cerebral aneurysms for assessing risk of rupture by using patient-specific computational hemodynamics models. *American Journal of Neuroradiology*, 26(10):2550–2559, 2005.
- [43] J. J. Schneiders, H. A. Marquering, P. v. Ooij, et al. Additional value of intra-aneurysmal hemodynamics in characterizing ruptured versus unruptured intracranial aneurysms. *American Journal of Neuroradiology*, 36(10):1920–1926, 2015.
- [44] J. Xiang, J. Yu, H. Choi, et al. Rupture Resemblance Score (RRS): Toward risk stratification of unruptured intracranial aneurysms using hemodynamic-morphological discriminants. *Journal of NeuroInterventional surgery*, 7(7):490–495, 2015.
- [45] D. F. Kallmes. Point: CFD—computational fluid dynamics or confounding factor dissemination. *American Journal of Neuroradiology*, 33(3):395–6, 2012.

- [46] A. M. Robertson and P. N. Watton. Computational fluid dynamics in aneurysm research: critical reflections, future directions. *American Journal of Neuroradiology*, 33(6):992–995, 2012.
- [47] J. R. Cebral and H. Meng. Counterpoint: Realizing the clinical utility of computational fluid dynamics – Closing the gap. *American Journal of Neuroradiology*, 33(3):396–398, 2012.
- [48] H. S. Byun and K. Rhee. CFD modeling of blood flow following coil embolization of aneurysms. *Medical Engineering and Physics*, 26(9):755–761, 2004.
- [49] J. R. Cebral and R. Löhner. Efficient simulation of blood flow past complex endovascular devices using an adaptive embedding technique. *IEEE Transactions on Medical Imaging*, 24(4):468–476, 2005.
- [50] M. Haithem Babiker, L. Fernando Gonzalez, A. Felipe, et al. Quantitative effects of coil packing density on cerebral aneurysm fluid dynamics: An in vitro steady flow study. *Annals of Biomedical Engineering*, 38(7):2293–2301, 2010.
- [51] J. R. Cebral, F. Mut, M. Raschi, et al. Aneurysm rupture following treatment with flow-diverting stents: Computational hemodynamics analysis of treatment. *American Journal of Neuroradiology*, 32(1):27–33, 2011.
- [52] W. Chong, Y. Zhang, Y. Qian, et al. Computational hemodynamics analysis of intracranial aneurysms treated with flow diverters: Correlation with clinical outcomes. *American Journal of Neuroradiology*, 35(1):136–142, 2014.
- [53] M. Kim, D. B. Taulbee, M. Tremmel, and H. Meng. Comparison of two stents in modifying cerebral aneurysm hemodynamics. *Annals of Biomedical Engineering*, 36(5):726–741, 2008.
- [54] D. Ma, G. F. Dargush, S. K. Natarajan, et al. Computer modeling of deployment and mechanical expansion of neurovascular flow diverter in patient-specific intracranial aneurysms. *Journal of Biomechanics*, 45(13):2256–2263, 2012.

- [55] A. G. Radaelli, L. Augsburger, J. R. Cebal, et al. Reproducibility of haemodynamical simulations in a subject-specific stented aneurysm model - A report on the Virtual Intracranial Stenting Challenge 2007. *Journal of Biomechanics*, 41(10):2069–2081, 2008.
- [56] S. Appanaboyina, F. Mut, R. Löhner, et al. Computational fluid dynamics of stented intracranial aneurysms using adaptive embedded unstructured grids. *International Journal for Numerical Methods in Fluids*, 57(5):475–493, 2008.
- [57] J. Krejza, M. Arkuszewski, S. E. Kasner, et al. Carotid artery diameter in men and women and the relation to body and neck size. *Stroke*, 37(4):1103–1105, 2006.
- [58] B. C. Flores, W. W. Scott, C. S. Eddleman, et al. The A1-A2 diameter ratio may influence formation and rupture potential of anterior communicating artery aneurysms. *Neurosurgery*, 73(5):845–853, 2013.
- [59] J. Lang. *Skull base and related structures: Atlas of clinical anatomy*. Schattauer Verlag, 2001.
- [60] P. B. Bijari, L. Antiga, B. A. Wasserman, and D. A. Steinman. Scan-rescan reproducibility of carotid bifurcation geometry from routine contrast-enhanced MR angiography. *Journal of Magnetic Resonance Imaging*, 33(2):482–489, 2011.
- [61] J. Poethke, L. Goubergrits, U. Kertzscher, et al. Impact of imaging modality for analysis of a cerebral aneurysm: Comparison between CT, MRI and 3DRA. In J. Vander Sloten, P. Verdonck, M. Nyssen, and J. Haueisen, editors, *4th European Conference of the International Federation for Medical and Biological Engineering: ECIFMBE 2008 23–27 November 2008 Antwerp, Belgium*, pages 1889–1893. Springer Berlin Heidelberg, 2009.
- [62] A. J. Geers, I. Larrabide, a. G. Radaelli, et al. Patient-specific computational hemodynamics of intracranial aneurysms from 3D rotational angiography and CT angiography: An in vivo reproducibility study. *American Journal of Neuroradiology*, 32(3):581–586, 2011.

- [63] M. Piccinelli, D. a. Steinman, Y. Hoi, et al. Automatic neck plane detection and 3D geometric characterization of aneurysmal sacs. *Annals of Biomedical Engineering*, 40(10):2188–2211, 2012.
- [64] J. Cezbral and M. Castro. Flow–area relationship in internal carotid and vertebral arteries. *Physiological Measurement*, 29(5):585–594, 2008.
- [65] K. Valen-Sendstad, M. Piccinelli, R. KrishnankuttyRema, and D. A. Steinman. Estimation of inlet flow rates for image-based aneurysm CFD models: Where and how to begin? *Annals of Biomedical Engineering*, 43(6):1422–1431, 2015.
- [66] A. Marzo, P. Singh, P. Reymond, et al. Influence of inlet boundary conditions on the local haemodynamics of intracranial aneurysms. *Computer Methods in Biomechanics and Biomedical Engineering*, 12(4):431–444, 2009.
- [67] A. Marzo, P. Singh, I. Larrabide, et al. Computational hemodynamics in cerebral aneurysms: The effects of modeled versus measured boundary conditions. *Annals of Biomedical Engineering*, 39(2):884–896, 2011.
- [68] D. A. Steinman. Assumptions in modelling of large artery hemodynamics. In *Modeling of Physiological Flows*, pages 1–18. Springer, 2012.
- [69] Ø. Evju, K. Valen-Sendstad, and K.-A. Mardal. A study of wall shear stress in 12 aneurysms with respect to different viscosity models and flow conditions. *Journal of Biomechanics*, 46(16):2802–2808, 2013.
- [70] J. Xiang, M. Tremmel, J. Kolega, et al. Newtonian viscosity model could overestimate wall shear stress in intracranial aneurysm domes and underestimate rupture risk. *Journal of Neurointerventional Surgery*, 4(4):351–357, 2012.
- [71] M. A. Castro, M. C. A. Olivares, C. M. Putman, and J. R. Cezbral. Unsteady wall shear stress analysis from image-based computational fluid dynamic aneurysm models under Newtonian and Casson rheological models. *Medical and Biological Engineering and Computing*, 52(10):827–839, 2014.
- [72] Y. Bazilevs, M. C. Hsu, Y. Zhang, et al. Computational vascular fluid-structure interaction: Methodology and application to cerebral

- aneurysms. *Biomechanics and Modeling in Mechanobiology*, 9(4):481–498, 2010.
- [73] J. G. Isaksen, Y. Bazilevs, T. Kvamsdal, et al. Determination of Wall Tension in Cerebral Artery Aneurysms by Numerical Simulation. *Stroke*, 39(12):3172–3179, 2008.
- [74] R. Torii, M. Oshima, T. Kobayashi, et al. Influence of wall elasticity in patient-specific hemodynamic simulations. *Computers & Fluids*, 36(1):160–168, 2007.
- [75] A. Valencia, F. Muñoz, S. Araya, et al. Comparison between computational fluid dynamics, fluid–structure interaction and computational structural dynamics predictions of flow-induced wall mechanics in an anatomically realistic cerebral aneurysm model. *International Journal of Computational Fluid Dynamics*, 23(9):649–666, 2009.
- [76] A. M. Robertson, X. Duan, K. M. Aziz, et al. Diversity in the strength and structure of unruptured cerebral aneurysms. *Annals of Biomedical Engineering*, 43(7):1502–1515, 2015.
- [77] R. Torii, M. Oshima, T. Kobayashi, et al. Influence of wall thickness on fluid–structure interaction computations of cerebral aneurysms. *International Journal for Numerical Methods in Biomedical Engineering*, 26(3-4):336–347, 2010.
- [78] C. Murray. The physiological principle of minimum work : I. The vascular system and the cost of blood volume. *Proceedings of the National Academy of Sciences*, 12(3):207–214, 1926.
- [79] M. Zamir. The role of shear forces in arterial branching. *The Journal of General Physiology*, 67(2):213–222, 1976.
- [80] A. M. Malek, S. L. Alper, and S. Izumo. Hemodynamic shear stress and its role in atherosclerosis. *JAMA: the journal of the American Medical Association*, 282(21):2035–2042, 1999.
- [81] D. M. Sforza, K. Kono, S. Tateshima, et al. Hemodynamics in growing and stable cerebral aneurysms. *Journal of NeuroInterventional Surgery*, pages 1–6, 2015.

- [82] L. Goubergrits, J. Schaller, U. Kertzscher, et al. Statistical wall shear stress maps of ruptured and unruptured middle cerebral artery aneurysms. *Journal of The Royal Society Interface*, 9(69):677–688, 2012.
- [83] S. Rossitti and J. Löfgren. Vascular dimensions of the cerebral arteries follow the principle of minimum work. *Stroke*, 24(3):371–377, 1993.
- [84] C. Cheng, F. Helderman, D. Tempel, et al. Large variations in absolute wall shear stress levels within one species and between species. *Atherosclerosis*, 195(2):225–235, 2007.
- [85] I. G. H. Jansen, J. J. Schneiders, W. V. Potters, et al. Generalized versus patient-specific inflow boundary conditions in computational fluid dynamics simulations of cerebral aneurysmal hemodynamics. *American Journal of Neuroradiology*, 35(8):1543–1548, 2014.
- [86] G. G. Ferguson. Physical factors in the initiation, growth, and rupture of human intracranial saccular aneurysms. *Journal of Neurosurgery*, 37(6):666–677, 1972.
- [87] W. Stehbens. Flow in glass models of arterial bifurcations and berry aneurysms at low Reynolds numbers. *Quarterly Journal of Experimental Physiology and Cognate Medical Sciences*, 60(3):181–192, 1975.
- [88] K. Valen-Sendstad, K.-A. Mardal, and D. A. Steinman. High-resolution CFD detects high-frequency velocity fluctuations in bifurcation, but not sidewall, aneurysms. *Journal of Biomechanics*, 46(2):402–407, 2013.
- [89] Ø. Evju and K.-A. Mardal. On the assumption of laminar flow in physiological flows: Cerebral aneurysms as an illustrative example. In *Modeling the Heart and the Circulatory System*, volume 14, pages 177–195. 2015.
- [90] M. O. Khan, K. Valen-Sendstad, and D. A. Steinman. Narrowing the expertise gap for predicting intracranial aneurysm hemodynamics: Impact of solver numerics versus mesh and time-step resolution. *American Journal of Neuroradiology*, 36(7):1310–1316, 2015.

- [91] N. Varble, J. Xiang, N. Lin, and H. Meng. Flow instability detected by high-resolution CFD in fifty-six middle cerebral artery aneurysms. *Journal of Biomechanical Engineering*, 138(6), 2016.
- [92] D. A. Fedosov, B. Caswell, and G. E. Karniadakis. A multiscale red blood cell model with accurate mechanics, rheology, and dynamics. *Biophysical Journal*, 98(10):2215–2225, 2010.
- [93] D. A. Fedosov, H. Noguchi, and G. Gompper. Multiscale modeling of blood flow: From single cells to blood rheology. *Biomechanics and Modeling in Mechanobiology*, 13(2):239–258, 2014.
- [94] A. Bedekar, K. Pant, Y. Ventikos, and S. Sundaram. A computational model combining vascular biology and haemodynamics for thrombosis prediction in anatomically accurate cerebral aneurysms. *Food and Bioproducts Processing*, 83(2):118–126, 2005.
- [95] L. Grinberg, J. A. Insley, V. Morozov, et al. A new computational paradigm in multiscale simulations: Application to brain blood flow. In *Proceedings of the 2011 ACM/IEEE International Conference for High Performance Computing, Networking, Storage and Analysis, Seattle, WA*, pages 1–12, 2011.
- [96] I. Chatziprodromou, A. Tricoli, D. Poulikakos, and Y. Ventikos. Haemodynamics and wall remodelling of a growing cerebral aneurysm: A computational model. *Journal of Biomechanics*, 40(2):412–26, 2007.
- [97] C. A. Figueroa, S. Baek, C. A. Taylor, and J. D. Humphrey. A computational framework for fluid-solid-growth modeling in cardiovascular simulations. *Computer Methods in Applied Mechanics and Engineering*, 198(45-46):3583–3602, 2010.
- [98] D. A. Steinman, Y. Hoi, P. Fahy, et al. Variability of computational fluid dynamics solutions for pressure and flow in a giant aneurysm: The ASME 2012 Summer Bioengineering Conference CFD Challenge. *Journal of Biomechanical Engineering*, 135(2):021016–021016–13, 2013.
- [99] D. Fiorella, C. Sadasivan, H. H. Woo, and B. Lieber. Regarding “Aneurysm rupture following treatment with flow-diverting stents: Computational hemodynamics analysis of treatment”. *American Journal of Neuroradiology*, 32(5):E95–E97, 2011.

- [100] K. Valen-Sendstad and D. A. Steinman. Mind the gap: Impact of computational fluid dynamics solution strategy on prediction of intracranial aneurysm hemodynamics and rupture status indicators. *American Journal of Neuroradiology*, 35(3):536–543, 2013.
- [101] Y. Bazilevs, M. C. Hsu, Y. Zhang, et al. A fully-coupled fluid-structure interaction simulation of cerebral aneurysms. *Computational Mechanics*, 46(1):3–16, 2010.
- [102] T. E. Tezduyar, K. Takizawa, C. Moorman, et al. Multiscale sequentially-coupled arterial FSI technique. *Computational Mechanics*, 46(1):17–29, 2010.
- [103] F. Nobile and C. Vergara. An effective fluid-structure interaction formulation for vascular dynamics by generalized Robin conditions. *SIAM Journal on Scientific Computing*, 30(2):731–763, 2008.
- [104] M. A. Fernandez, M. Landajuela, and M. Vidrascu. Fully decoupled time-marching schemes for incompressible fluid/thin-walled structure interaction. *Journal of Computational Physics*, 297:156–181, 2015.
- [105] R. Retarekar. *Hemodynamics and natural history outcome in unruptured intracranial aneurysms*. Phd dissertation, University of Iowa, 2012.
- [106] J. Liu, J. Fan, J. Xiang, et al. Hemodynamic characteristics of large unruptured internal carotid artery aneurysms prior to rupture: A case control study. *Journal of Neurointerventional Surgery*, 8:367–372, 2016.
- [107] V. M. Pereira, O. Brina, P. Bijlenga, et al. Wall shear stress distribution of small aneurysms prone to rupture a case-control study. *Stroke*, 45(1):261–264, 2014.
- [108] G. Duan, N. Lv, J. Yin, et al. Morphological and hemodynamic analysis of posterior communicating artery aneurysms prone to rupture: A matched case-control study. *Journal of Neurointerventional Surgery*, 8(1):47–51, 2014.
- [109] J. J. Schneiders, H. a. Marquering, R. Van Den Berg, et al. Rupture-associated changes of cerebral aneurysm geometry: High-resolution 3D

- imaging before and after rupture. *American Journal of Neuroradiology*, 35(7):1358–1362, 2014.
- [110] W. Brinjikji, B. J. Chung, C. Jimenez, et al. Hemodynamic differences between unstable and stable unruptured aneurysms independent of size and location: a pilot study. *Journal of Neurointerventional Surgery*, (0):1–6, 2016.
- [111] G. Pizzichelli, B. Kehlet, Ø. Evju, et al. Numerical study of intrathecal drug delivery to a permeable spinal cord: Effect of catheter position and angle. *Submitted to Computer Methods in Biomechanics and Biomedical Engineering*, 2016.
- [112] S. W. Funke, M. Nordaas, Ø. Evju, et al. Variational data assimilation for transient blood flow simulations. *Submitted to SIAM Journal on Scientific Computing*. <http://arxiv.org/abs/1607.03013>, 2016.
- [113] P. Farrell, D. Ham, S. Funke, and M. Rognes. Automated derivation of the adjoint of high-level transient finite element programs. *SIAM Journal on Scientific Computing*, 35(4):369–393, 2013.
- [114] A. Logg, K.-A. Mardal, and G. Wells. *Automated solution of differential equations by the finite element method: The FEniCS book*, volume 84. Springer Science & Business Media, 2012.
- [115] M. Mortensen and K. Valen-Sendstad. Oasis: A high-level/high-performance open source Navier-Stokes solver. *Computer Physics Communications*, 188:177–188, 2015.

Paper I

A study of wall shear stress in 12 aneurysms with respect to different viscosity models and flow conditions

*Øyvind Evju, Kristian Valen-Sendstad and
Kent-Andre Mardal.*

Journal of Biomechanics 46 (16), 2802-2808



A study of wall shear stress in 12 aneurysms with respect to different viscosity models and flow conditions



Øyvind Evju^a, Kristian Valen-Sendstad^{a,b}, Kent-André Mardal^{a,*}

^a Center for Biomedical Computing, Simula Research Laboratory, Martin Linges vei 17, Fornebu, Norway

^b Biomedical Simulation Laboratory, Department of Mechanical & Industrial Engineering, University of Toronto, 5 Kings College Road, Toronto, ON, Canada

ARTICLE INFO

Article history:

Accepted 1 September 2013

Keywords:

Cerebral aneurysms
Computational fluid dynamics
Wall shear stress
Non-Newtonian fluid
Boundary conditions

ABSTRACT

Recent computational fluid dynamics (CFD) studies relate abnormal blood flow to rupture of cerebral aneurysms. However, it is still debated how to model blood flow with sufficient accuracy. Common assumptions made include Newtonian behaviour of blood, traction free outlet boundary conditions and inlet boundary conditions based on available literature. These assumptions are often required since the available patient specific data is usually restricted to the geometry of the aneurysm and the surrounding vasculature. However, the consequences of these assumptions have so far been inadequately addressed.

This study investigates the effects of 4 different viscosity models, 2 different inflow conditions and 2 different outflow conditions in 12 middle cerebral artery aneurysms. The differences are quantified in terms of 3 different wall shear stress (WSS) metrics, involving maximal WSS, average WSS, and proportion of aneurysm sac area with low WSS. The results were compared with common geometrical metrics such as volume, aspect ratio, size ratio and parent vessel diameter and classifications in terms of sex and aneurysm type.

The results demonstrate strong correlations between the different viscosity models and boundary conditions. The correlation between the different WSS metrics range from weak to medium. No strong correlations were found between the different WSS metrics and the geometrical metrics or classifications.

© 2013 Elsevier Ltd. All rights reserved.

1. Introduction

Cerebral aneurysms are relatively common. Around 1–6% of the population develop aneurysms during a life-time (Schievink, 1997) and often at a quite early age (50–60 years). The rupture of a cerebral aneurysm causes subarachnoid hemorrhage (SAH), a stroke associated with high risk of morbidity, and a mortality rate as high as 60% within 30 days (Le Roux and Wallace, 2010). The rupture risk is however quite low, usually estimated to less than 1% per year (Rinkel et al., 1998). Risk of rupture has been related to the size and morphology of aneurysms and their surrounding vasculature, but individual risk assessment is still not feasible. CFD could potentially aid clinicians in individualized assessment and treatment planning, and is therefore under active research.

Recently, three large retrospective computational studies have demonstrated that fluid dynamics simulations can be used to discriminate ruptured from non-ruptured aneurysms (Cebal et al., 2011a, 2011b; Xiang et al., 2011). However, what constitutes an appropriate computational model is an open question. Fluid–

structure interaction (e.g. Bazilevs et al., 2010; Isaksen et al., 2008) and non-linear viscosity models (e.g. Gambaruto et al., 2011; Xiang et al., 2012) have received some attention as extensions of the more commonly used Newtonian flow simulations within rigid vessels. Still, while these studies argue for adding complexity to the model, they typically employ relatively simple boundary conditions obtained from the literature and only consider a few aneurysms.

Vascular remodelling due to flow conditions was observed already 150 years ago by Virchow. As demonstrated more recently by e.g. Chien (2007) and Hoi et al. (2008), among others, the wall shear stress (WSS) acting on the endothelial cells surfacing the arterial wall plays a central role in this remodelling. It has been shown that aneurysms grow in the direction of low WSS (Boussel et al., 2008), but there is no conclusion whether low or high WSS correlates with rupture status. That is, certain studies have found high WSS to be correlated with rupture status (Jou et al., 2008; Cebal et al., 2011b), which contrasts the correlation of low WSS reported by others (Xiang et al., 2011; Miura et al., 2013).

Recently, clinical researchers have expressed scepticism towards CFD analysis because of the overwhelming and confounding number of models and flow metrics, c.f. the editorial in AJNR (Kallmes, 2012). It is therefore timely to compare different models and metrics in an effort to reduce this number. In this study we simulate flow in 12

* Correspondence to: Center for Biomedical Computing, Simula Research Laboratory, P.O. Box 134, N-1325 Lysaker, Norway. Tel.: +47 93610854.
E-mail address: kent-and@simula.no (K.-A. Mardal).

different middle cerebral artery (MCA) aneurysms, 4 different viscosity models, 2 different inflow boundary conditions and 2 different outflow boundary conditions. We included natural sex and age variations in the hematocrit levels of the viscosity models. WSS is quantified in terms of three different metrics: maximal WSS, average WSS, and proportion of aneurysm sac area with low WSS with respect to the different viscosity models and boundary conditions. We also compare with common geometry metrics such as aneurysm volume, aspect ratio, and parent vessel diameter and classifications in terms of sex and aneurysm type.

2. Methods

Computed tomography angiography (CTA) volume images were obtained from a 16 multi-detector row spiral scanner (Somatom Sensation 16; Siemens, Erlangen, Germany) taken from 12 MCA aneurysms treated at the Department of Neurosurgery, University Hospital of North Norway between 2006 and 2008. The register was approved by the local ethics committee and data inspectorate.

The Vascular Modelling Toolkit (VMTK) was used to segment the CTA images and create CFD meshes. The aneurysm models have been meshed with 800,000–1,200,000 tetrahedral cells containing three boundary layers. The isolation of the aneurysm sac was done using the same approach as Ford et al. (2009). We used a previously developed and validated Navier–Stokes solver (Valen-Sendstad et al., 2012a) implemented in FEniCS (Logg et al., 2011), with minor extensions to stabilize the flow for larger time steps. Specifically, we implemented an incremental pressure correction scheme (Goda, 1979) with semi-implicit handling of the nonlinear convection term, implicit Euler time-stepping and used first order linear continuous elements for both the velocity and pressure. This scheme was found favorable when compared to the schemes in Valen-Sendstad et al. (2012a) in terms of the accuracy and efficiency. A thorough comparison and verification of this scheme can be found in Evju (2011), which shows that the scheme is second order accurate in space and first order in time.

Mesh convergence for the involving meshes has been verified in a previous study (Valen-Sendstad, 2011, paper IV), where the maximal pointwise kinetic energy and total kinetic energy varied with less than 2% between the two finest meshes for all cases, and the maximal pointwise vorticity and integrated vorticity varied with less than 5% between the same meshes. A time step of 1.25 ms was used, which gave 800 time steps per second. The simulations were run for four cycles to eliminate cyclic variations, and the solution was saved at every fifth time step of the fourth cycle.

For all the 12 aneurysm geometries (see Fig. 1), we employed and compared four different viscosity models, two different inlet boundary conditions and two different outlet boundary conditions, for a total of 72 simulations. The different viscosity models are summarized in Table 1. A Newtonian viscosity model with a value of 0.00345 Pa s was used as reference. The Casson model incorporates hematocrit and asymptotic viscosity. Hematocrit level varies according to age and sex and we have chosen hematocrit levels 38% (C38) and 40% (C40) corresponding to women before and after menopause (Jacobsen et al., 2012). The shear-rate dependence of all viscosity models is as visualized in Fig. 2. The marked area in this figure demonstrates the asymptotic behaviour of the different viscosity models, ranging from shear rates typical for healthy MCAs. The Newtonian reference model has the same viscosity as the asymptotic value of the modified Cross model, making this model relevant for isolating the shear thinning effects. Both the Casson models have lower asymptotic values, and the difference between them reflects the change in hematocrit.

The inlet velocity is set to be a linear interpolation of a parabolic profile radially in space. The spatial peak velocity is determined by using a pulsatile waveform, depicted in Fig. 3. This waveform is taken from the MCA segment of a female patient undergoing cerebrovascular treatment. For our reference calculations, the spatial peak velocity has been scaled to a timed average of 0.75 m/s, which has been found to be an average flow velocity in female MCAs (Krejza et al., 2005). As a comparison to this, we have also employed a set of simulations using a reduced inflow velocity of 25% to 0.56 m/s, roughly corresponding to the average velocity in the MCA of people aged > 60. For all simulations we used a heart rate of 75 beats per minute, and a density of 1056 kg/m³.

To represent the peripheral resistance, a resistance condition is applied at the outlets in the reference simulations:

$$p = CQ_o,$$

where Q_o is the flow rate through the outlet. The value of the coefficient is set to $C = 5.97 \times 10^9$ Pa s/m³ for the MCA (Alastruey et al., 2007). The traction free outflow conditions corresponds to $C=0$. The parameters used for each set of simulations have been summarized in Table 2.

For the reference case, we computed some key flow properties, shown in Table 3. The Reynolds number (Re) is computed as $QD/(\nu A)$, where Q , D , ν , and A are the inlet flow rate, parent vessel diameter, kinematic viscosity, and parent vessel cross sectional area, respectively. The Womersley number (Wo) is computed as

$R(\omega/\nu)^{1/2}$, where R is the radius and ω is the angular frequency. The inlet WSS (IWSS) is calculated from the Poiseuille formula, $\tau = 8\mu Q/(DA)$, where μ corresponds to the Newtonian viscosity value. The inlet diameter varies from 1.5 mm to 3.5 mm, roughly a factor 2.3, which is also reflected in the Reynolds and Womersley numbers. Correspondingly, the flow rate varies by a factor of 5.2, or 2.3^2 , from 0.633 mL/s to 3.600 mL/s. The IWSS is inversely related to the diameter.

The WSS magnitude has been time-averaged over the full cardiac cycle, and normalized with the IWSS. Based on results of previous studies on the relationship between WSS and aneurysm growth and rupture (see for example Cebal et al., 2011b; Xiang et al., 2011; Jou et al., 2008), we have chosen and calculated three WSS metrics. These are the maximum WSS of the aneurysm sac (MWSS), the average WSS over the aneurysm sac (AWSS) and the area of low shear (LSA) which have been defined as the area where the normalized WSS is less than 0.1, divided by the total sac area.

The correlation was calculated using Pearson's correlation coefficient. With two sets of measurements $X = \{x_1, x_2, \dots, x_n\}$ and $Y = \{y_1, y_2, \dots, y_n\}$, the coefficient is calculated as

$$r_{X,Y} = \frac{\sum_{i=1}^n (x_i - \bar{x})(y_i - \bar{y})}{\sqrt{\sum_{i=1}^n (x_i - \bar{x})^2 \sum_{i=1}^n (y_i - \bar{y})^2}}$$

where \bar{x} and \bar{y} is the sample mean of X and Y , respectively. Strong, medium, and weak correlation are defined by absolute values of $r_{X,Y}$ greater than 0.8, greater than 0.4, and less than 0.4, respectively. For the data with binary outcome, sex and aneurysm type, we let men and bifurcation take the value 1, while women and sidewall are 0.

3. Results

Average WSS: There are large differences in AWSS between the aneurysms in the reference case, ranging from a minimum value of 0.24 (A12) to a maximum of 1.8 (A6) (ratio 7.7), with an average value of 0.94, as shown in Fig. 4a. The effects of the different viscosity models differ from the reference in the range –9.4% to 5.3%. The variations are largest for the C38 case, with an average decrease of 3.1% and a standard deviation of 3.8%. The modified Cross model, which is the only model that isolates the shear thinning, predicts the smallest deviations on an average (0.5%) and has the lowest standard deviation (2.4%).

For the cases with modified boundary conditions, we see that the differences from the reference are far larger than in the non-Newtonian cases. For the reduced inflow case, the AWSS was significantly reduced on an average (–22.4%). This suggests that the WSS in the aneurysm is more sensitive to flow changes than what a linear relationship would predict.

For the traction free case, the results vary greatly, from –6.8% to 36.1%. It is worth noting that the three traction free simulations causing the largest differences from the reference simulations are A1, A4 and A5, where the aneurysms all occur downstream from a modelled bifurcation, see also Fig. 1. The different outflow conditions do in these cases cause a significantly different flow diversion between the different outlets (A1: 36.1%, A4: –6.8%, and A5: 12.4%) and correspondingly different flow and WSS within the aneurysms. For the other aneurysms, the changes are of the same order as for the non-Newtonian cases.

Maximum WSS: As shown in Fig. 4b, the MWSS reference values vary from 2.3 (A11) to 11 (A9) (ratio 4.6), with an average value of 6.0. The changes caused by the viscosity models range from –7.7% to 3.9%. Again, the C38 model yields the greatest variations, with a standard deviation of 3.5%. Similar results are obtained for the C40 case. The modified Cross model is again the most coherent with the reference values, although a clear indication is shown for a slightly lower MWSS, with an average decrease of 2.8% and standard deviation of 2.0%.

We also note that the viscosity seems to be of greater significance in some aneurysms than others. In aneurysm A4 for example, the C38 model predicts an increase as high of 3.9%, the C40 model predicts an increase of 2.2% and the MC model predicts a –7.2% change. In other aneurysms, such as A2 and A3, the MWSS seems to be much less dependent on viscosity.

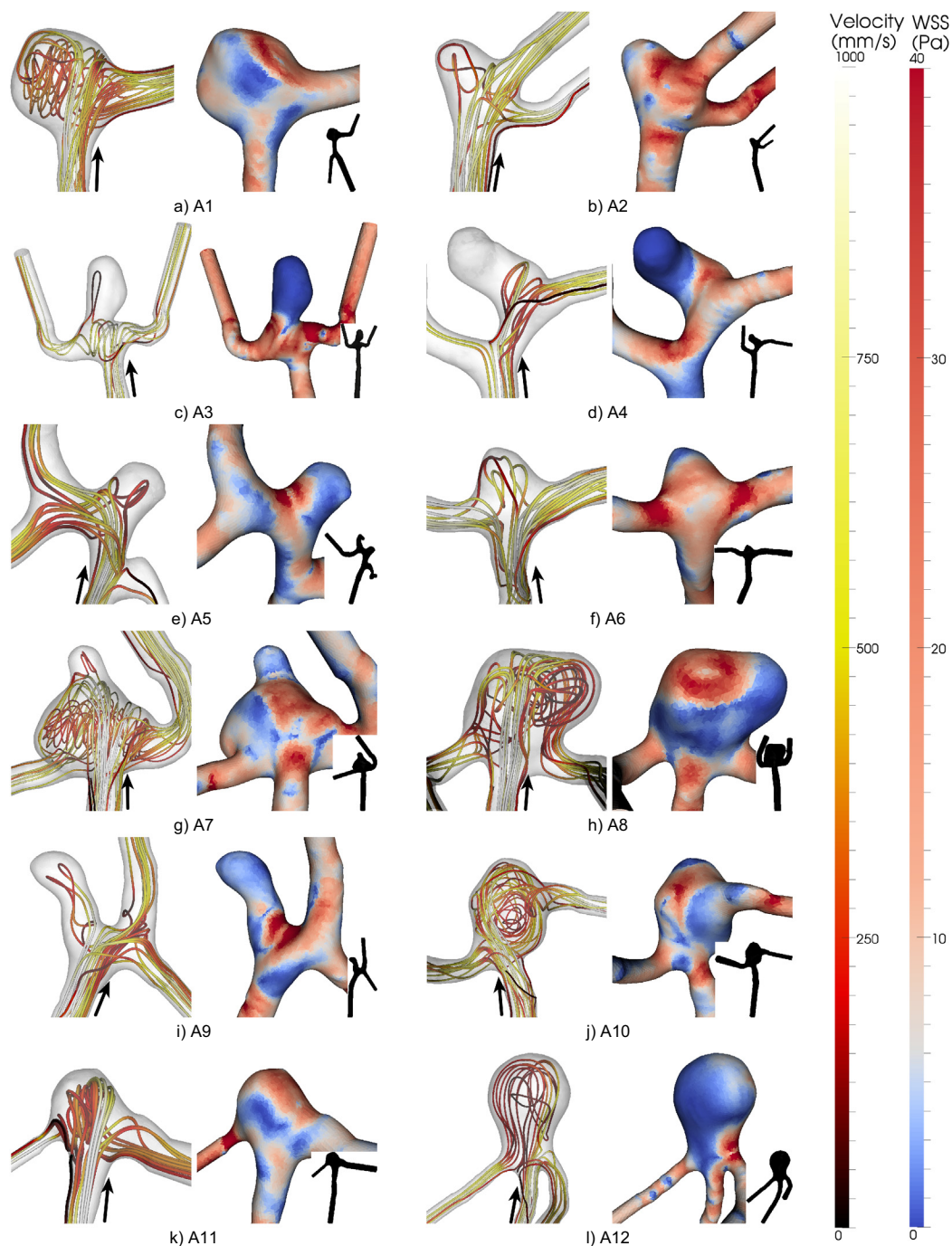


Fig. 1. The 12 different aneurysms used in simulations. Streamlines of the velocity at systole on the left, and the corresponding WSS magnitude on the right. The inflow is from below. Images are created from the reference simulations.

For the reduced inflow case, we see very similar variations as found for AWSS. Again, the average decrease in MWSS is more sensitive than the 25% reduction predicted by linear relationship, with an average additional decrease of 22.9%. The variations for the traction free case are large, ranging from -4.0% to 37.4% . The results are not coherent with those for the AWSS. In aneurysm A6 for example, we see an increase in max WSS of 16.9%. This is in contrast to the results for AWSS, which showed an increase of only 1.5%. In this particular case, the MWSS occurs close to the edge of the isolated aneurysm sac causing this peak WSS to fall outside the sac in the case in the reference simulation.

Area of low WSS: For the LSA metric, the reference values vary greatly, from 0.002 (A1) to 0.59 (A4) (ratio 293), and the

average is 0.17, as seen in Fig. 4c. There are mainly three aneurysms (A3, A4 and A12) that contribute to the relatively high average area.

The shear thinning effects, isolated in the modified Cross model, tend towards a reduced LSA. The two Casson models predict similar changes. Overall, there are only small variations caused by the viscosity models, with differences in the range -0.037 to 0.022 .

The reduced inflow case shows the largest changes by far, with an average increase of 0.046. In all aneurysms, this case predicted an increased area, however, the variations between the aneurysms are large. Case A5 is particularly interesting, as this increases to 0.233, almost three times the reference value.

Table 1

The viscosity models used in the simulations. The modified Cross and Casson model parameters are taken from Robertson et al. (2009) and Yeow et al. (2002), Dintenfass (1985), respectively.

Name	Model	Parameters
Newtonian	$\mu = 0.00345 \text{ Pa s}$	
Modified Cross	$\hat{\mu} = (1 + (\lambda\dot{\gamma})^m)^{-a}$	$\hat{\mu} = (\mu - \mu_\infty) / (\mu_0 - \mu_\infty)$, $\lambda = 3.736 \text{ s}; m = 2.406$, $a = 0.254, \mu_0 = 0.056 \text{ Pa s}$, $\mu_\infty = 0.00345 \text{ Pa s}$
Casson	$\mu = \frac{\tau_y}{\dot{\gamma}} + \frac{2\sqrt{\mu_\infty\sqrt{\tau_y}}}{\sqrt{\dot{\gamma}}} + \mu_\infty$	$\tau_y = 0.02687 \text{ H}^3 \text{ Pa s}$, $\mu_\infty = \eta_0(1 - TkH)^{-2.5}$, $\eta_0 = 0.00145 \text{ Pa s}$, $Tk = 0.62, (H = \text{Hematocrit})$.

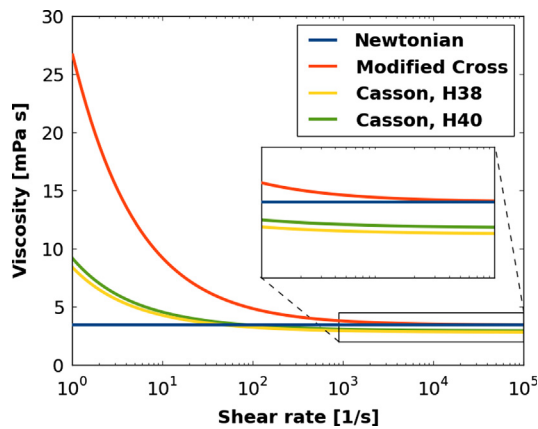


Fig. 2. The viscosity as a function of the shear rate for the different viscosity models.

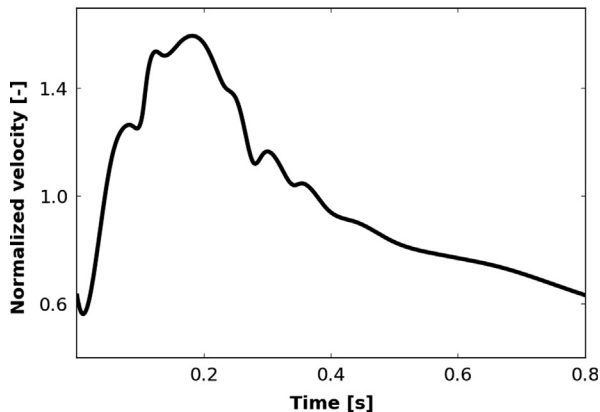


Fig. 3. Normalized waveform.

Table 2

A summary of the parameters used in the different simulations. The simulations described by the first row is used as a reference for the comparisons with the other simulations.

Simulation	Key	Viscosity	Inflow condition	Outflow condition
Reference	Ref.	Newtonian	0.75 m/s	Resistance
Modified Cross	MC	Modified Cross	Ref.	Ref.
Casson, H40	C40	Casson, hct 40%	Ref.	Ref.
Casson, H38	C38	Casson, hct 38%	Ref.	Ref.
Traction free	TF	Ref.	Ref.	Traction free
Reduced inflow	RI	Ref.	0.56 m/s	Ref.

Table 3

A summary of the reference simulations, with inlet diameter, Reynolds and Womersley numbers, flow rate, calculated average WSS at the inlet, rupture status (ruptured/unruptured), type (sidewall/bifurcation), sex, aneurysm volume, aspect ratio and size ratio.

Aneurysm	D (mm)	Re (-)	Wo (-)	Q (mL/s)	IWSS (Pa)	Status	Type	Sex	V (mm ³)	AR (-)	SR (-)
A1	3.43	386	2.66	3.40	2.96	U	S	M	212	1.15	3.04
A2	2.51	248	1.95	1.59	3.54	U	B	F	33	0.90	1.59
A3	2.49	241	1.93	1.54	3.49	R	B	F	54	1.80	3.61
A4	2.12	222	1.64	1.21	4.45	U	S	F	43	1.42	3.08
A5	1.96	209	1.52	1.05	4.92	U	S	F	13	1.08	1.54
A6	2.55	282	1.98	1.85	3.91	R	B	M	18	0.79	1.58
A7	3.53	398	2.74	3.60	2.88	R	B	M	509	1.00	3.95
A8	2.40	264	1.86	1.62	4.14	R	B	F	278	0.94	3.86
A9	2.24	246	1.74	1.42	4.41	R	S	F	33	2.10	3.74
A10	2.68	298	2.08	2.05	3.74	R	B	F	265	0.80	3.32
A11	1.55	159	1.20	0.63	6.00	R	B	F	24	0.59	1.65
A12	1.74	184	1.35	0.82	5.46	U	B	M	251	2.25	5.85

The traction free case displays only minor changes, comparable to the changes caused by different viscosity models. The differences range from -0.012 to 0.028 .

Correlation: Shown in Fig. 5 are scatterplots of each metric, comparing the values from the reference case with those obtained by the other cases. The linear correlation is very strong for all cases, with r -values of 0.95 or higher. The differences in viscosity models give correlation values of 0.995 or higher.

Table 4 shows the correlation matrix between aneurysm type, sex, parent vessel diameter (D), aneurysm volume (V), aspect ratio (AR), size ratio (SR), MWSS, AWSS, and LSA. There are no strong correlations, but there are medium correlations between LSA and AR (0.72), SR and AR (0.71), AWSS and LSA (-0.63), SR and V (0.60), D and V (0.59), AWSS and AE (0.52), LSA and SE (0.50), D and Sex (0.47), Sex and V (0.48), and Sex and AWSS (0.44). The rest of the correlations are low. Fig. 6 shows the relationship between the different WSS metrics.

4. Discussion

This study investigates 3 different WSS metrics in 12 cerebral aneurysms with respect to 2 different inflow conditions, 2 different outflow conditions, and 4 different viscosity models. The different WSS metrics showed only weak or medium correlation (-0.06 , 0.40 and -0.63) between each other and the other geometrical metrics. The different viscosity models gave less than 4% change on an average for the different WSS metrics. Furthermore, the different viscosity models and boundary conditions all showed strong correlation (> 0.95).

The low sensitivity of average WSS with respect to the viscosity model is consistent with other studies (Gambaruto et al., 2011; Jiang et al., 2011; Lee and Steinman, 2007), which concern one single cerebral aneurysm, a canine model aneurysm, and carotid arteries. Furthermore, neglecting the non-Newtonian effects of blood may underestimate the average WSS, as well as overestimate the maximum WSS, which is coherent with the recent study (Chen and Lu, 2006).

We have investigated 4 different viscosity models, but many other nonlinear viscosity models have been proposed or considered (see for example Gambaruto et al., 2011; Chen and Lu, 2006). However, during this study, we considered seven different viscosity models initially, and similar results were obtained with all models (Evju, 2011).

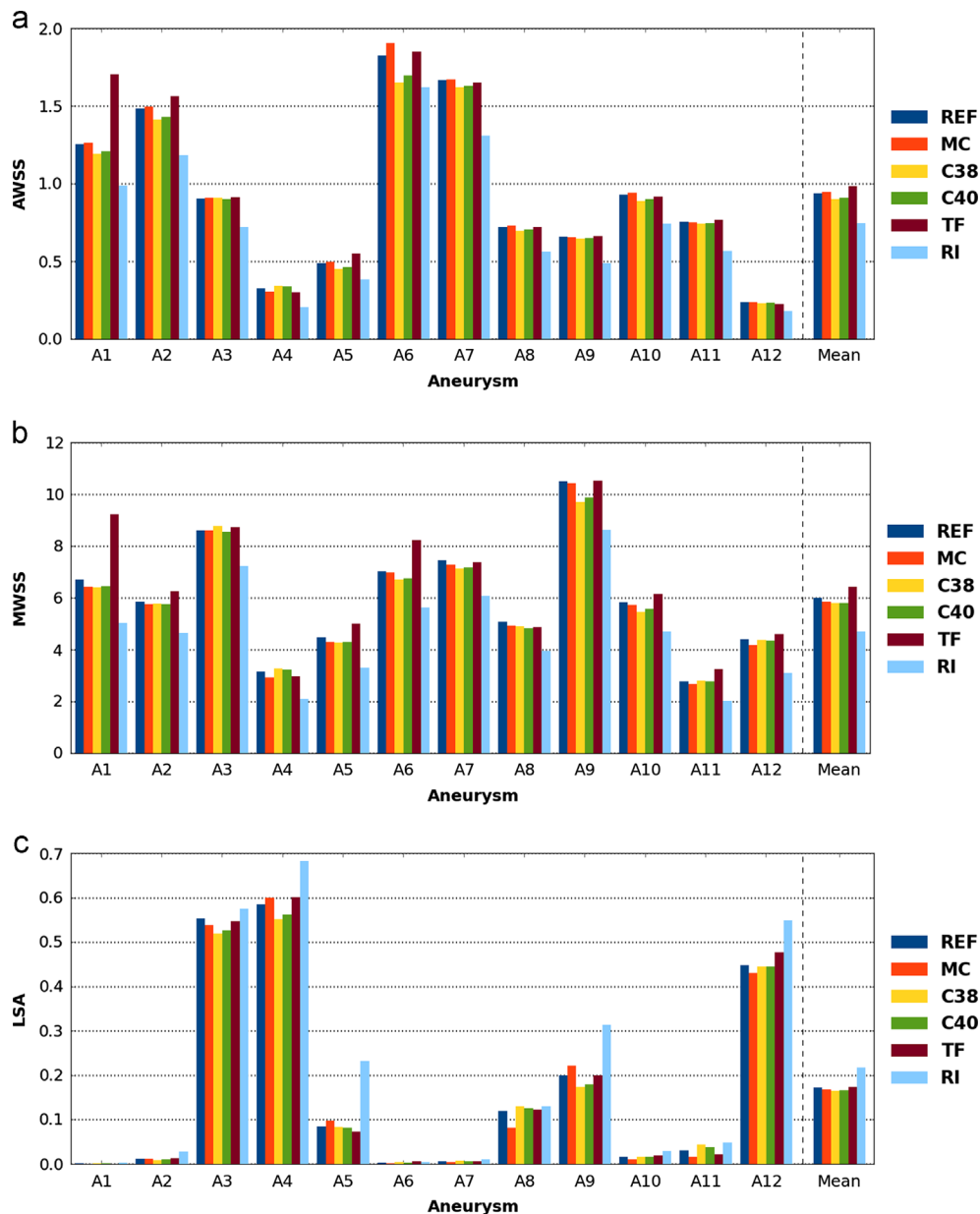


Fig. 4. The different WSS metrics for the different aneurysms, viscosity models and boundary conditions. From top to bottom, the AWSS, MWSS, and LSA values are displayed.

We have assumed the vessel and aneurysm walls to be rigid and impermeable, which is reasonable for flow and WSS prediction in finite segments of large arteries (Steinman, 2012). Furthermore, we have implicitly used the common assumption that the flow is laminar through the choice of the numerical solver and resolution in both time and space, although this assumption has recently been challenged (Valen-Sendstad et al., 2011). Removing these simplifications would require additional patient-specific parameters to be determined and cause a significant increase in computational time. In addition, these chosen simplifications are the most common in clinical studies.

The hematocrit levels vary with age and sex (Jacobsen et al., 2012), with a clear increase in women with increasing age. Women also have increased risk of rupture (Linn et al., 1996; de Rooij et al., 2007) and it is natural to question whether these natural viscosity variations can alter the WSS significantly and perhaps help explain the increased rupture risk. However, as we have seen in this study,

the differences in WSS in MCA aneurysms caused by the different viscosity models are relatively small compared to the WSS variations among the different individuals. The sex differences in rupture risk may be related to the fact that women on an average have vessels with smaller diameters than men (Lindekleiv et al., 2010). We found a medium correlation between sex and vessel diameter and aneurysms volume.

The recent works (Baharoglu et al., 2012; Valen-Sendstad et al., 2012b) suggest that the flow differs in bifurcation and sidewall aneurysms. However, in our current study, there are only weak correlations between the aneurysm type and the different metrics.

Recently, clinical researchers have expressed scepticism towards CFD analysis despite years of enthusiasm. The scepticism arose mainly because of the overwhelming number of models and flow characterizations described in a rapidly growing number of papers on the topic, c.f. e.g. the editorial in AJNR (Kallmes, 2012) and its response from CFD practitioners (Robertson and Watton, 2012;

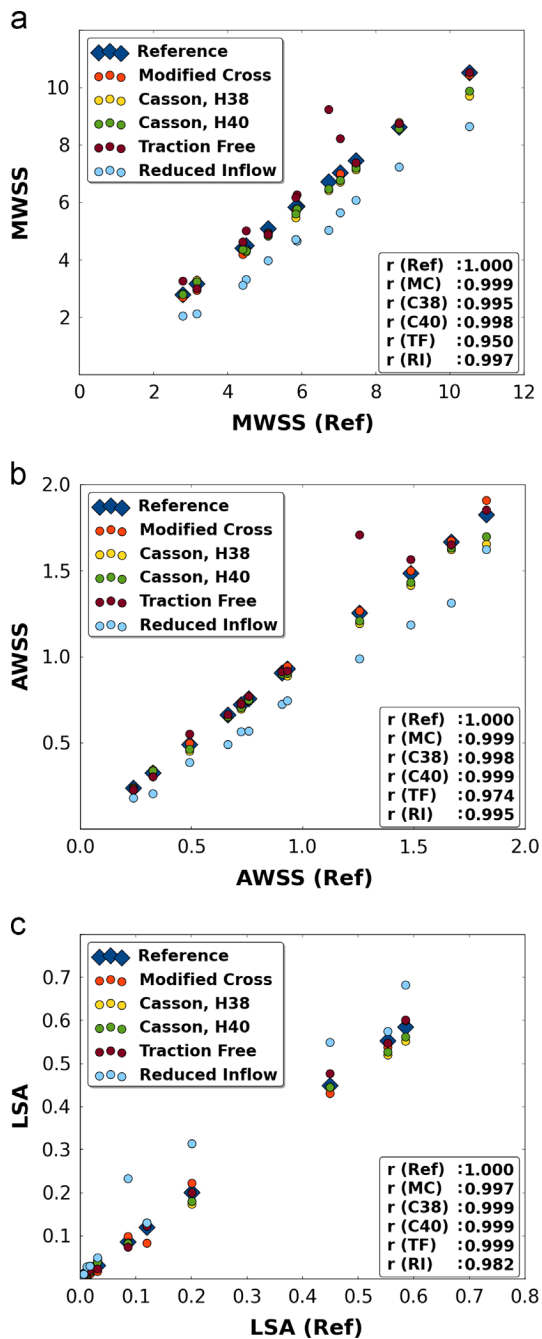


Fig. 5. Scatterplots of each metric, comparing the values from the reference case with those obtained by the other cases.

Table 4

Correlations between parent vessel diameter, aneurysm type, sex, aneurysm volume, aspect ratio, size ratio, MWSS, AWSS, and LSA for the reference simulations.

	D	Type	Sex	V	AR	SR	MWSS	AWSS	LSA
D	1.00	0.01	0.47	0.59	-0.21	0.08	0.50	0.70	-0.38
Type		1.00	-0.13	-0.32	0.28	-0.12	0.07	-0.36	0.15
Sex			1.00	0.48	0.09	0.30	0.13	0.44	-0.19
V				1.00	-0.05	0.60	0.07	0.21	-0.21
AR					1.00	0.71	0.38	-0.52	0.72
SR						1.00	0.19	-0.39	0.50
MWSS							1.00	0.40	-0.06
AWSS								1.00	-0.63
LSA									1.00

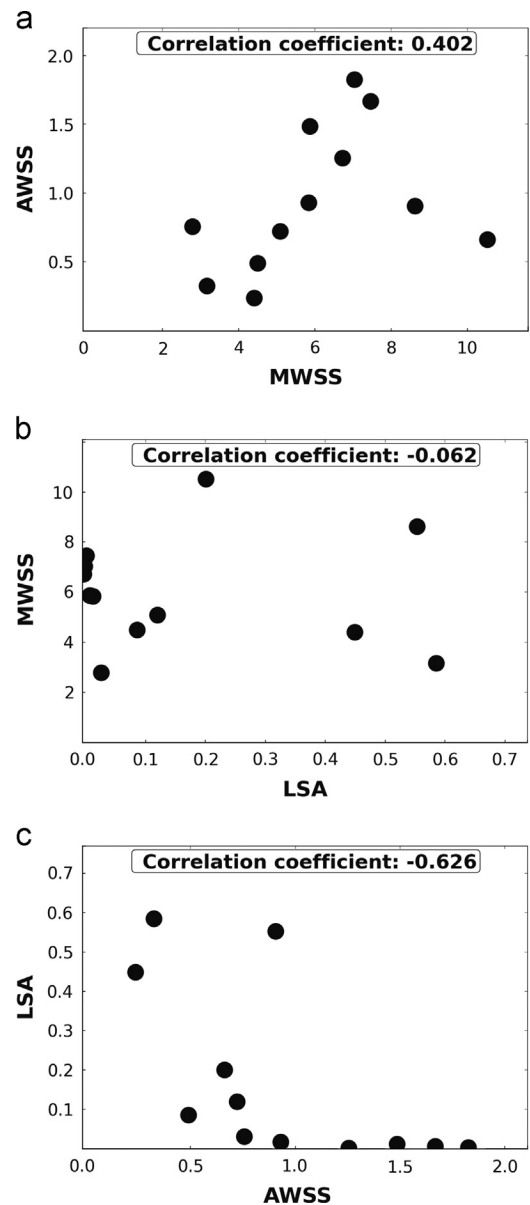


Fig. 6. Scatterplots of the different WSS metrics for the references simulations.

Cebral and Meng, 2012). Based on our study, different WSS metrics do not have strong correlation and it is therefore important to find the right WSS metrics. On the other hand, the different viscosity models and boundary conditions correlate strongly.

5. Conclusion

This study shows that the different viscosity models and boundary conditions correlate strongly for three different WSS metrics. The correlation between the different WSS metrics ranges from weak to medium. No strong correlations were found between the different WSS metrics and the geometrical metrics or classifications.

Conflict of interest statement

All authors declare that there are no conflicts of interest.

Acknowledgements

This work has been supported by Research Council of Norway through grant no. 209951 and a Center of Excellence grant awarded to the Center for Biomedical Computing at Simula Research Laboratory.

References

- Alastruey, J., Parker, K., Peiro, J., Byrd, S., Sherwin, S., 2007. Modelling the Circle of Willis to assess the effects of anatomical variations and occlusions on cerebral flows. *Journal of Biomechanics* 40, 1794–1805.
- Baharoglu, M.I., Lauric, A., Gao, B.L., Malek, A.M., 2012. Identification of a dichotomy in morphological predictors of rupture status between sidewall-and bifurcation-type intracranial aneurysms. *Journal of Neurosurgery* 116, 871–881.
- Bazilevs, Y., Hsu, M.C., Zhang, Y., Wang, W., Kvamsdal, T., Hentschel, S., Isaksen, J., 2010. Computational vascular fluid–structure interaction: methodology and application to cerebral aneurysms. *Biomechanics and Modeling in Mechanobiology* 9, 481–498.
- Boussel, L., Rayz, V., McCulloch, C., Martin, A., Acevedo-Bolton, G., Lawton, M., Smith, R.H.W.S., Young, W.L., Saloner, D., 2008. Aneurysm growth occurs at region of low wall shear stress: patient-specific correlation of hemodynamics and growth in a longitudinal study. *Stroke* 39, 2997–3002.
- Cebral, J., Meng, H., 2012. Counterpoint: realizing the clinical utility of computational fluid dynamics—closing the gap. *American Journal of Neuroradiology* 33, 396–398.
- Cebral, J., Mut, F., Weir, J., Putman, C., 2011a. Association of hemodynamic characteristics and cerebral aneurysm rupture. *American Journal of Neuroradiology* 32, 264–270.
- Cebral, J., Mut, F., Weir, J., Putman, C., 2011b. Quantitative characterization of the hemodynamic environment in ruptured and unruptured brain aneurysms. *American Journal of Neuroradiology* 32, 145–151.
- Chen, J., Lu, X.Y., 2006. Numerical investigation of the non-Newtonian pulsatile blood flow in a bifurcation model with a non-planar branch. *Journal of Biomechanics* 39, 818–832.
- Chien, S., 2007. Mechanotransduction and endothelial cell homeostasis: the wisdom of the cell. *American Journal of Physiology – Heart and Circulatory Physiology* 292, 1209–1224.
- Dintenfass, L., 1985. Red cell rigidity, Tk, and filtration. *Clinical Hemorheology* 5, 241–244.
- Evju, Ø., 2011. Sensitivity Analysis of Simulated Blood Flow in Cerebral Aneurysms. Master's Thesis. DUO, University of Oslo.
- Ford, M., Hoi, Y., Piccinelli, M., Antiga, L., Steinman, D.A., 2009. An objective approach to digital removal of saccular aneurysms: technique and applications. *British Journal of Radiology* 82, 55–61.
- Gambaruto, A.M., Janela, J., Moura, A., Sequeira, A., 2011. Sensitivity of hemodynamics in a patient specific cerebral aneurysm to vascular geometry and blood rheology. *Mathematical Biosciences and Engineering* 8, 409–423.
- Goda, K., 1979. A multistep technique with implicit difference schemes for calculating two- or three-dimensional cavity flows. *Journal of Computational Physics* 30, 76–95.
- Hoi, Y., Gao, L., Tremmel, M., Paluch, R., Siddiqui, A., Meng, H., Mocco, J., 2008. In vivo assessment of rapid cerebrovascular morphological adaptation following acute blood flow increase. *Journal of Neurosurgery* 109, 1141–1147.
- Isaksen, J.G., Bazilevs, Y., Kvamsdal, T., Zhang, Y., Kaspersen, J.H., Waterloo, K., Romner, B., Ingebrigtsen, T., 2008. Determination of wall tension in cerebral artery aneurysms by numerical simulation. *Stroke* 39, 3172–3178.
- Jacobsen, B.K., Eggen, A.E., Mathiesen, E.B., Wilsgaard, T., Njølstad, I., 2012. Cohort profile: the Tromsø study. *International Journal of Epidemiology* 41, 961–967.
- Jiang, J., Johnson, K., Valen-Sendstad, K., Mardal, K.A., Wieben, O., Strother, C., 2011. Flow characteristics in a canine aneurysm model: a comparison of 4-D accelerated phase-contrast MR measurements and computational fluid dynamics simulations. *Medical Physics* 38, 6300–6313.
- Jou, L., Lee, D., Morsi, H., Mawad, M., 2008. Wall shear stress on ruptured and unruptured intracranial aneurysms at the internal carotid artery. *American Journal of Neuroradiology* 29, 1761–1767.
- Kallmes, D., 2012. Point CFD—computational fluid dynamics or confounding factor dissemination. *American Journal of Neuroradiology* 33, 395–396.
- Krejza, J., Szydlak, P., Liebeskind, D.S., Kochanowicz, J., et al., 2005. Age and sex variability and normal reference values for the VMCA/VICA index. *American Journal of Neuroradiology* 26, 730–735.
- Lee, S.W., Steinman, D.A., 2007. On the relative importance of rheology for image-based CFD models of the carotid bifurcation. *Journal of Biomechanical Engineering* 129, 273–278.
- Lindekleiv, H.M., Valen-Sendstad, K., Morgan, M.K., Mardal, K.A., et al., 2010. Sex differences in intracranial arterial bifurcations. *Gender Medicine* 7, 149–155.
- Linn, F., Rinkel, G., Algra, A., van Gijn, J., 1996. Incidence of subarachnoid hemorrhage: role of region, year, and rate of computed tomography: a meta-analysis. *Stroke* 27, 625–629.
- Logg, A., Mardal, K.A., Wells, G.N., 2011. Automated Solution of Differential Equations by the Finite Element Method. Springer.
- Miura, Y., Ishida, F., Umeda, Y., Tanemura, H., Suzuki, H., Matsushima, S., Shimozaki, S., Taki, W., 2013. Low wall shear stress is independently associated with the rupture status of middle cerebral artery aneurysms. *Stroke* 44, 519–521.
- Rinkel, G.J.E., Djibuti, M., Algra, A., van Gijn, J., 1998. Prevalence and risk of rupture of intracranial aneurysms: a systematic review. *Stroke* 29, 251–256.
- Robertson, A., Watton, P., 2012. Computational fluid dynamics in aneurysm research: critical reflections, future directions. *American Journal of Neuroradiology* 33, 992–995.
- Robertson, A.M., Sequeira, A., Owense, R.G., 2009. Rheological models for blood. In: Formaggia, L., Quarteroni, A., Veneziani, A. (Eds.), *Cardiovascular Mathematics. Modeling and Simulation of the Circulatory System*. Springer-Verlag, Italia, Milano, pp. 211–241.
- de Rooij, N., Linn, F., van der Plas, J., Algra, A., Rinkel, G.J.E., 2007. Incidence of subarachnoid haemorrhage: a systematic review with emphasis on region, age, gender and time trends. *Journal of Neurology, Neurosurgery and Psychiatry* 78, 1365–1372.
- le Roux, A., Wallace, M., 2010. Outcome and cost of aneurysmal subarachnoid hemorrhage. *Neurosurgery Clinics of North America* 21, 235–246.
- Schievink, W.I., 1997. Intracranial aneurysms. *New England Journal of Medicine* 336, 28–40.
- Steinman, D.A., 2012. Assumptions in modelling of large artery hemodynamics. In: *Modeling of Physiological Flows*. Springer, pp. 1–18.
- Valen-Sendstad, K., 2011. Computational Cerebral Hemodynamics. Ph.D. Thesis. University of Oslo.
- Valen-Sendstad, K., Logg, A., Mardal, K.A., Narayanan, H., Mortensen, M., 2012a. A comparison of finite element schemes for the incompressible Navier–Stokes equations. In: Logg, A., Mardal, K.A., Wells, G.N. (Eds.), *Automated Solution of Differential Equations by the Finite Element Method*. Springer, pp. 399–420.
- Valen-Sendstad, K., Mardal, K.A., Mortensen, M., Reif, B.A.P., Langtangen, H.P., 2011. Direct numerical simulation of transitional flow in a patient-specific intracranial aneurysm. *Journal of Biomechanics* 44, 2826–2832.
- Valen-Sendstad, K., Mardal, K.A., Steinman, D.A., 2012b. High-resolution CFD detects high-frequency velocity fluctuations in bifurcation, but not sidewall, aneurysms of the middle cerebral artery. *Journal of Biomechanics* 46, 402–407.
- Xiang, J., Natarajan, S.K., Tremmel, M., Ma, D., Mocco, J., Hopkins, L.N., Siddiqui, A., Levy, E.I., Meng, H., 2011. Hemodynamic-morphologic discriminants for intracranial aneurysm rupture. *Stroke* 42, 144–152.
- Xiang, J., Tremmel, M., Kolega, J., Levy, E.I., Natarajan, S.K., Meng, H., 2012. Newtonian viscosity model could overestimate wall shear stress in intracranial aneurysm domes and underestimate rupture risk. *Journal of Neurointerventional Surgery*, 351–357.
- Yeow, Y.L., Wickramasinghe, S.R., Leong, Y.K., Han, B., 2002. Model-independent relationships between hematocrit, blood viscosity, and yield stress derived from Couette viscometry data. *Biotechnology Progress* 18, 1068–1075.

Book chapter

On the Assumption of Laminar Flow in Physiological Flows: Cerebral Aneurysms as an Illustrative Example

Øyvind Evju and Kent-Andre Mardal.

*In Modeling the Heart and the Circulatory System,
volume 14, pages 177–195. 2015.*

On the Assumption of Laminar Flow in Physiological Flows: Cerebral Aneurysms as an Illustrative Example

Øyvind Evju and Kent-Andre Mardal

Abstract In physiological fluid flows, except for in the heart and the aorta, the Reynolds numbers are moderate (below 1000). This is far below the typical point of transition in pipe flow, which occurs around Reynolds number 2300. Because of this, laminar flow is commonly assumed in the modelling of these flows, resulting in computational methods tailored for this flow regime.

This chapter presents a critical review of this assumption, and both clinical and numerical evidence of transitional physiological flows are presented. The pulsatility and complex geometries in physiological flow are highlighted as the main reasons for a lower transition point in physiological flows.

Furthermore, we discuss the threshold of transition in a particular case of an aneurysm with respect to resolution, Reynolds number and non-Newtonian viscosity modelling.

7.1 Introduction

Most fluid flows in our human body, except for the blood flow in heart and aorta, are believed to be laminar in healthy individuals. A good reason for this, from an evolutionary point of view, is that turbulence introduces extra friction and hence transport is more efficient in the laminar regime than in the turbulent regime. It has also been shown that laminar flow ensures a healthy mechanotransduction¹ in the vessel walls. On the other hand, various pathologies, like for example atheroscle-

Ø. Evju

Simula Research Laboratory, P.O. Box 134, 1325 Lysaker, Norway
e-mail: oyvinev@simula.no

K.-A. Mardal ()

Simula Research Laboratory, P.O. Box 134, 1325 Lysaker, Norway and
Department of Informatics, University of Oslo, P.O. Box 1080 Blindern 0316 Oslo, Norway
e-mail: kent-and@simula.no

¹ Mechanotransduction refers to the process where cells convert mechanical stimuli to chemical activity and is vital in the remodelling that occur in vessels.

rosis and aneurysms, involve anatomies causing disturbed flow and possibly even turbulent flow. The disturbances trigger a downward spiral where the disturbed flow leads to an unhealthy mechanotransduction causing remodelling of the vasculature which again worsen the flow disturbances. Recent research has therefore challenged the assumption of laminar flow in such pathologies and put the focus on the possible role of transitional or turbulent flow in these pathologies.

Transition to turbulence in steady pipe flow occurs at Reynolds number (Re) around 2300, while fully developed turbulence is obtained around 4000. The Reynolds number in large arteries and also elsewhere in our body is usually far below 2300 and laminar flow is therefore usually assumed. However, both the pulsatile nature of the flow and deviations from straight pipe geometry might introduce transition to turbulence at lower Reynolds numbers, as we will demonstrate in this chapter.

While the laminar regime and in many applications the fully developed turbulent regime are reasonably well understood from both a modelling and numerical point of view, the transitional regime with occasional turbulence poses additional challenges. Modelling is difficult in particular, because it is challenging to precisely predict the onset of the turbulent spots. Instead of modelling the turbulence, one might increase the resolution in space and time and resolve all scales of the turbulent flow numerically, a technique called direct numerical simulation (DNS). This approach is feasible only for flows with moderate Reynolds numbers because resolving the small structures (Kolmogorov microscales) induces computational costs scaling as Re^3 . In addition to the high resolution requirement, it is necessary to employ schemes that introduce as little dissipation as possible. It may also be necessary to carefully construct the boundary conditions such that these allow for or induce small perturbations or unstable modes that may grow into turbulence. In numerical simulations that do not sufficiently address these requirements, transition is often not seen even though physical experiments reveal them under similar flow conditions.

This chapter is devoted to a critical review on the assumption of laminar flow in physiological flow applications and we will use blood flow in cerebral aneurysms as an illustrating example. We will discuss the consequences of this assumption, which lowers the requirement on the resolution and validates the use of stabilization techniques and time discretizations with dissipation. We will also review clinical and biomechanical findings suggesting that transitional flow is common or at least not unusual in many pathologies. Finally, we discuss cerebral aneurysms in depth and show that for some aneurysms transition may occur already for Reynolds number as low as 300.

7.2 On the Definition of Turbulence

Defining and identifying transitional or turbulent flow in a pulsatile and complex 3D geometry is a challenging task. For completeness we include a formal definition of turbulence:

Turbulent flow is an irregular condition of flow in which the various quantities show a random variation with time and space coordinates, so that statistically distinct average values can be discerned.

The above definition was provided in [18] and later Bradshaw adds an important observation; namely that *turbulence has a wide range of scales*. See for example [46] for discussions concerning this definition. Following this definition we consider random fluctuations on a wide range of scales as the defining characteristics of turbulence. Laminar flow on the other hand is characterized as smooth and deterministic.

Between the regimes of laminar and fully developed turbulent flows there is a regime with complex flow such as occasional turbulence or spots of turbulence that is often called the transitional regime. According to White [45, p. 344] most analyses are devoted to either the fully developed turbulent regime or the laminar regime and engineers are advised to avoid the transitional regime. While engineers may choose to avoid this regime, several diseased states may lead to transitional flow and the unpredictability of transition may even be a factor that worsen the condition, as will be discussed in the following.

The distinction between laminar, transitional and turbulent flow dates back to 1883 when Osbourne Reynolds observed that the flow condition was governed by the ratio of inertial forces to viscous forces (the Reynolds number) in stationary pipe flow. In his famous experiments Reynolds showed that transition to turbulence in stationary pipe flow occurs at $Re=2300$ and fully developed turbulence is achieved at $Re=4000$. Subsequent experiments have shown that turbulence might be suppressed until $Re=40\ 000$ given sufficiently smooth pipe, inflow and outflow. On the other hand, the lower limit seems to be about 2000 [31].

Transitional or turbulent flow causes extra friction. For example, in stationary pipe flow the pressure drop needed to drive the flow under laminar conditions scales as V , where V is the mean flow, while in transitional or turbulent flow the pressure drop scales as $\approx V^{1.75}$. This was observed by Hagen in 1839. In pipe flow the transition point is clearly defined as the pressure drop increases from V and $V^{1.75}$ and it occurs around around Reynolds number 2100. The sharpness of the transition point suggests that the pressure drop might give insight into the precise transition point and we will therefore also discuss pressure drops in the following.

Pulsatility may both increase and decrease the threshold for transition. In particular, flow deceleration typically promote transition, while acceleration delay transition. Concerning flow in straight pipes, it was demonstrated in [40] that transition to turbulence is highly dependent on the Womersley number. Of particular importance for physiological flow is the fact that the transitional regime occur early for Womersley numbers between 2–5, numbers that are physiologically reasonable. Alternative definitions of the Reynolds number that put the focus on the pulsatility was proposed in this publication.

Probably even more important than the pulsatility is the geometry. For instance, in Couette flow or flow around cylinders, transition occurs at $Re=500$ and $Re=300$, respectively. For this reason a wide range of other Reynolds numbers has also been

proposed in the literature, see [31] for an overview, but it remains difficult to employ these numbers as guidelines for when transition occurs in the complex vasculature of the body. Still, many works consider the Reynolds number as an important guideline for whether the flow is laminar or not and justify their laminar assumption by a Reynolds number calculation.

7.3 Clinical Observations

Clinically, turbulent blood flow has been observed *in vivo* associated with the heart valves, the ascending aorta, and in arteriovenous grafts. Audible sounds (20-20 000 Hz) caused by the high frequency pressure fluctuation of turbulence are for some conditions symptoms of severely disturbed flow. For instance heart murmurs are associated with turbulence generated by malfunctioning mitral valves or a stenosed aorta. Arteriovenous grafts sometimes produce audible thrills at frequencies 100-200 Hz caused by vein wall vibration.

Turbulence or transition have received less attention in other pathologies like atherosclerosis and aneurysms, but there are still significant evidence in the clinical literature suggesting that it is common or at least not unusual. For example, severe stenosis in the carotid artery can result in transition to turbulent flow, which may produce an audible sound (bruit) that physicians can detect. Another manifestation of turbulence is pulsatile tinnitus, or tinnitus that is synchronous with a person's heartbeat, which are audible sounds that is transmitted to the inner ear [15]. This condition is likely caused by the abnormal blood flow associated with conditions such as arteriovenous malformations, stenosed carotid arteries, cerebral aneurysms etc. The topic of pulsatile tinnitus in association with cerebral aneurysms dates back to 1936 where Bergstrand et.al. [6] demonstrated pulsatile tinnitus in 4 of 22 cases of intra cranial aneurysms. While their relative high fraction of pulsatile tinnitus per aneurysms have been challenged in, e.g. Beadles [5], several recent studies report that pulsatile tinnitus is indeed present and caused by aneurysms [3, 35]. Pulsatile tinnitus, both subjective (as experienced by the patients) and objective (detected by the clinician), does however require that the sounds generated by the turbulent or transitional flow are transmitted either to the patients inner ear or through the skull for detection. To improve the sound detection procedure, Ferguson employed a phonocatheter on the exposed aneurysm during craniotomy and found that 10 out of 17 aneurysms had bruits of sounds with predominate frequencies in the range of 270 to 660 Hz [10]. This suggests that a significant fraction of aneurysms may have transitional blood flow.

Clinicians have performed various glass model studies to consider the issue of turbulence in blood flow. Already in 1958, Stehbens [36] investigated the transition threshold in idealized bifurcations and S-shaped arteries modelling the carotid siphon. The critical Reynolds numbers in the bifurcation and the S-shaped geometry were 600 and 900, respectively. In all cases he used stationary inflow conditions. Later, in 1972, Roach et.al. [29] considered bifurcations and bifurcations with

aneurysms at the apex using glass models and found that turbulence was present in bifurcations (depending on the angle of the bifurcation) at $Re=1200$ under steady conditions and around 800 under pulsatile condition. In aneurysms transition occurred already at Reynolds numbers between 400 and 500, with only a slight difference between stationary and pulsatile flow.

7.4 Mechanotransduction and the Remodelling of the Vasculature

The vasculature is an active system that adapt to facilitate a healthy blood flow. In particular, it seems that the arterial system adapt vessel radius to a flow that on average has a uniform wall shear stress (WSS) of around 5 Pa [13]. This finding is called the uniform WSS hypothesis and has been found to apply to most parts of the cardiovascular systems. Furthermore, bifurcations in most part of the vasculature have angles and radii that satisfy an optimum principle known as Murray's law. This law states that the energy requirements for metabolism and transport are minimized in blood flow. Murray used this optimum principle to derive a relationship between angles and radii in bifurcations and this relationship has been validated in various parts of the cardiovascular in e.g. rats, dogs and humans [32, 48]. This law suggest that the cardiovascular system is tuned to be cost efficient. However, a notable exception from this law is the bifurcations associated with the circle of Willis, where cerebral aneurysms form [1, 20]. Hence, large parts of the vasculature appear to be constructed for an energy efficient transport of blood throughout the body. Moreover, the vasculature plays an active role and remodel itself to optimize the flow and maintain a uniform WSS. An example of this process can be found in [19, 26]. Here, the authors surgically closed both of the carotid arteries in a rabbit. The consequence was an increased flow of about 400% in the basilar artery. Over the course of a week, the artery grew radially until a baseline WSS was again obtained and the artery remained rather unchanged in the following weeks. Complex geometries like many bifurcations lead to deviations from the principle of uniform WSS and are particularly prone to e.g. atherosclerosis [23] and aneurysms [1]. These complex geometry also often cause early transition.

Research on the mechanotransduction, the process where living cells turn mechanical stimuli to chemical signals, have firmly established that endothelial cells (EC), the cells that surface the innermost layer of the blood vessels, play an active role in the remodelling of blood vessels. Experiments have shown that EC respond to flow, and in particular that undisturbed flow leads to healthy remodelling, while disturbed or oscillating flow fail to do so [4, 7]. Turbulent shear stress also substantially increases the endothelial cell turnover when compared to laminar flow with similar shear [8].

It is however an open question at what time scales the mechanotransduction occur. The biomechanical signalling of EC involves reaction-diffusion process that are slow (tens of seconds) compared to the high-frequency fluctuations in blood flow.

However, recent research suggest that the mechanical signaling can be transmitted more rapidly (within 100 ms) through the cytoskeletal filaments within the EC layer and allow for rapid transmission over longer distances. Furthermore, there is evidence that also the medial and adventitial layers are responsive to this mechanical signalling [4]. It is, however, not known precisely how the various vessel layers remodel themselves and to what extent there are individual variations in the mechanotransduction and remodelling.

Finally, turbulent blood flow introduce clot formation. In fact, in [37] they generated turbulent flow in canine models and it was found that the weight of the thrombosis was proportional to the Reynolds number and turbulence intensity.

7.5 Modelling of Blood Flow

Blood is a suspension of blood cells, platelets and plasma and does therefore not necessarily display a Newtonian rheology. A wide range of different models have been proposed and analysed, see e.g. [30]. For blood flow in larger arteries and aneurysms, Newtonian models typically capture the main flow quite accurately, for example maximal WSS, average WSS and area of low WSS correlate strongly (>0.95) between Newtonian and commonly used non-Newtonian models [9], but may overestimate WSS in areas of low shear [47].

In large arteries there is also a pulsatile response in the vessel to the blood flow, and this fluid-structure interaction has been the subject of many recent publications [27, 28]. The pressure propagation throughout the vasculature can only be described by fluid-structure interaction models, but there is evidence that the main flow in localized regions can often be modelled by assuming rigid vessels. The main reason for this is that for localized vessel segments the whole segment deforms in synchrony [38]. Hence, for modelling of main flow features in large localized arteries it appears that Newtonian modelling with rigid vessels may be adequate under the assumption of laminar flow, bearing in mind the large flow differences caused by the geometrical variations between different patients.

The previously mentioned studies that report turbulence, all consider Newtonian flow within rigid geometries. However, both non-Newtonian viscosity and fluid-structure interaction may both delay or accelerate transition. From an engineering point of view, delay of transition has been a hot topic for over 50 years because of its potential to reduce drag and suppress noise.

Concerning transition and fluid-structure interaction, Kramer [22] demonstrated already in 1960 that compliant coating, based on the dolphin's epidermis, may substantially delay transition. Naturally, this spurred a lot of research activity, which mostly failed to reproduce the drag reduction demonstrated by Kramer. Now, more than 50 years after the initial experiments of Kramer, there is little doubt that compliant coating may delay transition, c.f. e.g., [16]. Reynolds numbers for transition in geometries with compliant coating may exceed corresponding Reynolds numbers for flow within rigid geometries by more than an order of magnitude. However, it is

also clear that delaying transition is delicate and that compliance might even introduce instabilities.

An interesting case here is the audible sounds caused by vein wall vibration in arteriovenous grafts. The vein wall vibration is present *in vivo* and is believed to be caused by high frequency pressure fluctuation in the turbulent blood flow occurring already at Reynolds number as low as 500. However, *in vitro* models and also numerical simulations have failed to demonstrate turbulent flow in models of arteriovenous grafts at such low Reynolds numbers [34]. In fact, the studies suggest that the graft geometry and flow pulsatility are not sufficient to explain the transition at such low Reynolds numbers and it appears that the only likely explanation is either the non-linear viscosity of blood or the compliance of the vessel walls. In particular, the high frequency content of the vortical structures appear to be strongly linked with the natural harmonics of the wall. We also remark that in arteriovenous grafts there is a strong correlation between vein wall vibration and intimal thickening [11], suggesting that the veins are able to sense and react to the turbulence although not in a beneficial manner.

7.6 On the Modelling of Transitional Flow

The process of transition is a difficult topic that has been under intensive research since Reynolds and Hagen did their famous experiments. Transition occurs because unstable modes are triggered, starting often as minor perturbations to the flow that grow either in space, time or both. The Navier-Stokes equations are non-linear and non-normal and a consequence is that the standard approach of stability analysis in terms of eigenvalue fail to predict the occurrence of unstable mode leading to transition. For instance, transition in simple flow problems as Couette and Poiseuille can not be explained in terms the linear analysis of eigenvalues [41]. Because the exact mechanism behind transition (or the procedure to calculate the unstable modes) is not known, it is difficult to model transition using for instance Reynolds averaged Navier-Stokes equations for transition even though they often are powerful tools for fully developed turbulence.

For flow problems such as physiological flow applications where the Reynolds number is moderate, it is usually not possible to predict whether transition will occur or not. The only feasible approach seems to be to perform a DNS. This is, however, challenging for at least three reasons: 1) special care needs to be taken to construct discretization schemes to avoid dissipation, 2) the resolution needs to be extremely high compared to corresponding laminar simulations, and 3) boundary conditions needs to be chosen such that instabilities are allowed.

This is in sharp contrast to simulations where laminar flow is assumed and where most simulations, at least for aneurysms studies, employ first order schemes with built-in dissipation that avoid stability issues [44]. Here, the justification for these schemes is that laminar flow is assumed. Moreover, as [44] points out, convergence studies are not always reported or are performed in a poor fashion. It is therefore

difficult to determine whether transition would occur at a higher resolution in these studies. A recent benchmark study [39], where 25 research groups performed CFD analysis in a prescribed geometry of a cerebral aneurysm with a proximal stenosis given boundary conditions, reveals that the flow varied remarkably inside the aneurysms among the results of the different research groups. There was a clear tendency that simulations with research codes on high resolutions demonstrated flow instabilities to a greater extent than low resolution simulations performed with commercial codes.

Concerning the resolution of the discretization, the requirement of a DNS is that the so-called Kolmogorov scales are resolved. Determining the Kolmogorov scale is challenging from a numerical point of view as it needs to be estimated based on the simulation results, and grid independence of local quantities needs to be established. However, as pointed out in [2], performing DNS studies that concern blood flow is particularly challenging as the Kolmogorov length scale may be on the same scale as the red blood cells and thus it is on the scale where the continuum hypothesis breaks down.

Still, several attempts of DNS studies in carotid arteries [24], arteriovenous grafts [25], cerebral aneurysms [42] have been performed, albeit at a much coarser resolution than the estimates provided in [2]. These simulations report cycle-to-cycle variations on a wide range of scales, e.g., temporal fluctuations in the range of 100–1000 Hz. An important observation is that instabilities seems to be caused by geometry rather than the pulsatility and therefore that stationary inflow/outflow conditions can be used to detect possible transition effects and for grid-independence studies, c.f. e.g. [24, 43, 44]. This is because the pulsatility is relatively slow as compared with the velocities in the sense that the number of flow-throughs per cycle is sufficiently high. However, it has been pointed out that transition most often occurs in the deceleration phase [42]. Simulations with constant flow can therefore be assumed to predict a higher critical Reynolds number, than a similar simulation with pulsatile flow.

7.7 An Illustrating Example: Transition in a Cerebral Aneurysm

To investigate the threshold to transition, we consider an aneurysms from a canine model [21]. The aneurysm, although artificially produced, is a prototype for human aneurysms created by a technique often used in clinical trials. The aneurysm is shown in Fig. 7.1.

The aneurysm model was meshed with 3,275,000 tetrahedra, with a coarser mesh at the distal parts of the geometry. This corresponds to approximately 25–50 cells across the parent artery diameter and 120–150 cells across the diameter of the aneurysm, with an average edge length of 0.137mm. This is not claimed to be fully converged, as Fig. 7.2 illustrates, but it is in the upper range of resolutions used in CFD studies within the field. However, to capture any high-frequency flow effects, the time step was set to $7.5e-6$ s, several orders of magnitude below what is typically



Fig. 7.1. The canine aneurysm that is used in our computations. The dark slice is used to display the flow field, the red dot denoted by a P shows the point used in our analysis of the turbulent characteristics, and the balls A, B1 and B2 are used to calculate the pressure drop over the aneurysm ($\Delta p := \bar{p}_A - \frac{\bar{p}_{B1} + \bar{p}_{B2}}{2}$)

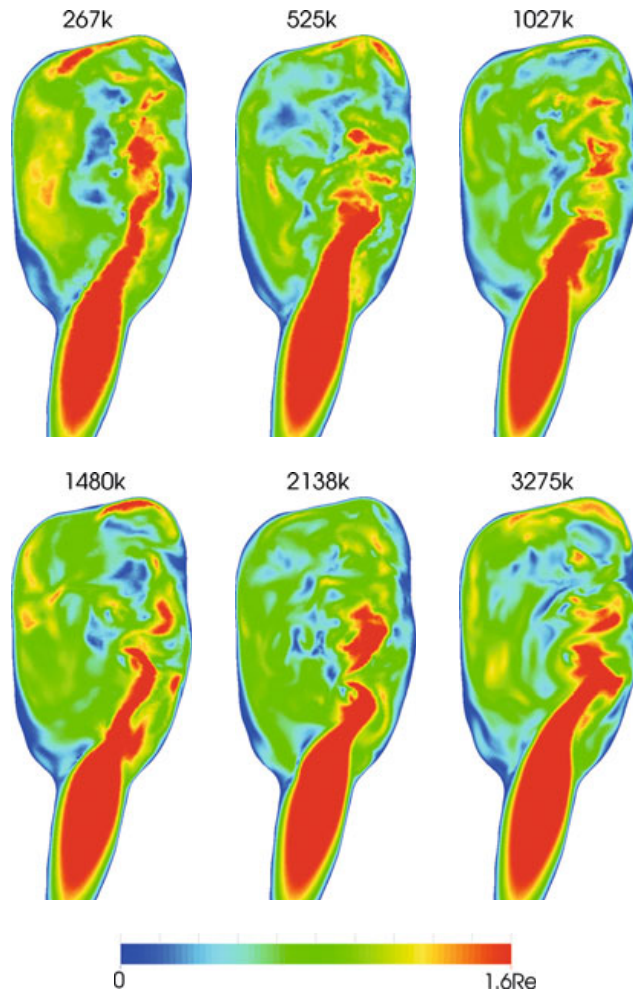


Fig. 7.2. The figure shows the velocity magnitude in a slice through the aneurysm at Reynolds numbers 1000 at various resolutions

employed. Blood was modelled with a density of 1056 kg/m^3 and a Newtonian viscosity of 3.45 mPa s .

Dirichlet boundary conditions were set for the velocity, with no-slip conditions at the walls, and paraboloid-shaped inflows and outflows, with the flow rate distributed evenly between the two outflows. For the pressure, natural boundary conditions were used, and the resulting pressure was normalized around zero.

As was demonstrated in [12, 24], the transition to turbulence in larger arteries is predominantly governed by the geometry rather than the relatively slow pulsatility that merely turns the turbulence on and off. That is, given the relatively long cardiac cycle (> 10 flow-throughs in a typical model), it is preferable to consider the question of turbulence under static conditions, which is done in the following. Notice, however, that while the boundary conditions are static, as the Reynolds number increase, the flow inside the aneurysm and surrounding will not be stationary. In fact, as was demonstrated in [43], we might expect high frequency fluctuations ($> 100 \text{ Hz}$) already at Reynolds numbers around 200–300.

The Navier-Stokes equations were solved with a finite element incremental pressure correction scheme, following the idea of [14]. The scheme applies a Crank-Nicolson method for the time stepping and a linear handling of the convection term as introduced by [33], making the tentative velocity step second order in both time and space. This scheme is chosen because it preserves the exact same stability properties as Navier-Stokes and hence does not introduce additional dissipation in the flow. The scheme reads as:

At $t = t^{n+1} := (n + 1)\Delta t$ with the solution $(u^k, p^k) := (u(t^k), p(t^k))$ known for $k = 0, \dots, n$, kinematic viscosity ν , and density ρ , do

1. Solve a reaction-diffusion-advection equation for a tentative velocity, \tilde{u}^{n+1} :

$$\frac{1}{\Delta t} (\tilde{u}^{n+1} - u^n) - \nabla \cdot \nu \nabla \tilde{u}^{n+\alpha} + u^* \cdot \nabla \tilde{u}^{n+\alpha} + \nabla p^{n-1} = 0,$$

where

$$\begin{aligned} \tilde{u}^{n+\alpha} &= \alpha \tilde{u}^{n+1} + (1 - \alpha) u^n \quad (\alpha = \frac{1}{2} \text{ for Crank-Nicolson}), \\ u^* &= \frac{3}{2} u^n - \frac{1}{2} u^{n-1}. \end{aligned}$$

2. Solve a Poisson equation for the pressure, p^{n+1} :

$$\Delta p^{n+1} = \Delta p^n + \frac{\rho}{\Delta t} \nabla \cdot \tilde{u}^{n+1}.$$

3. Update for the correct velocity, u^{n+1} :

$$u^{n+1} = \tilde{u}^{n+1} - \frac{\Delta t}{\rho} \nabla (p^{n+1} - p^n).$$

4. Increment ($n \leftarrow n + 1$) and repeat.

The scheme was implemented in the open source software package FEniCS², and is available through the open source CFD package *cbc.flow*³. Linear elements were used for both velocity and pressure.

We first ran simulations at a coarser time resolution to obtain steady state solutions to be used as initial condition for our main simulations with 0.2 to 6 flow-throughs depending on the Reynolds number. We then disregarded the first 5000 time steps of our main simulations to allow for the finer time scales to reach a quasi-steady state.

To analyse the turbulent characteristics of the flow over time, we analyse the power spectral density (PSD) of the velocity magnitude in a point of the interior of the aneurysm sac, as shown in Fig. 7.1. The PSD for a discrete time-signal is as follows. Let

$$S_{xx}(\omega) = \frac{(\Delta t)^2}{T} \left| \sum_{n=1}^N x_n e^{-i\omega n} \right|^2,$$

where ω is the frequency, Δt is the time step, T is the time interval, N is the number of samples and x_n denotes the sample at $t = n\Delta t$. Since the velocity magnitude is real-valued, the PSD is symmetric, i.e. $S_{\|\mathbf{u}\|\|\mathbf{u}\|}(\omega) = S_{\|\mathbf{u}\|\|\mathbf{u}\|}(-\omega)$. We therefore define $PSD_{\|\mathbf{u}\|}$ as

$$PSD_{\|\mathbf{u}\|}(\omega) := 2S_{\|\mathbf{u}\|\|\mathbf{u}\|}(\omega), \quad \omega > 0.$$

This is related to the sample variance of $\|\mathbf{u}\|$ with the relation

$$\sigma^2 = \int_0^\infty PSD_{\|\mathbf{u}\|}(\omega) d\omega.$$

Thus, $PSD_{\|\mathbf{u}\|}$ can provide information about which frequencies are required to resolve, in our case, the pointwise velocity magnitude. In the following, we report $\omega_{0.95}$ as the approximate frequency that is required to capture 95% of the variance, that is,

$$\int_0^{\omega_{0.95}} PSD_{\|\mathbf{u}\|}(\omega) d\omega = 0.95\sigma^2.$$

Given our time stepping, we are limited by the Nyquist frequency of $\frac{1}{2\Delta t} \approx 66667$ Hz. The number of bins in the discrete Fourier transform are given by $T\frac{1}{2\Delta t} = 20000$, and the bin size is thus 3.33 Hz.

The PSD analysis seen in Fig. 7.3 revealed a significant change in the frequencies of the flow between $Re=250$ and $Re=500$. When $Re < 250$, $\omega_{0.95}$ is less than 60 Hz, but this jumps to 313 Hz at $Re=500$ and further to 923 Hz and 2046 Hz at $Re=1000$ and $Re=2000$, respectively. To capture any flow effects at these frequencies, the resolution requirements are minimum twice the reported frequency. However, this is no guarantee for the *correct* flow effects at these frequencies. It should also be noted that when considering pulsatile flows, the frequencies present in the flow are likely

² <http://fenicsproject.org>

³ https://bitbucket.org/simula_cbc/cbcflow

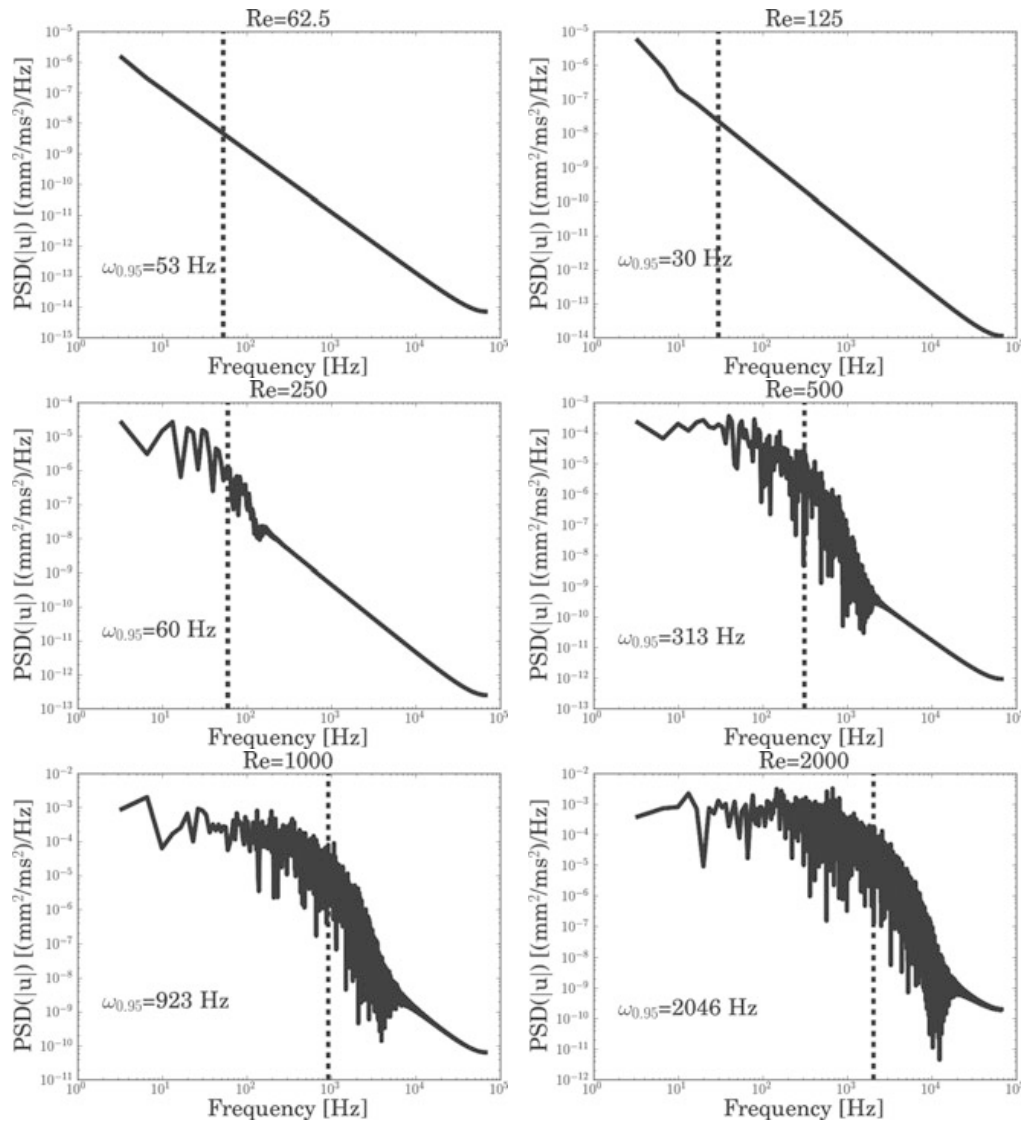


Fig. 7.3. The figure shows the power spectrum of a point in the aneurysm at different Reynolds numbers

significantly higher, due to the deceleration phase of the flow at late systole/early diastole.

Considering the slice views in Fig. 7.4, the pattern is clearly seen of the increasing complexity in the flow from $Re = 250$ and upwards. Worth noting is also the flow field in the parent artery, which appears laminar as expected.

While blood displays non-Newtonian rheology, in many CFD studies the shear rates are assumed adequately high to assume a Newtonian behaviour. While this assumption is often adequate [9], its effect on the transition of flow has not been studied. To address this, we employ a Modified Cross viscosity presented in Fig. 7.5. The model parameters are fitted to viscometer data [30], and the computation was done explicitly. We re-ran simulations at the flow rates corresponding to $Re=250$ and

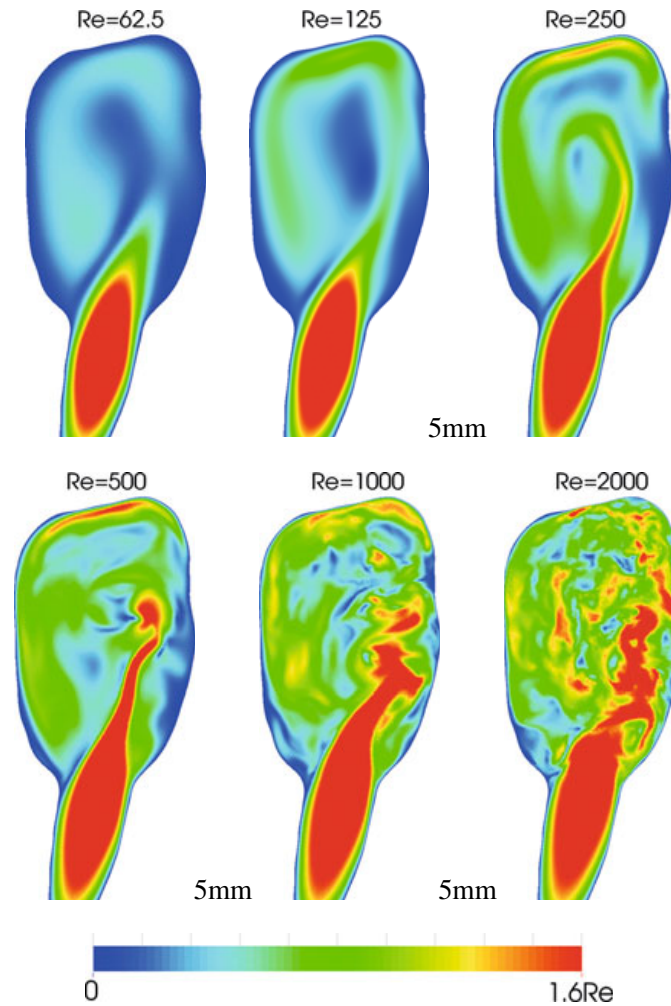


Fig. 7.4. The figure shows the velocity magnitude in a slice through the aneurysm at different Reynolds numbers

Re=500 in the Newtonian case. Since the flow rates are equal, but the viscosity is not, the actual Reynolds number is somewhat lower for the non-Newtonian case. The Reynolds number will be similar to the Newtonian case in the parent artery, where the shear rate is high, but will change in the parts of the geometry where the shear rate drops. On average, the Modified Cross model predicted 20% higher viscosity compared to the Newtonian case.

The resulting PSD can be seen in Fig. 7.6, with slice-views of the flow in Fig. 7.7. Keeping in mind the effects on the Reynolds number, it would appear that the non-Newtonian viscosity model delays the transition of the flow significantly.

In pipe flow the transition to turbulence is clearly identified by a marked change in the pressure drop relation to velocity. The pressure drop increases linearly as the velocity (or Reynolds number) increase in laminar flow, but has a sharp point of transition that occur around Re=2000 after which the pressure drop grows like $\approx V^{1.75}$, see e.g. Fig. 6.4 in [45]. In Fig. 7.8, we show the pressure drop as a function of the

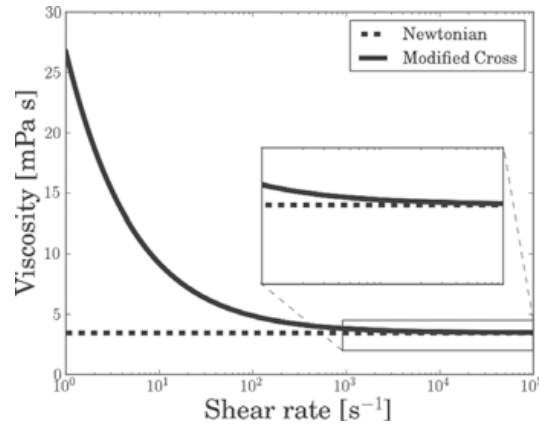


Fig. 7.5. The two viscosity models used. The Modified Cross model is given by $\frac{\mu - \mu_\infty}{\mu_0 - \mu_\infty} = \frac{1}{(1 + (l\dot{\gamma})^m)^a}$ with $l = 3.736s$, $m = 2.406$, $a = 0.254$, $\mu_0 = 0.056 Pa s$, $\mu_\infty = 0.00345 Pa s$. Note that the Modified Cross approaches the Newtonian model used as $\dot{\gamma} \rightarrow \infty$

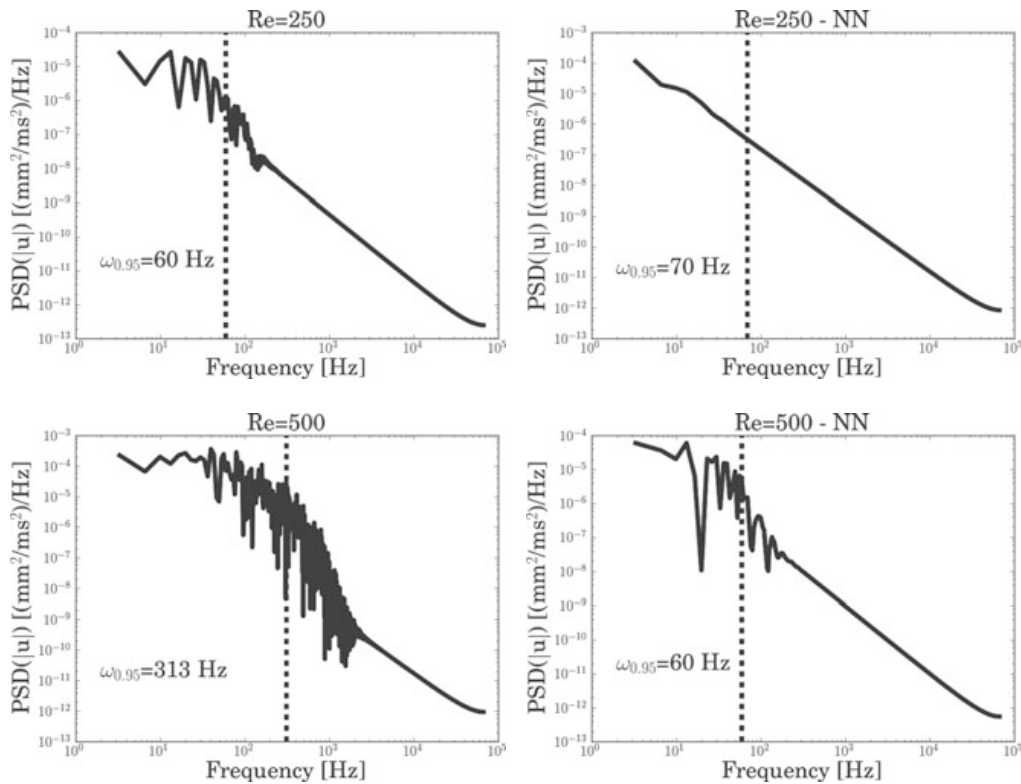


Fig. 7.6. The figure shows the $PSD_{||u||}$ Reynolds numbers 250 and 500 with a Newtonian and non-Newtonian viscosity model

Reynolds number in the parent vessel. For Reynolds number between 0 and 200, the pressure drop demonstrate a linear dependency to the Reynolds number. However, already at $Re=200$ deviations start to occur, also with notable variations over time. The transition point is, however, not as easily identified as in stationary pipe flow.

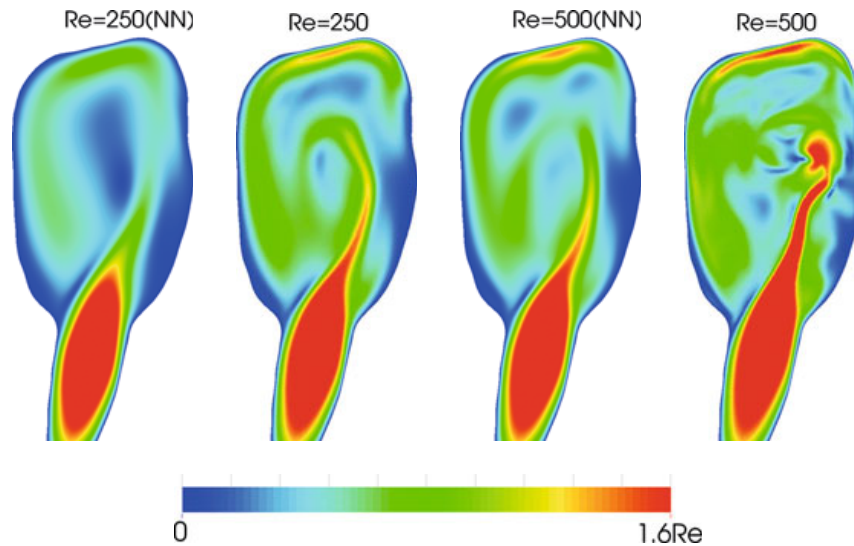


Fig. 7.7. The figure shows the velocity magnitude of the flow for simulations with a non-Newtonian viscosity compared to simulations with a Newtonian viscosity

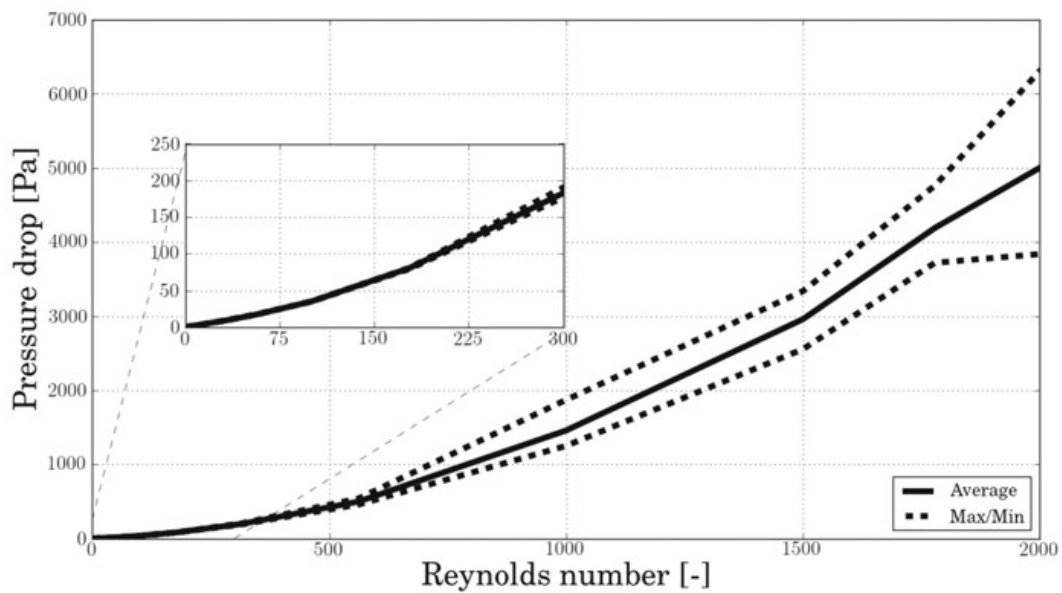


Fig. 7.8. The figure shows the pressure drop over the aneurysm as a function of the Reynolds number. Clearly, the pressure drop demonstrate a close to linear relation with respect to the Reynolds number for low numbers, but already at around Reynolds number 200 deviations from the linear relation occur and the pressure drop is no longer static in time

7.8 Discussion

This chapter mainly discuss aspects of cerebral aneurysms and aim to illustrate that transition to turbulence might be an important factor for some aneurysms. We modelled a canine aneurysm model, under steady in- and outflow conditions, and transi-

tion occurred already at Reynolds number around 200–500. It remains to be investigated whether transition is important *in vivo* and whether it is linked to rupture.

Aneurysms have strong geometrical variation. A recent publication [43] found transition in 5 of 12 middle cerebral artery aneurysms at comparable Reynolds numbers (also under stationary conditions). Some clinical research have also reported signs of transition. For instance, Ferguson found that 10 out of 17 aneurysms had bruits of sounds with predominate frequencies in the range of 270 to 660 Hz [10] and suggested that the sounds were generated by transitional or turbulent flow inside the aneurysm. Other studies such as [3, 6, 35] suggest that pulsatile tinnitus sometimes is caused by transition to turbulent flow inside aneurysms.

There are many factors that may both promote and delay transition. In addition to the geometry, both flow pulsatility, non-Newtonian rheology, and fluid–structure interaction between blood and vessels may significantly both decrease and increase the threshold for transition. Furthermore, these factors may even promote transition in some aneurysm and delay transition in others. In this paper, we have demonstrated that a non-Newtonian model (Modified Cross) delayed transition in one particular aneurysm. It is not clear whether this applies to other aneurysm or non-Newtonian models.

Many other conditions related to abnormal blood flow, such as stenosed carotid arteries, aortic aneurysms, arteriovenous malformation share the characteristics of Reynolds number significantly less than 2000, but involve flow in highly complex geometry that might significantly reduce the threshold of transition. Furthermore, audible sounds are often indicative of the severity of the conditions. It therefore seems that transitional or turbulent flow may be associated with many cardiovascular conditions and this observation suggest that an increased focus on transition in the computational modelling community might be needed.

The flow of cerebrospinal fluid flow that surrounding the central nervous system is in many respect similar to cardiovascular flow. Rough calculations of the Reynolds number suggest that it is around 200 in healthy flow, but several conditions are associated with hyper-kinetic flow. Clinicians often report turbulence in normal pressure hydrocephalus, a form of dementia. A recent publication [17] shows that the cerebrospinal fluid flow is on the threshold to transition in a patient with the Chiari malformation – a condition where the lower part of the brain is herniated through the skull and obstruct the pulsatile flow between the neck and skull. Hence, transition may also be an issue for conditions associated with abnormal cerebrospinal fluid flow.

Detecting transitional or turbulent flow by performing numerical simulations are challenging because the mechanism behind transition is only partly understood. Delaying or removing transition in numerical simulations are easily done by for example employing stabilizing schemes or using too coarse resolution. However, clinical evidence over a wide range of applications suggest that flow instabilities, transition and turbulence might be important in several conditions. Finally, the fluid-structure interaction between the flow and surrounding tissue and the non-linear viscosity of blood might both stabilize and de-stabilize the flow depending on the circumstances.

Hence, at this point, it seems that there are many open questions and unresolved issues concerning transitional flow in several important diseases.

7.9 Conclusions

Some evidence in the clinical literature suggests that conditions such as for example cerebral aneurysms may sometimes cause transition to turbulence. Still, this issue has largely been neglected in the biomechanical modelling and numerical simulations. The current chapter presents simulations that demonstrate that transition may occur already at Reynolds number of the order of 300–500 in a typical canine model aneurysm. Aneurysm geometry, flow pulsatility, non-Newtonian rheology, and fluid–structure interaction may both promote and delay transition and it is therefore unclear how important transition is *in vivo*.

References

1. Alnæs, M.S., Isaksen, J., Mardal, K.A., Romner, B., Morgan, M.K., Ingebrigtsen, T.: Computation of hemodynamics in the circle of willis. *Stroke* **38**(9), 2500–2505 (2007)
2. Antiga, L., Steinman, D.A.: Rethinking turbulence in blood. *Biorheology* **46**(2), 77–81 (2009)
3. Austin, J., Maceri, D.: Anterior communicating artery aneurysm presenting as pulsatile tinnitus. *ORL; Journal for oto-rhino-laryngology and its related specialties* **55**(1), 54–57 (1993)
4. Barakat, A.I.: Blood flow and arterial endothelial dysfunction: Mechanisms and implications. *Comptes Rendus Physique* (2013)
5. Beadles, C.F.: Aneurisms of the larger cerebral arteries. *Brain* **30**(3), 285–336 (1907)
6. Bergstrand, H., Olivecrona, H., Tönnis, W.: *Gefäßmissbildungen und Gefäßgeschwülste des Gehirns*. Georg Thieme (1936)
7. Chien, S.: Mechanotransduction and endothelial cell homeostasis: the wisdom of the cell. *American Journal of Physiology-Heart and Circulatory Physiology* **292**(3), H1209–H1224 (2007)
8. Davies, P.F., Remuzzi, A., Gordon, E.J., Dewey, C.F., Gimbrone, M.A.: Turbulent fluid shear stress induces vascular endothelial cell turnover *in vitro*. *Proceedings of the National Academy of Sciences* **83**(7), 2114–2117 (1986)
9. Evju, Ø., Valen-Sendstad, K., Mardal, K.A.: A study of wall shear stress in 12 aneurysms with respect to different viscosity models and flow conditions. *Journal of biomechanics* **46**(16), 2802–2808 (2013)
10. Ferguson, G.G.: Turbulence in human intracranial saccular aneurysms. *Journal of neurosurgery* **33**(5), 485–497 (1970)
11. Fillinger, M.F., Reinitz, E.R., Schwartz, R.A., Resetairts, D.E., Paskanik, A.M., Bruch, D., Bredenberg, C.E.: Graft geometry and venous intimal-medial hyperplasia in arteriovenous loop grafts. *Journal of Vascular Surgery* **11**(4), 556–566 (1990)
12. Fischer, P.F., Loth, F., Lee, S.E., Lee, S.W., Smith, D.S., Bassiouny, H.S.: Simulation of high-Reynolds number vascular flows. *Computer methods in applied mechanics and engineering* **196**(31), 3049–3060 (2007)

13. Fung, Y.c.: *Biomechanics: circulation*. Springer, New York (1997)
14. Goda, K.: A multistep technique with implicit difference schemes for calculating two- or three-dimensional cavity flows. *Journal of Computational Physics* **30**(1), 76–95 (1979)
15. Hafeez, F., Levine, R.L., Dulli, D.A.: Pulsatile tinnitus in cerebrovascular arterial diseases. *Journal of Stroke and Cerebrovascular Diseases* **8**(4), 217–223 (1999)
16. Gad-el Hak, M., et al.: Compliant coatings: a decade of progress. *Applied Mechanics Reviews* **49**, S147–S160 (1996)
17. Helgeland, A., Mardal, K.A., Haughton, V., Pettersson Reif, B.A.: Numerical simulations of the pulsating flow of cerebrospinal fluid flow in the cervical spinal canal of a chiari patient. *Journal of Biomechanics* (2014)
18. Hinze, J.: *Turbulence*. McGraw-Hill Book Company (1959)
19. Hoi, Y., Gao, L., Tremmel, M., Paluch, R.A., Siddiqui, A.H., Meng, H., Mocco, J.: In vivo assessment of rapid cerebrovascular morphological adaptation following acute blood flow increase. *Journal of neurosurgery* **109**(6), 1141 (2008)
20. Ingebrigtsen, T., Morgan, M.K., Faulder, K., Ingebrigtsen, L., Sparr, T., Schirmer, H.: Bifurcation geometry and the presence of cerebral artery aneurysms. *Journal of neurosurgery* **101**(1), 108–113 (2004)
21. Jiang, J., Johnson, K., Valen-Sendstad, K., Mardal, K.A., Wieben, O., Strother, C.: Flow characteristics in a canine aneurysm model: A comparison of 4D accelerated phase-contrast MR measurements and computational fluid dynamics simulations. *Medical Physics* **38**, 6300 (2011)
22. Kramer, M.O.: Boundary layer stabilization by distributed damping. *Journal of the American Society for Naval Engineers* **72**(1), 25–34 (1960)
23. Ku, D.N.: Blood flow in arteries. *Annual Review of Fluid Mechanics* **29**(1), 399–434 (1997)
24. Lee, S.E., Lee, S.W., Fischer, P.F., Bassiouny, H.S., Loth, F.: Direct numerical simulation of transitional flow in a stenosed carotid bifurcation. *Journal of biomechanics* **41**(11), 2551–2561 (2008)
25. Lee, S.W., Fischer, P., Loth, F., Royston, T., Grogan, J., Bassiouny, H.: Flow-induced vein-wall vibration in an arteriovenous graft. *Journal of fluids and structures* **20**(6), 837–852 (2005)
26. Meng, H., Swartz, D.D., Wang, Z., Hoi, Y., Kolega, J., Metaxa, E.M., Szymanski, M.P., Yamamoto, J., Sauvageau, E., Levy, E.I.: A model system for mapping vascular responses to complex hemodynamics at arterial bifurcations in vivo. *Neurosurgery* **59**(5), 1094 (2006)
27. Quarteroni, A., Formaggia, L.: Mathematical modelling and numerical simulation of the cardiovascular system. *Handbook of numerical analysis* **12**, 3–127 (2004)
28. Quarteroni, A., Tuveri, M., Veneziani, A.: Computational vascular fluid dynamics: problems, models and methods. *Computing and Visualization in Science* **2**(4), 163–197 (2000)
29. Roach, M.R., Scott, S., Ferguson, G.G.: The hemodynamic importance of the geometry of bifurcations in the circle of willis (glass model studies). *Stroke* **3**(3), 255–267 (1972)
30. Robertson, A.M., Sequeira, A., Owense, R.G.: Rheological models for blood. In: *Cardiovascular mathematics. Modeling and simulation of the circulatory system*, pp. 211–241. Springer-Verlag Italia, Milano (2009)
31. Schlichting, H., Kestin, J.: *Boundary-layer theory*, vol. 539. McGraw-Hill, New York (1968)
32. Sherman, T.F.: On connecting large vessels to small. The meaning of Murray’s law. *The Journal of general physiology* **78**(4), 431–453 (1981)

33. Simo, J., Armero, F.: Unconditional stability and long-term behavior of transient algorithms for the incompressible Navier-Stokes and Euler equations. *Computer Methods in Applied Mechanics and Engineering* **111**(1), 111–154 (1994)
34. Smith, D.S.: Experimental investigation of transition to turbulence in arteriovenous grafts. Ph.D. thesis, University of Illinois at Chicago (2008)
35. Sonmez, G., Basekim, C.C., Ozturk, E., Gungor, A., Kizilkaya, E.: Imaging of pulsatile tinnitus: a review of 74 patients. *Clinical imaging* **31**(2), 102–108 (2007)
36. Stehbens, W.: Turbulence of blood flow. *Experimental Physiology* **44**(1), 110–117 (1959)
37. Stein, P.D., Sabbah, H.N.: Measured turbulence and its effect on thrombus formation. *Circulation Research* **35**(4), 608–614 (1974)
38. Steinman, D.A.: Assumptions in modelling of large artery hemodynamics. In: *Modeling of Physiological Flows*, pp. 1–18, Springer, Milan (2012)
39. Steinman, D.A., Hoi, Y., Fahy, P., Morris, L., Walsh, M., Aristokleous, N., Anayiotos, A.S., Papaharilaou, Y., Arzani, A., Shadden, S., et al.: Variability of CFD solutions for pressure and flow in a giant aneurysm: The SBC2012 CFD challenge. *Journal of biomechanical engineering* **1**, 542 (2013)
40. Stettler, J., Hussain, A.: On transition of the pulsatile pipe flow. *Journal of Fluid Mechanics* **170**(1), 169–197 (1986)
41. Trefethen, L., Trefethen, A., Reddy, S., Driscoll, T., et al.: Hydrodynamic stability without eigenvalues. *Science* **261**(5121), 578–584 (1993)
42. Valen-Sendstad, K., Mardal, K.A., Mortensen, M., Reif, B.A.P., Langtangen, H.P.: Direct numerical simulation of transitional flow in a patient-specific intracranial aneurysm. *Journal of biomechanics* **44**(16), 2826–2832 (2011)
43. Valen-Sendstad, K., Mardal, K.A., Steinman, D.A.: High-resolution cfd detects high-frequency velocity fluctuations in bifurcation, but not sidewall, aneurysms. *Journal of Biomechanics* **46**(2), 402–407 (2013)
44. Valen-Sendstad, K., Steinman, D.: Mind the gap: Impact of computational fluid dynamics solution strategy on prediction of intracranial aneurysm hemodynamics and rupture status indicators. *American Journal of Neuroradiology* (2013). DOI 10.3174/ajnr.A3793
45. White, F.M.: *Fluid mechanics*. WCB/McGraw-Hill, Boston (1999)
46. Wilcox, D.C.: *Turbulence modeling for CFD*, vol. 2. DCW industries La Canada (1998)
47. Xiang, J., Tremmel, M., Kolega, J., Levy, E.I., Natarajan, S.K., Meng, H.: Newtonian viscosity model could overestimate wall shear stress in intracranial aneurysm domes and underestimate rupture risk. *Journal of NeuroInterventional Surgery* **4**(5), 351–357 (2012)
48. Zamir, M.: Nonsymmetrical bifurcations in arterial branching. *The Journal of general physiology* **72**(6), 837–845 (1978)

Paper II

Robustness of common hemodynamic
indicators with respect to numerical
resolution in 38 middle cerebral artery
aneurysms

*Øyvind Evju, Jose M. Pozo, Alejandro F. Frangi
and Kent-Andre Mardal.
Submitted.*

Robustness of common hemodynamic indicators with respect to numerical resolution in 38 middle cerebral artery aneurysms

Øyvind Evju¹, Jose M. Pozo², Alejandro F. Frangi², Kent-Andre Mardal^{1,3*}

¹Center for Biomedical Computing, Simula Research Laboratory, Oslo, Norway

²Centre for Computational Imaging & Simulation Technologies in Biomedicine (CISTIB), Department of Electronic and Electrical Engineering, University of Sheffield, Sheffield, United Kingdom

³Department of Mathematics, University of Oslo, Oslo, Norway

* Corresponding author: kent-and@math.uio.no (KAM)

Abstract

Background Using computational fluid dynamics (CFD) to compute the hemodynamics in cerebral aneurysms has received much attention in the last decade. The usability of these methods depends on the quality of the computations, highlighted in recent discussions. The purpose of this study is to investigate the convergence of common hemodynamic indicators with respect to numerical resolution.

Methods 38 middle cerebral artery bifurcation aneurysms were studied at two different resolutions (one comparable to most studies, and one finer). Relevant hemodynamic indicators were collected from two of the most cited studies, and were compared at the two refinements. In addition, correlation to rupture was investigated.

Results Most of the hemodynamic indicators were very well resolved at the coarser resolutions, correlating with the finest resolution with a correlation coefficient >0.95 . The oscillatory shear index (OSI) had the lowest correlation coefficient of 0.83. A logarithmic Bland-Altman plot revealed noticeable variations in the proportion of the aneurysm under low shear, as well as in spatial and temporal gradients not captured by the correlation alone.

Conclusion Statistically, hemodynamic indicators agree well across the different resolutions studied here. However, there are clear outliers visible in several of the hemodynamic indicators, which suggests that special care should be taken when considering individual assessment.

Introduction

Unruptured aneurysms constitute a major dilemma for clinicians because of the high prevalence of about 2%, the low annual rupture risk of less than 1%, combined with a high mortality of around 40% associated with rupture [1,2]. For this reason, improved risk assessment is sought to improve treatment and reduce costs. To this end, several indicators representing aneurysm morphology [3–8] and hemodynamics [9–14] have been proposed as biomarkers for aneurysm rupture.

The *in vivo* measurement of detailed blood flow in intracranial aneurysms is currently infeasible, since the existing methods are invasive and/or too limited in resolution. Because of this, computational fluid dynamics (CFD) have been used to estimate the blood flow in aneurysms and adjacent vessels. However, methods, resolutions, models and hemodynamic indicators vary among studies and confound clinicians [15]. For instance, the ASME 2012 Challenge [16] displayed significant variations among results obtained from different research groups despite given common geometry and boundary conditions. Furthermore, deviation from laminar flow has been observed [17,18]. These studies have spurred significant activity on qualitative assessment of the effect of numerical schemes, software packages and resolution [19–22]. Our motivation with the current study is to address whether resolution plays an important role in quantitative studies.

In the numerous CFD studies on cerebral aneurysms available, a wide range of hemodynamic indicators have been proposed. Most are based on the wall shear stress (WSS), that is, the friction acting on the vessel wall, which may vary considerably both with respect to location, phase in the cardiac cycle, and among patients. Some indicators like maximal or average WSS are motivated by the assumption that the vessels are only able to sustain a certain amount of friction. Others, like oscillatory shear index (OSI), low shear area (LSA), WSS gradients (WSSG), and shear concentration index (SCI) are more directly motivated by the mechanotransduction in the vessel walls. Other indicators attempt to quantify the dissipation or jets in the flow like the viscous dissipation ratio (VDR) and inflow concentration index (ICI). The convergence or sensitivity with respect to resolution, methods and models may vary among these indicators. In [19], the authors highlight the missing or inadequate convergence tests in computational studies. The cause of this is suggested to be the computational time required, but they also point to choice of numerical scheme, with schemes tailored for laminar flow might never capture transitional or turbulent flow patterns. Furthermore, the relationship between the different indicators has been highlighted for being insufficiently discussed [15].

In this study, we have investigated the robustness of common hemodynamic indicators with respect to numerical resolution. We have chosen indicators from two of the most frequently cited studies in the field, namely Cebal et al. [10] and Xiang et al. [14]. From these studies, all hemodynamic indicators significantly correlated with rupture ($p < 0.05$), were computed. In addition, we computed the wall shear stress gradient (WSSG) and the wall shear stress time derivative (TDWSS) for completeness, in order to capture spatial and temporal variations. We computed all indicators at different refinement levels to investigate the effects of numerical resolution. Finally, we also included the morphological indicators aspect ratio (AR), non-sphericity index (NSI) and volume (V). Correlations among morphological indicators, hemodynamic indicators, and rupture status were investigated to uncover potential surrogates. To limit the amount of variability in the data selection, we limited our study to middle cerebral artery (MCA) bifurcation aneurysms. A total of 38 geometries were studied.

Methods

3D Rotational Angiography (3DRA) images from 53 patients including a MCA bifurcation aneurysm were selected from the @neurIST [23,24] database. The cerebral vasculature in the region of interest was automatically segmented by a geodesic active region segmentation method [25]. The possible geometrical and topological errors in the resulting vessel surface were manually corrected using the suite @neuFuse [24]. The vasculature of interest was isolated cutting with planes perpendicular to the centerline, and the neck was manually delineated as the surface separating the aneurysm dome from the parent vessels, instead of a single plane [7].

A selection of the suitable geometries was made based on the sufficient length of the vessels present on the segmentation. Geometries where the segmentation did not reach further upstream than the C3 segment of the internal carotid artery (ICA) were excluded from further analysis. This was done to include possible secondary flows initiated around the carotid siphon that propagates downstream, as noted in [26]. In the cases where we had multiple segmentations, the geometry with the longest centerline was selected. A total of 38 geometries were included for further studies, and shown in Figure S1 in the supporting information. A brief summary of the selected dataset is found in Table 1.

Table 1. Summary of the selected dataset.

Parameter	Data range
<i>Ruptured/unruptured</i>	13/25
<i>Age [years]</i>	35-78 ($\mu=52.8$, $\sigma=9.2$)
<i>Female/male [-]</i>	28/10
<i>Flow rate (ICA) [ml/min]</i>	100-382 ($\mu=245$, $\sigma=62$)
<i>Flow rate (MCA) [ml/min]</i>	58-255 ($\mu=134$, $\sigma=38$)

The hemodynamic indicators computed include the ones significantly correlated with aneurysm rupture in either Xiang et al. [14] or Cebal et al. [10]. In addition, the wall shear stress gradient and a wall shear stress time derivative functional are computed for completeness. The exact definitions and significance of each of the indicators computed, are shown in Table 2A-B.

For completeness, we have also included in the study the two morphological indicators most frequently considered [6,7,14] for their high correlation with aneurysm rupture: aspect ratio (AR) [27] and non-sphericity index (NSI) [4]. Their definition is presented in Table 2C, and they were automatically computed from the segmented aneurysm surface and the delineated neck. We have also included the aneurysm volume as size indicator.

Table 2. Definition of all indicators computed. For notation see Supporting information.

Indicator	Abbrev.	Study	Significance	Definition used
Time- and space-averaged WSS	AWSS	Xiang et al. [14]	R<U ($p<0.0001$)	$\frac{1}{A_a} \int_{\Gamma_a} \bar{\tau} dS$
Maximum WSS	MWSS	Xiang et al. [14] Cebal et al. [10]	R<U ($p=0.0002$) R>U ($p<0.004$)	$\max_{x \in \Gamma_a} \bar{\tau} $
Oscillatory shear index	OSI	Xiang et al. [14]	R>U ($p<0.0001$)	$\frac{1}{A_a} \int_{\Gamma_a} \frac{1}{2} \left(1 - \frac{ \bar{\tau} }{ \bar{\tau} } \right) dS$
Low shear area	LSA	Xiang et al. [14]	R>U ($p<0.0001$)	$\frac{1}{A_a} \int_{\Gamma_a} \begin{cases} 1, & \text{if } \bar{\tau} < 0.1AWSS \\ 0, & \text{otherwise} \end{cases} dS$
Viscous dissipation ratio	VDR	Cebal et al. [10]	R<U ($p<0.0174$)	$\frac{1}{T1 - T0} \int_{T0}^{T1} \frac{\frac{1}{V_a} \int_{\Omega_a} 2\frac{\mu}{\rho} \epsilon ^2 dv}{\frac{1}{V_{nv}} \int_{\Omega_{nv}} 2\frac{\mu}{\rho} \epsilon ^2 dv} dt$
Inflow concentration index	ICI	Cebal et al. [10]	R>U ($p<0.004$)	$\frac{1}{T1 - T0} \int_{T0}^{T1} \frac{Q_{in}/Q_{pa}}{A_{in}/A_{neck}} dt$
Shear concentration index	SCI	Cebal et al. [10]	R>U ($p<0.049$)	$\frac{1}{T1 - T0} \int_{T0}^{T1} \frac{F_h/F_a}{A_h/A_a} dt$

(A) Overview of hemodynamic indicators taken from literature (R=ruptured, U=unruptured).

Indicator	Abbrev.	Definition used
Time-derivative WSS	TDWSS	$\frac{1}{A_a} \int_{\Gamma_a} \left \frac{\partial \bar{\tau} }{\partial t} \right dS$
WSS gradient	WSSG	$\frac{1}{A_a} \int_{\Gamma_a} \ \nabla \bar{\tau}\ dS$

(B) Hemodynamic indicators added for completion.

Indicator	Abbrev.	Definition used
Non-sphericity index	NSI	$1 - \frac{(18\pi)^{1/3} V_a^{2/3}}{A_a}$
Aspect ratio	AR	$\frac{\text{Aneurysm depth}}{\text{Neck width}}$

(C) Morphological indicators computed.

Tetrahedral meshes were generated using VMTK (www.vmtk.org). We generated two sets of meshes to investigate the robustness of the computed indicators with respect to numerical resolution. We varied the resolution depending proximity to the aneurysm domain, increasing the target nodal distance up to a factor 2 furthest from the aneurysm domain. The parent artery had a target nodal distance of 1.25 times the intra-aneurysmal target nodal distance. For small arteries, we reverted to a radius-adaptive sizing method. All meshes included a boundary layer of approximately 0.3 times the target nodal distance. This boundary layer consisted of 4 sublayers, gradually decreasing in thickness by a factor 0.6, resulting in the outermost sublayer to be of an approximate thickness of 0.03 times the target nodal distance.

The coarse meshes consisted of 0.5-1.5 million cells, with an average nodal distance of 0.18mm close to the aneurysm domain, increasing to the double further from the aneurysm. The finer meshes used, had an average

nodal distance of 0.13mm in the near-aneurysm domain. The velocity is approximated using piecewise quadratic polynomials, making the effective mesh resolution 0.065mm. The meshes varied in size from 1.2 to 4.0 million cells. This corresponds to approximately 10-32 million linear elements. Compared to Valen-Sendstad and Steinman [19], our fine spatial resolution is similar to their high resolution (0.065mm to 0.06m). The coarse meshes are approximately 50% coarser than their normal resolution (0.18mm to 0.12mm). A comparison of the two refinements are visualized in Figure 1.

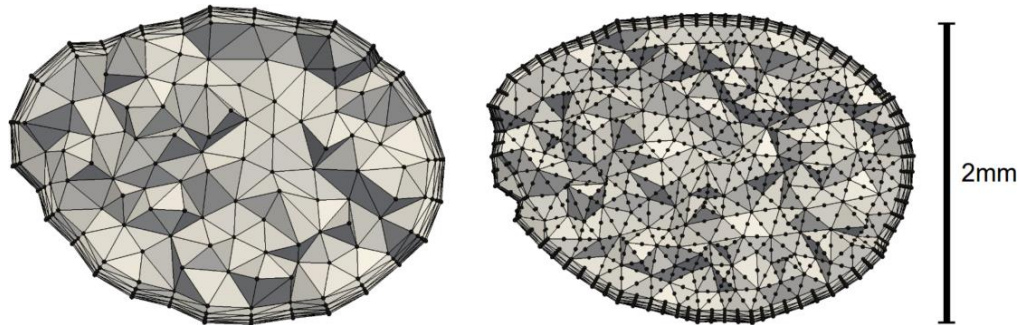


Figure 1: The figure illustrates the differences between the coarsest resolution on the left, and the finest resolution on the right. The clip is done just upstream from the aneurysm of model 1. The black dots represent points at which the velocity is computed.

By selecting 8000 time steps for the coarse mesh, and 23000 time steps for the fine mesh, we assured the same Courant number for both refinements, which is below 1 for flow velocities up to 1.5 m/s.

All hemodynamic indicators were computed on both sets of refinements, and compared with correlation coefficients, average differences and a Bland-Altman plot [28]. A more comprehensive test was performed on the five first aneurysms of the dataset, where all results were computed on 4 different resolutions. The 2 additional meshes had a resolution between the coarse and the fine meshes. For all resolutions, the velocity was approximated with piecewise quadratic polynomials, and the indicators were computed from the second cycle.

We assume blood to behave as a Newtonian fluid with a dynamic viscosity (μ) of 3.45 mPa s, as justified by Evju et al. [29], and with a density of 1.056 g/mm³ (ρ). The walls were assumed to be rigid and impermeable. The inflow boundary conditions were set on the C2/C3 segment as a Womersley profile [30] scaled with the cross-sectional area, as suggested in [31]. The inflow velocity was adjusted to match a physiologically realistic flow rate of 245 ml/min (± 61 ml/min) [32]. We matched this with an average inflow velocity of 0.27 m/s, resulting in a standard deviation of 62 ml/min.

An average profile is obtained from elderly adults in Hoi et al. [32], measured using cine phase contrast magnetic resonance imaging (PC-MRI) at the C1 segment, with a period of 0.949 seconds (63 bpm). Since we

are mainly interested in the flow in the MCA, we reduced the pulsatility by 15% to account for a dampening along the carotid siphon. The dampening has been reported to be in the range -5% to 52% with mean 17.4%. [33] The final dampened flow rate profile is visualized in Figure 2, normalized with 0.27 m/s times cross-sectional area.

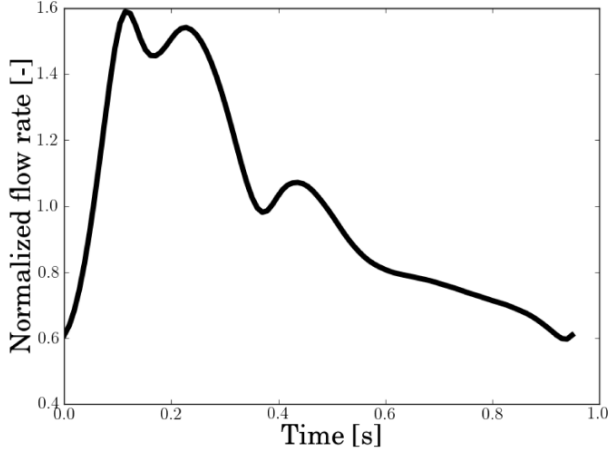


Figure 2: Flow profile used in the simulations.

On the other arteries included we used pressure conditions to approximately distribute the flow by the principle of minimum work (Murray's law) [34]. More specific, the pressure at artery i is set to

$$p_i = K \left(\frac{r_i^3}{\sum_j r_j^3} \right)^{-1} \int_{\Gamma_i} \mathbf{u} \cdot \mathbf{n} dS$$

where r_i denotes the radius of artery i , Γ_i is the cross-sectional surface, and \mathbf{n} the outward pointing normal. The summation is over all arteries except ICA, and the constant K is set to $10^9 \frac{kg}{m^4 s}$. This outlet condition ensures that the length of the outlets has a minimal effect on the flow division, matching Murray's law at the M2 outlets with an average deviation of -3.2% ($\pm 3.2\%$). These pressure conditions are preferred over velocity outflow conditions, because of the lesser influence on the upstream flow.

The incompressible Navier-Stokes equations were solved using the open source software cbcflow [35] based on FEniCS [36]. The computation of the hemodynamic indicators were done using cbcpost [37]. The solver implementation mimics very closely the one described in [38], and displays second order convergence in both time and space. It is based on an operator splitting scheme, with a linearization of the convective term that keeps the second order convergence in time. At each time step, a tentative velocity is computed using the pressure field from the previous time step. This is then followed by applying the incompressibility constraint to compute a corrected pressure. Finally, the tentative velocity and corrected pressure is used to compute the final velocity.

To determine the correlation with rupture status, we first grouped the results into groups of ruptured and unruptured. We then performed a Shapiro-Wilks test for the normality of the results. Where the null

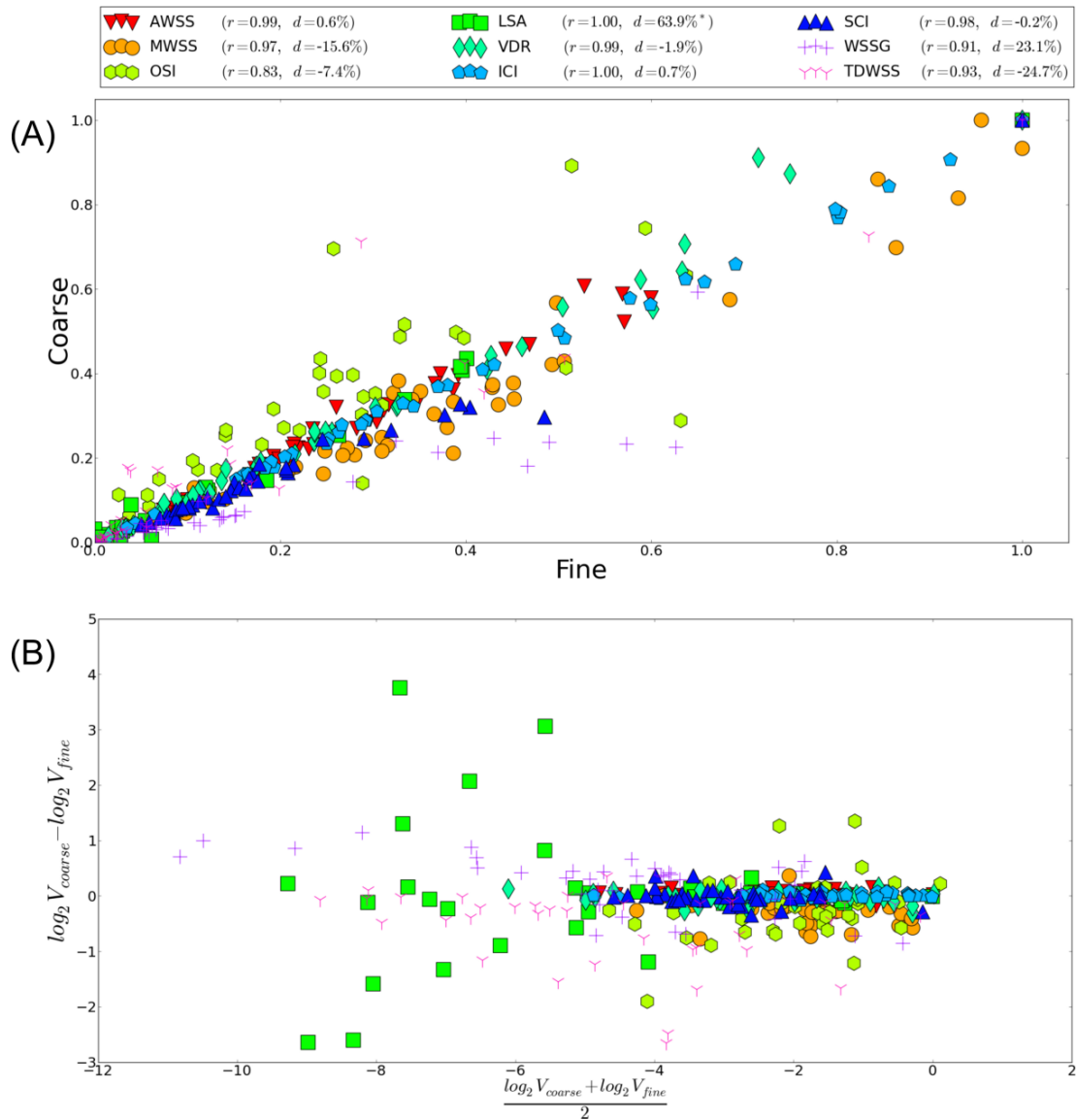


Figure 3: Comparison between the two refinements for all hemodynamic indicators. (A) Correlation plot between coarse and fine refinements. (B) Logarithmic Bland-Altman plot of coarse versus fine (V_{coarse} vs V_{fine}). r denotes the Pearson correlation coefficient, d the average difference ($d = \frac{1}{38} \sum_{i=1}^{38} \frac{V_{coarse}^i - V_{fine}^i}{V_{fine}^i}$). All values are normalized with the max value at the finest refinement. *: In 5 cases, LSA was zero for at least one of the two refinements (and less than 0.03 on the other). These are excluded from the Bland-Altman plot and the computation of d , to avoid division-by-zero.

hypothesis of normally distributed data could not be rejected we used a two-tailed t-test. Otherwise, we used a Mann-Whitney U-test.

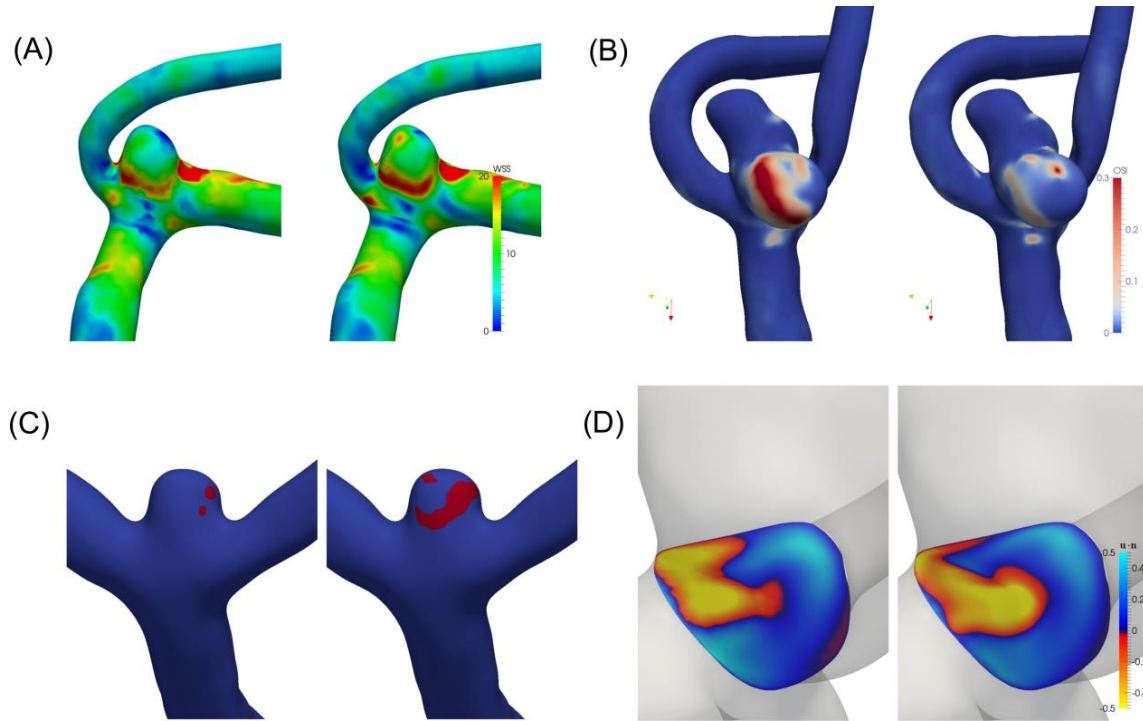


Figure 4: Variability in selected indicators, representative of worst case. Left figures represent the coarse resolution, right figures represent the fine. (A) Shows the WSS fields at different refinements of case 21. (Coarse/fine: AWSS=9.7/8.9 Pa, MWSS=43.7/51.8 Pa.) (B) OSI fields at different refinements for case 48 (coarse: 0.028, fine: 0.012). (C) LSA fields ($|\tau| < 0.1$ in red) at different refinements of case 9 (coarse: 0.033, fine: 0.076). (D) ICI fields at different refinements for case 24 at $t=0.2$ (coarse: 1.20, fine: 1.14).

Results

Figure 3A shows the correlation between the two sets of simulations performed on different refinements. We see that most of the indicators are very well reproduced on the coarsest resolutions, with a few exceptions. That is, AWSS, MWSS, LSA, VDR, ICI, SCI correlate very strongly ($r > 0.95$). The OSI appears to be the most difficult quantity to correctly rank, with a correlation coefficient of 0.834, which is largely caused by a few outliers. Also WSSG ($r = 0.910$) and TDWSS ($r = 0.932$) have a number of outliers. We remark that although MWSS demonstrated very strong correlation it is generally underestimated on the coarser refinement with an average deviation of 15.6%.

The logarithmic Bland-Altman plot in Figure 3B illustrates the spread of in particular WSSG, TDWSS and LSA. The variations from lowest to highest of around 2^{10} demonstrate that correlation alone is not a sufficient criterion for robustness. From the plot, we see that LSA in particular is difficult to accurately compute for lower values.

Regarding convergence, the global L^2 -norm of the velocity varied by less than 1.2% of time-averaged velocity between the coarse and fine resolution for all aneurysms. The more thorough convergence test on the first five geometries, revealed a difference in the same norm of less than 0.13% between the two finest refinement

levels. However, at the two finest refinement levels, the AWSS, VDR, ICI and SCI varied up to 5%. The MWSS, OSI and LSA all showed differences of up to 12%, whereas the WSSG and TDWSS showed differences of up to 40% between the two finest refinements.

Figure 4 shows a visual representation of worst case scenarios of selected indicators. Figure 4A shows the WSS at coarse and fine resolution in case 21 which is representative for the maximal difference in MWSS and AWSS. Clearly most of the main features are present in the coarse resolutions but there are spots (e.g. at the top) with clear differences. In this case, AWSS was 9.7 Pa and 8.9 Pa and MWSS 43.7 Pa and 51.8 Pa at the coarse and fine resolutions, respectively. Figure 4B shows the differences in OSI fields at coarse and fine resolution in case 48. Clearly, the coarse resolution overestimates the area of local OSI above 0.1 which results in an OSI of 0.028 at the coarse resolution and only 0.012 at the fine resolution. Figure 4C shows the LSA field in case 9, where the coarse resolution clearly underestimates the LSA. This is reflected in the values 0.033 at coarse resolution and 0.076 on the fine resolution. Finally, the ICI field for case 24 is shown in Figure 4D at $t=0.2$ where only slight variations between the coarse and fine resolution can be seen. The resulting ICI is 1.20 and 1.14, respectively.

By investigating the correlation between the different indicators shown in Table 3 and Table 4, we found that they were to a large degree uncorrelated, with a few exceptions. For the hemodynamic indicators, the strongest correlations are between the SCI and LSA ($r=0.86$). VDR correlates with AWSS at $r=0.77$. WSSG correlates with MWSS with $r=0.70$. For all other hemodynamic indicators, the correlations are medium to none ($|r|<0.6$). Between hemodynamic and morphological indicators, we found a correlation between ICI and volume at $r=0.62$. We also found a correlation between LSA and AR at $r=0.64$. All other correlations were below 0.6 in absolute value.

Table 3. Correlation matrix between hemodynamic indicators. All coefficients larger than 0.6 are highlighted in bold.

	AWSS	MWSS	OSI	LSA	VDR	ICI	SCI	WSSG	TDWSS
AWSS	1.00								
MWSS	0.30	1.00							
OSI	-0.10	-0.17	1.00						
LSA	-0.46	0.19	0.02	1.00					
VDR	0.77	-0.07	0.07	-0.41	1.00				
ICI	-0.24	-0.33	0.41	-0.08	-0.09	1.00			
SCI	-0.49	0.31	-0.07	0.86	-0.51	-0.01	1.00		
WSSG	0.57	0.70	0.00	-0.16	0.23	-0.33	-0.12	1.00	
TDWSS	0.53	0.31	0.49	-0.26	0.35	0.17	-0.26	0.63	1.00

Table 4. Correlation between all hemodynamic and morphological indicators. All coefficients larger than 0.6 in absolute value are highlighted in bold.

	AR	NSI	Volume
AWSS	-0.46	-0.42	-0.55
MWSS	0.29	0.22	-0.19
OSI	0.00	0.02	0.07
LSA	0.64	0.43	0.45
VDR	-0.51	-0.51	-0.49
ICI	0.20	0.35	0.62
SCI	0.62	0.41	0.51
WSSG	-0.15	-0.18	-0.33
TDWSS	-0.21	-0.11	-0.22

Concerning rupture status, summarized in Table 5, we see that all the morphological indicators computed are able to discriminate between the two groups at a statistically significant level. Of these, NSI were the most significant, with higher values in the ruptured group (0.18 to 0.12; $p=0.007$). AR was also higher in the ruptured group than in the unruptured group (1.25 to 0.97; $p=0.016$). The ruptured aneurysms were also larger, demonstrated with a greater volume (123 to 88mm³; $p=0.019$). Of the hemodynamic indicators computed, only ICI showed a significant difference between the two groups, with higher values in the ruptured aneurysms (1.64 to 1.29; $p=0.044$). MWSS also showed a tendency of higher values in the ruptured group, however not at a significant level (65.2 to 57.2; $p=0.068$). The other hemodynamic indicators were not statistically significant, with p -values ranging from 0.131 to 0.896. We remark that large changes between both mesh resolutions were observed in the p -value of OSI (from 0.244 to 0.896) and MWSS (from 0.112 to 0.068). However, none of the indicators changed from not-significant to significant or vice versa with respect to resolution.

Discussion

In this study we investigated the computational robustness of hemodynamic indicators based on two of the most frequently cited quantitative studies in the field [10,14], on a dataset consisting of 25 unruptured and 13 ruptured MCA aneurysms. In addition, we included three common morphological indicators, as well as two hemodynamic indicators for completeness. Coarse and fine resolution simulations correlated very strongly ($r>0.95$) for AWSS, MWSS, LSA, VDR, ICI, SCI, while OSI ($r=0.83$), WSSG ($r=0.91$), and TDWSS ($r=0.93$) correlated strongly. Although strongly correlated, the important deviations from the identity line observed for LSA ($d=63.9\%$), TDWSS ($d=-24.7\%$) and WSSG ($d=23.1\%$) indicates over- or underestimation in the coarser resolution with respect the finer resolution. The inspection of the corresponding logarithmic Bland-Altman plot revealed large variations for the lower values, in particular for LSA.

Our coarse resolution in this study is representative of a normal or high resolution in common CFD analysis of aneurysms. Considering the global L^2 -norm of the velocity, we found only very small changes ($<1.2\%$) between this resolution and our finest resolution. However, even at the finest refinement levels, a detailed convergence analysis of the indicators on five aneurysms showed that not all indicators were converged in the strict sense usually applied to CFD analysis. Only the indicators AWSS, VDR, ICI, and SCI showed a differences of less than

5% between the two finest refinements. MWSS, OSI and LSA showed differences of up to 12%, while WSSG and TDWSS had a difference of up to 40%.

Table 5. Comparison between the ruptured and unruptured aneurysms for all indicators at both resolutions.

Indicator	Units	Resolution	Ruptured		Unruptured		p-value
			Mean	Std. dev.	Mean	Std. dev.	
AWSS	Pa	fine	6.8	6.3	7.3	3.9	0.131
		coarse	7.0	6.5	7.2	3.9	0.190
MWSS	Pa	fine	65.2	32.7	57.2	44.1	0.068
		coarse	51.8	24.8	46.3	30.8	0.112
OSI	-	fine	0.028	0.018	0.029	0.020	0.896
		coarse	0.026	0.014	0.027	0.023	0.244
LSA	-	fine	0.130	0.238	0.069	0.114	0.151
		coarse	0.131	0.234	0.066	0.109	0.144
VDR	-	fine	0.49	0.51	0.63	0.52	0.182
		coarse	0.50	0.53	0.60	0.47	0.190
ICI	-	fine	1.64	0.73	1.29	0.98	0.044
		coarse	1.66	0.74	1.30	0.98	0.041
SCI	-	fine	6.9	8.2	4.5	2.7	0.295
		coarse	6.4	6.7	4.6	2.9	0.306
WSSG	Pa/mm	fine	1012	1202	2138	3368	0.137
		coarse	1154	1516	1861	2093	0.124
TDWSS	Pa/s	fine	407	729	400	541	0.235
		coarse	315	577	260	401	0.244
AR	-	-	1.25	0.43	0.97	0.41	0.016
NSI	-	-	0.18	0.05	0.12	0.07	0.007
Volume	mm ³	-	123	95	88	143	0.019

Correlation between indicators were weak to none, with the exception of SCI-LSA ($r=0.86$), VDR-AWSS ($r=0.77$), WSSG-MWSS ($r=0.70$), and TDWSS-WSSG ($r=0.63$). Correlation between morphological and hemodynamic indicators were weak to none except for LSA-AR ($r=0.64$), SCI-AR ($r=0.62$), and ICI-Volume ($r=0.62$). This suggests that there could be possibilities for surrogates that are more robust, for example the SCI as a surrogate for the less robust LSA.

Only one of the hemodynamic indicators, the ICI, showed a significant difference between ruptured and unruptured aneurysms. The morphological indicators all showed significant differences between the two groups, with NSI as the strongest of the three indicators included. For the other hemodynamic indicators, the tendencies were as expected with basis in the studies they were taken from, but not strong enough to reach statistical significance. The OSI was however an exception from this, where the means were practically identical, and the p-value as high as 0.896. For MWSS, the tendency was towards *higher* MWSS in ruptured aneurysms than unruptured aneurysms, but with a p-value of 0.068, this was not deemed significant. The

increased resolution did not change the p-value from significant to not-significant or vice versa for any of the indicators. This suggests that coarse simulations can provide useful information, even though the actual values are not strictly converged.

A limitation of this study is the relatively small number of 38 geometries. This might explain why statistical significance was not obtained in our study, in contrast to the same indicators studied in Cebal et al. [10] and Xiang et al. [14]. We have also only studied MCA bifurcation aneurysms, which may have different mechanisms related to rupture than aneurysms at other locations. In addition, this study, as comparable studies, is done retrospectively. This further complicates the usage of these indicators as predictors of aneurysm rupture. In particular, it has been shown that the morphology may be significantly affected by aneurysm rupture [39]. Finally, we remark that we have not assumed laminar flow in our simulations and our numerical algorithms were hence not tailored towards such application, using e.g. dissipative or stabilized schemes. The results in particular for OSI, WSSG and TDWSS might have been different if laminar flow was assumed.

The spatial resolution of the quantitative studies considered in [10] and [14] are similar to what we consider coarse resolution. Xiang et al. [14] report 300 000 to 1 000 000 tetrahedral elements, with a hexahedral boundary layer, whereas Cebal et al. [10] report a resolution of 0.1 to 0.2 mm. The temporal resolution is typically much coarser than what we have used, with time steps of 0.001s to 0.01s [19]. This is connected to the solution strategy as mentioned above, an implicit or explicit assumption of laminar flow, and the usage of diffusive schemes or stabilization terms. Other relevant studies such as [12,40–42] either lack information about resolution, or report similar resolutions. In light of the results in this study and recent studies such as [19,22], it seems reasonable to question whether these results are converged in a strict sense. However, using quantitative methods, the results of this study suggest that strict convergence does not alter conclusions based on quantitative analysis.

A detailed grid convergence of 5 aneurysms was done by Hodis et al. [43], where the authors used extrapolation to estimate the grid uncertainty of velocities and average and maximal WSS at peak systole. Our meshes are roughly comparable to their mesh refinements h_4 and h_1 . They reported grid convergence errors in average WSS of 1-11% and in maximal WSS of 6-15% for the finest mesh. This does not compare directly to our findings, but similar to this study, it highlights the difficulties of strict convergence. They state that each patient-specific model requires individual grid convergence studies. However, as our study shows, this requirement might be unnecessary strict for quantitative studies that considers tens to hundreds of aneurysm models, as the effect of outliers will be diminished.

In Khan et al. [22], the authors study resolution requirements on 3 different aneurysms. They highlight the need for a minimally dissipative solver as more important than grid or temporal resolution. In this study we use the same numerical scheme as the high fidelity solver used by the authors in that study. They state that this high fidelity solver “can tolerate surprisingly coarse resolutions”, and show that in particular AWSS and OSI are properly resolved at spatial resolutions comparable to our coarse resolutions. In our study, we find that for our 38 cases, this still holds true for AWSS, but the OSI seems more difficult to resolve for certain geometries.

Conclusion

In this study we demonstrate that a quantitative CFD analysis of hemodynamics in cerebral aneurysms, are reasonably robust even though strict convergence in a traditional sense is not obtained. This suggests that the results of the previous quantitative CFD studies such as [10,12,14,40–42], even though likely under-resolved in a strict CFD mesh convergence sense, would correlate strongly with properly resolved simulations. However, some hemodynamic indicators such as AWSS, VDR, ICI and SCI are relatively easy to resolve, compared to OSI, LSA, MWSS, WSSG and TDWSS. For individual assessment, special care should be taken that the considered hemodynamic indicators are converged, as there are outliers.

Acknowledgements

The simulations performed in this study was done on the Abel Cluster (project NN9279K), owned by the University of Oslo and the Norwegian metacenter for High Performance Computing (NOTUR), and operated by the Department for Research Computing at USIT, the University of Oslo IT-department.

<http://www.hpc.uio.no/>

Nomenclature

AR = Aspect ratio

AWSS = average WSS

CFD = Computational fluid dynamics

ICI = Inflow concentration index

MWSS = Maximal WSS

LSA = Low shear area

NSI = Non-sphericity index

OSI = Oscillatory shear index

SCI = Shear concentration index

TDWSS = Time-derivative of WSS

VDR = Viscous dissipation ratio

WSS = Wall shear stress

WSSG = WSS gradient

Supporting information

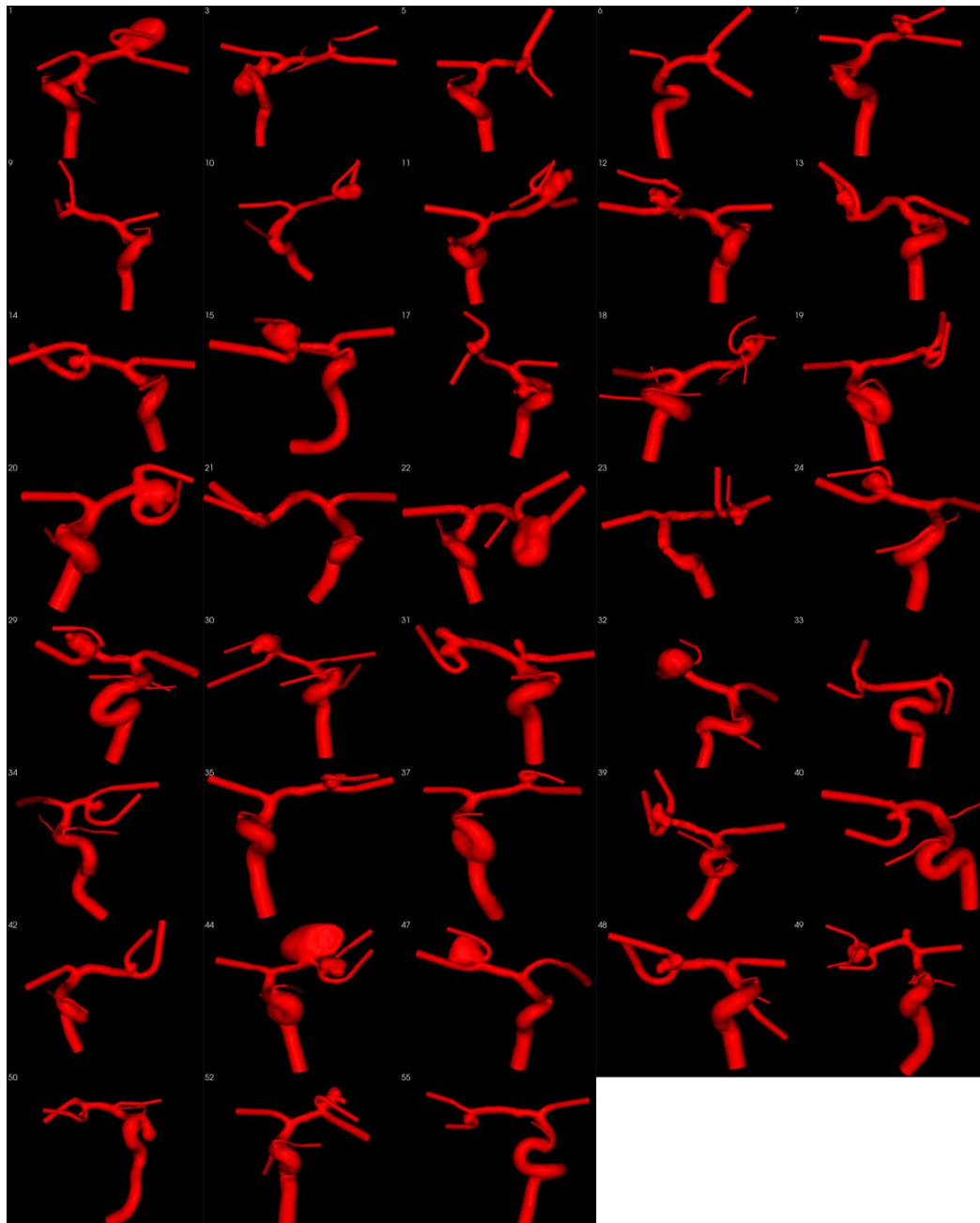


Figure S1. Geometries. All geometries used in our computations. Scale is not equal for all images.

Table S1. A short, but specific definition of the different values used to compute the hemodynamic indicators. The near-vessel domain is defined as the distance from the aneurysm neck of less than 1cm (shortest path, computed using Dijkstra's algorithm).

T_0	=	Time at start of second cycle			
T_1	=	Time at end of second cycle			
\mathbf{u}	=	Velocity field			
\mathbf{n}	=	Outward facing normal on given surface			
$\boldsymbol{\tau}$	=	$\mu[\mathbf{n} \cdot \nabla \mathbf{u} - (\mathbf{n} \cdot \nabla \mathbf{u} \cdot \mathbf{n})\mathbf{n}]$	(The wall shear stress vector)		
ϵ	=	$\frac{1}{2}(\nabla \mathbf{u} + (\nabla \mathbf{u})^T)$	Strain-rate tensor		
\bar{x}	=	$\frac{1}{T_1 - T_0} \int_{T_0}^{T_1} x dt$	(Cycle-averaged quantity)		
Ω_a	=	Aneurysm domain	Γ_a	=	Aneurysm dome surface
V_a	=	Aneurysm domain volume	A_a	=	Aneurysm dome area
Ω_{nv}	=	Near vessel domain	Γ_{nv}	=	Near vessel domain surface
V_{nv}	=	Near vessel domain volume	A_{nv}	=	Near vessel domain surface area
Γ_{neck}	=	Neck of the aneurysm	A_{neck}	=	Aneurysm neck area
Γ_{M2}	=	Outflow surface of all M2 arterial segments			
Q_{pa}	=	$\int_{\Gamma_{M2}} \mathbf{u} \cdot \mathbf{n} dS$	(Flow in parent artery)		
Γ_{in}	=	$\{\mathbf{x} \in \Gamma_{neck} \mid \mathbf{u} \cdot \mathbf{n} > 0\}$	(Inflow region of neck)		
A_{in}	=	$\int_{\Gamma_{in}} dS$	(Area of flow into aneurysm)		
Q_{in}	=	$\int_{\Gamma_{in}} \mathbf{u} \cdot \mathbf{n} dS$	(Flow into aneurysm)		
F_a	=	$\int_{\Gamma_a} \boldsymbol{\tau} dS$			
F_{nv}	=	$\int_{\Gamma_{nv}} \boldsymbol{\tau} dS$			
σ_{nv}^2	=	$\frac{1}{A_{nv}} \int_{\Gamma_{nv}} \left(\boldsymbol{\tau} - \frac{1}{A_{nv}} F_{nv} \right)^2 dS$	(Std.dev. of shear on near vessel domain)		
Γ_h	=	$\left\{ \mathbf{x} \in \Gamma_a \mid \boldsymbol{\tau} > \frac{1}{A_{nv}} F_{nv} + \sigma_{nv} \right\}$	(Region of high shear)		
A_h	=	$\int_{\Gamma_h} dS$	(Area of high shear)		
F_h	=	$\int_{\Gamma_h} \boldsymbol{\tau} dS$	(Total shear in region of high shear)		

References

1. Rinkel GJE, Djibuti M, Algra A, van Gijn J. Prevalence and Risk of Rupture of Intracranial Aneurysms: A Systematic Review. *Stroke*. 1998;29: 251–256. doi:10.1161/01.STR.29.1.251
2. Hop JW, Rinkel GJE, Algra A, van Gijn J. Case-Fatality Rates and Functional Outcome After Subarachnoid Hemorrhage: A Systematic Review. *Stroke*. 1997;28: 660–664. doi:10.1161/01.STR.28.3.660
3. Weir B, Amidei C, Kongable G, Findlay JM, Kassell NF, Kelly J, et al. The aspect ratio (dome/neck) of ruptured and unruptured aneurysms. *J Neurosurg*. 2003;99: 447–451. doi:10.3171/jns.2003.99.3.0447
4. Raghavan ML, Ma B, Harbaugh RE. Quantified aneurysm shape and rupture risk. *J Neurosurg*. 2005;102: 355–362. doi:10.3171/jns.2005.102.2.0355
5. Millán RD, Dempere-Marco L, Pozo JM, Cebal JR, Frangi AF. Morphological characterization of intracranial aneurysms using 3-D moment invariants. *IEEE Trans Med Imaging*. 2007;26: 1270–1282. doi:10.1109/TMI.2007.901008
6. Dhar S, Tremmel M, Mocco J, Kim M, Yamamoto J, Siddiqui AH, et al. Morphology parameters for intracranial aneurysm rupture risk assessment. *Neurosurgery*. 2008;63: 185–197. doi:10.1227/01.NEU.0000316847.64140.81
7. Valencia C, Villa-Uriol MC, Pozo JM, Frangi AF. Morphological descriptors as rupture indicators in middle cerebral artery aneurysms. *Engineering in Medicine and Biology Society (EMBC), 2010 Annual International Conference of the IEEE*. 2010. pp. 6046–6049. doi:10.1109/IEMBS.2010.5627610
8. Lauric A, Miller EL, Baharoglu MI, Malek AM. 3D shape analysis of intracranial aneurysms using the Writhe number as a discriminant for rupture. *Ann Biomed Eng*. 2011;39: 1457–1469. doi:10.1007/s10439-010-0241-x
9. Cebal JR, Mut F, Weir J, Putman CM. Association of hemodynamic characteristics and cerebral aneurysm rupture. *AJNR Am J Neuroradiol*. 2011;32: 264–270. doi:10.3174/ajnr.A2274
10. Cebal JR, Mut F, Weir J, Putman C. Quantitative characterization of the hemodynamic environment in ruptured and unruptured brain aneurysms. *AJNR Am J Neuroradiol*. 2011;32: 145–151. doi:10.3174/ajnr.A2419
11. Qian Y, Takao H, Umezu M, Murayama Y. Risk analysis of unruptured aneurysms using computational fluid dynamics technology: preliminary results. *AJNR Am J Neuroradiol*. 2011;32: 1948–1955. doi:10.3174/ajnr.A2655
12. Takao H, Murayama Y, Otsuka S, Qian Y, Mohamed A, Masuda S, et al. Hemodynamic differences between unruptured and ruptured intracranial aneurysms during observation. *Stroke*. 2012;43: 1436–1439. doi:10.1161/STROKEAHA.111.640995
13. Miura Y, Ishida F, Umeda Y, Tanemura H, Suzuki H, Matsushima S, et al. Low wall shear stress is independently associated with the rupture status of middle cerebral artery aneurysms. *Stroke*. 2013;44: 519–521. doi:10.1161/STROKEAHA.112.675306
14. Xiang J, Natarajan SK, Tremmel M, Ma D, Mocco J, Hopkins LN, et al. Hemodynamic-morphologic discriminants for intracranial aneurysm rupture. *Stroke*. 2011;42: 144–152. doi:10.1161/STROKEAHA.110.592923

15. Kallmes DF. Point: CFD--computational fluid dynamics or confounding factor dissemination. *AJNR Am J Neuroradiol.* 2012;33: 395–396. doi:10.3174/ajnr.A2993
16. Steinman DA, Hoi Y, Fahy P, Morris L, Walsh MT, Aristokleous N, et al. Variability of computational fluid dynamics solutions for pressure and flow in a giant aneurysm: the ASME 2012 Summer Bioengineering Conference CFD Challenge. *J Biomech Eng.* 2013;135: 021016–021016–13. doi:10.1115/1.4023382
17. Valen-Sendstad K, Mardal K-A, Mortensen M, Reif BAP, Langtangen HP. Direct numerical simulation of transitional flow in a patient-specific intracranial aneurysm. *J Biomech.* 2011;44: 2826–2832. doi:10.1016/j.jbiomech.2011.08.015
18. Valen-Sendstad K, Mardal K-A, Steinman DA. High-resolution CFD detects high-frequency velocity fluctuations in bifurcation, but not sidewall, aneurysms. *J Biomech.* 2013;46: 402–407. doi:10.1016/j.jbiomech.2012.10.042
19. Valen-Sendstad K, Steinman DA. Mind the Gap: Impact of Computational Fluid Dynamics Solution Strategy on Prediction of Intracranial Aneurysm Hemodynamics and Rupture Status Indicators. *AJNR Am J Neuroradiol.* 2013;35: 536–543. doi:10.3174/ajnr.A3793
20. Ventikos Y. Resolving the issue of resolution. *AJNR Am J Neuroradiol.* 2014;35: 544–545. doi:10.3174/ajnr.A3894
21. Jain K, Roller S, Mardal K-A. Transitional flow in intracranial aneurysms-A space and time refinement study below the Kolmogorov scales using Lattice Boltzmann Method. *Comput Fluids.* 2016;127: 36–46. doi:10.1016/j.compfluid.2015.12.011
22. Khan MO, Valen-Sendstad K, Steinman DA. Narrowing the Expertise Gap for Predicting Intracranial Aneurysm Hemodynamics: Impact of Solver Numerics versus Mesh and Time-Step Resolution. *AJNR Am J Neuroradiol.* 2015;36: 1310–1316. doi:10.3174/ajnr.A4263
23. Villa-Uriol MC, Berti G, Hose DR, Marzo A, Chiarini A, Penrose J, et al. @neurIST complex information processing toolchain for the integrated management of cerebral aneurysms. *Interface Focus.* 2011;1: 308–319. doi:10.1098/rsfs.2010.0033
24. The @neurIST Integrated Project. In: <http://www.aneurist.org>. Accessed on July 7, 2016. [Internet]. Available: <http://www.aneurist.org>
25. Bogunović H, Pozo JM, Villa-Uriol MC, Majoie C, van den Berg R, Gratama van Andel HAF, et al. Automated segmentation of cerebral vasculature with aneurysms in 3DRA and TOF-MRA using geodesic active regions: An evaluation study. *Med Phys.* 2011;38: 210–222. doi:10.1118/1.3515749
26. Valen-Sendstad K, Piccinelli M, Steinman DA. High-resolution computational fluid dynamics detects flow instabilities in the carotid siphon: Implications for aneurysm initiation and rupture? *J Biomech.* 2014;47: 3210–3216. doi:10.1016/j.jbiomech.2014.04.018
27. Ujiie H, Tachibana H, Hiramatsu O, Hazel AL, Matsumoto T, Ogasawara Y, et al. Effects of size and shape (aspect ratio) on the hemodynamics of saccular aneurysms: a possible index for surgical treatment of intracranial aneurysms. *Neurosurgery.* 1999;45: 119–129. doi:10.1097/00006123-199907000-00028
28. Bland JM, Altman DG. Measuring agreement in method comparison studies. *Stat Methods Med Res.* 1999;8: 135–160. doi:10.1191/096228099673819272
29. Evju Ø, Valen-Sendstad K, Mardal K-A. A study of wall shear stress in 12 aneurysms with respect to

- different viscosity models and flow conditions. *J Biomech.* 2013;46: 2802–2808.
doi:10.1016/j.jbiomech.2013.09.004
30. Womersley JR. Method for the calculation of velocity, rate of flow and viscous drag in arteries when the pressure gradient is known. *J Physiol.* 1955;127: 553–563. doi:10.1113/jphysiol.1955.sp005276
 31. Valen-Sendstad K, Piccinelli M, KrishnankuttyRema R, Steinman DA. Estimation of Inlet Flow Rates for Image-Based Aneurysm CFD Models: Where and How to Begin? *Ann Biomed Eng.* 2015;43: 1422–1431. doi:10.1007/s10439-015-1288-5
 32. Hoi Y, Wasserman B a, Xie YJ, Najjar SS, Ferruci L, Lakatta EG, et al. Characterization of volumetric flow rate waveforms at the carotid bifurcations of older adults. *Physiol Meas.* 2011;31: 291–302. doi:10.1088/0967-3334/31/3/002
 33. Schubert T, Santini F, Stalder a. F, Bock J, Meckel S, Bonati L, et al. Dampening of blood-flow pulsatility along the carotid siphon: Does form follow function? *AJNR Am J Neuroradiol.* 2011;32: 1107–1112. doi:10.3174/ajnr.A2426
 34. Sherman TF. On connecting large vessels to small. The meaning of Murray's law. *J Gen Physiol.* 1981;78: 431–453. doi:10.1085/jgp.78.4.431
 35. Evju Ø, Alnæs MS. cbcflow [Internet]. 2016. Available: https://bitbucket.org/simula_cbc/cbcflow
 36. Logg A, Mardal K-A, Wells G. Automated solution of differential equations by the finite element method: The FEniCS book. Springer Science & Business Media; 2012. doi:10.1007/978-3-642-23099-8
 37. Evju Ø, Alnæs MS. cbcpost [Internet]. 2016. Available: https://bitbucket.org/simula_cbc/cbcpost
 38. Mortensen M, Valen-Sendstad K. Oasis: A high-level/high-performance open source Navier–Stokes solver. *Comput Phys Commun.* 2015;188: 177–188. doi:10.1016/j.cpc.2014.10.026
 39. Schneiders JJ, Marquering H a., Van Den Berg R, VanBavel E, Velthuis B, Rinkel GJE, et al. Rupture-associated changes of cerebral aneurysm geometry: High-resolution 3D imaging before and after rupture. *AJNR Am J Neuroradiol.* 2014;35: 1358–1362. doi:10.3174/ajnr.A3866
 40. Jou L-D, Lee DH, Morsi H, Mawad ME. Wall shear stress on ruptured and unruptured intracranial aneurysms at the internal carotid artery. *AJNR Am J Neuroradiol.* 2008;29: 1761–1767. doi:10.3174/ajnr.A1180
 41. Retarekar R. Hemodynamics and natural history outcome in unruptured intracranial aneurysms [Internet]. University of Iowa. 2012. Available: <http://ir.uiowa.edu/etd/3520/>
 42. Xiang J, Yu J, Choi H, Dolan Fox JM, Snyder K V, Levy EI, et al. Rupture Resemblance Score (RRS): toward risk stratification of unruptured intracranial aneurysms using hemodynamic-morphological discriminants. *J Neurointerv Surg.* 2015;7: 490–495. doi:10.1136/neurintsurg-2014-011218
 43. Hodis S, Uthamaraj S, Smith AL, Dennis KD, Kallmes DF, Dragomir-Daescu D. Grid convergence errors in hemodynamic solution of patient-specific cerebral aneurysms. *J Biomech.* 2012;45: 2907–2913. doi:10.1016/j.jbiomech.2012.07.030

Paper III

Rupture prediction of cerebral
aneurysms: a nation-wide matched
case-control study of hemodynamics at
time of diagnosis

*Torbjørn Øygard Skodvin, Øyvind Evju, Christian
A. Helland and Jørgen Gjernes Isaksen.
Submitted.*

Rupture prediction of cerebral aneurysms: a nation-wide matched case-control study of hemodynamics at time of diagnosis.

Authors

Skodvin, Torbjørn Øygard,¹ medical student

Evju, Øyvind,² M.Sc.

Helland, Christian A,^{3,5} MD, PhD

Isaksen, Jørgen Gjernes,^{1,4} MD, PhD

Affiliations

- 1) Faculty of Health, UiT The Arctic University of Norway, Tromsø, Norway
- 2) Simula Research Laboratory, Oslo, Norway
- 3) Department of Neurosurgery, Haukeland University Hospital, Bergen, Norway
- 4) Department of Neurosurgery, University Hospital of Northern Norway, Tromsø, Norway
- 5) Department of Clinical Medicine, University of Bergen, Norway

Corresponding author

Name: Torbjørn Øygard Skodvin

E-mail address: torbjorn.skodvin@gmail.com

Telephone number: +47 99 38 70 14

Keywords: intracranial aneurysm, hemodynamics, computational fluid dynamics, subarachnoid hemorrhage, rupture

Abstract

Background and Purpose—Hemodynamic rupture predictors in cerebral aneurysms (CA) must be investigated in pre-rupture aneurysms, since rupture might significantly alter aneurysm hemodynamics. Both clinical and aneurysmal factors can confound results in unmatched patient materials. We aimed to identify hemodynamic variables at time of diagnosis associated with future rupture.

Methods—Nation-wide matched case-control study. 12 CA that later ruptured were matched 1:2 with control aneurysms that remained unruptured during a median follow-up time of 4.5 (interquartile range, 3.7-8.2) years. Cases and controls were matched by patient age and sex, and aneurysm location and size. Hemodynamic parameters were obtained from computational fluid dynamics (CFD) simulations.

Results—Low shear area (LSA) was significantly higher in cases than controls in univariate analysis ($P=0.041$). Minimal logarithmic wall shear stress (WSS), averaged logarithmic WSS, pressure loss coefficient (PLc) and inflow concentration index (ICI) showed a tendency of being associated with later rupture (P -values 0.09, 0.14, 0.15 and 0.18, respectively). LSA remained statistically significant in multivariable analysis ($P=0.030$).

Conclusions—Hemodynamics at time of diagnosis are different in aneurysms that later rupture than in those that remain unruptured. Increased LSA might be an early predictor of rupture.

Introduction

Subarachnoid hemorrhage (SAH) is an important cause of premature death and socioeconomic cost. Saccular cerebral aneurysms (CA) are the cause of 85 % of SAH.¹ CA are found in about 2-3.5 % of the adult population, but the individual rupture risk is uncertain.² Prophylactic surgical or endovascular treatment of aneurysms minimizes chances of future rupture, but involves considerable risk. Wider use and availability of radiological imaging of the brain has increased the rate of incidentally discovered CA. Evaluation of aneurysm hemodynamics can possibly aid treatment decisions.³

Aneurysm rupture itself might significantly alter aneurysm hemodynamics,⁴⁻⁶ demanding investigations with pre-rupture geometry. Reports of up to 13 cases before rupture have emerged,⁷⁻¹⁰ but none of these are matched on both clinical and aneurysmal factors, and are thus prone to confounding. For instance, aneurysm size is strongly correlated with wall shear stress (WSS),¹¹ and the combination of smoking and hypertension might increase rupture risk more than 10-fold.¹² The aim of this study was to identify hemodynamic factors at time of diagnosis of unruptured aneurysms that are associated with later rupture.

Patients and Methods

This matched case-control study is based on a retrospective data collection from 2003 to 2013, covering Norway's entire population of 5,000,000 people. For cases, we identified patients presenting with an unruptured saccular CA that later ruptured. For each case, we

selected two matching CA patients whose aneurysms did not rupture during follow-up, matched on aneurysm location and size, and patient sex and age. We retrieved clinical data and the first available cerebral angiography of each patient.

To prepare for computational simulation, an engineering team (led by Ø.E.), blinded to patients' status as case or control and to any clinical data, segmented and meshed the images into models. These segmented models were inspected by an experienced neurosurgeon (J.G.I.) to ensure consistency with the original angiography. The Appendix provides supplemental details about patient selection, recorded variables, parameter definitions and computational simulation.

For statistical analysis, we assessed variable distributions with Q-Q plots and Shapiro-Wilk tests. Balance between cases and controls was assessed using Student's t-test for parametric, Wilcoxon rank-sum test for non-parametric, and Chi squared test for categorical variables. Matched case-control analysis was performed using conditional logistic regression. Multivariable regression was performed using backwards stepwise elimination of independent variables with a threshold significance level of >0.2 . The data were analyzed with Stata for Mac (version 14; StataCorp LP, TX, USA). A *P*-value of <0.05 was assumed statistically significant.

The study was approved by the Regional Committee for Medical Research Ethics, which determined the study to be exempt from patient consent. We report according to the STROBE guidelines.

Table. Univariate Analysis of Hemodynamic Parameters in Cases and Controls

Parameter	Cases, mean (±SD) n = 12	Controls, mean (±SD) n = 24	P-values *
Minimum WSS	0.62 (0.66)	0.84 (0.69)	0.39
Time- and space-averaged WSS	6.33 (4.70)	7.50 (3.42)	0.41
Maximum WSS	39.6 (23.5)	55.2 (54.1)	0.39
Min. logarithmic WSS	-1.17 (1.39)	-0.47 (0.79)	0.09
Avg. logarithmic WSS	0.96 (1.01)	1.37 (0.53)	0.14
Oscillatory shear index	0.046 (0.039)	0.039 (0.025)	0.47
Low shear area	0.15 (0.16)	0.06 (0.07)	0.041
Pressure loss coefficient	1.25 (0.31)	1.48 (0.45)	0.15
Inflow concentration index	2.28 (1.12)	1.90 (1.17)	0.18
Shear concentration index	4.07 (2.38)	4.31 (2.44)	0.76
Viscous dissipation ratio	0.31 (0.23)	0.46 (0.63)	0.49

SD indicates standard deviation; and WSS, wall shear stress.

* P-value < 0.05 considered statistically significant.

Results

We successfully matched 12 case patients with two control patients each. The cases were four anterior communicating artery ([ACOM] 33.3%), seven middle cerebral artery ([MCA] 58.3%) and one posterior communicating artery ([PCOM] 8.3%) aneurysm. Maximal diameter was 8.34 mm (SD, 3.41) in cases and 8.15 mm (3.40) in controls ($P=0.87$). Sex, age and smoking status was similarly distributed among cases and controls (P -values 0.81, 0.80 and 0.64, respectively), while hypertension tended to be more prevalent among controls ($P=0.08$). For cases, median time from diagnosis to rupture was 3.4 years (interquartile range [IQR], 1.6-6.3). For controls, median time from diagnosis to death or end of follow-up was

4.5 years (IQR, 3.7-8.2). The Appendix provides details about the case matching, and Appendix Table II provides baseline characteristics of cases and matched controls.

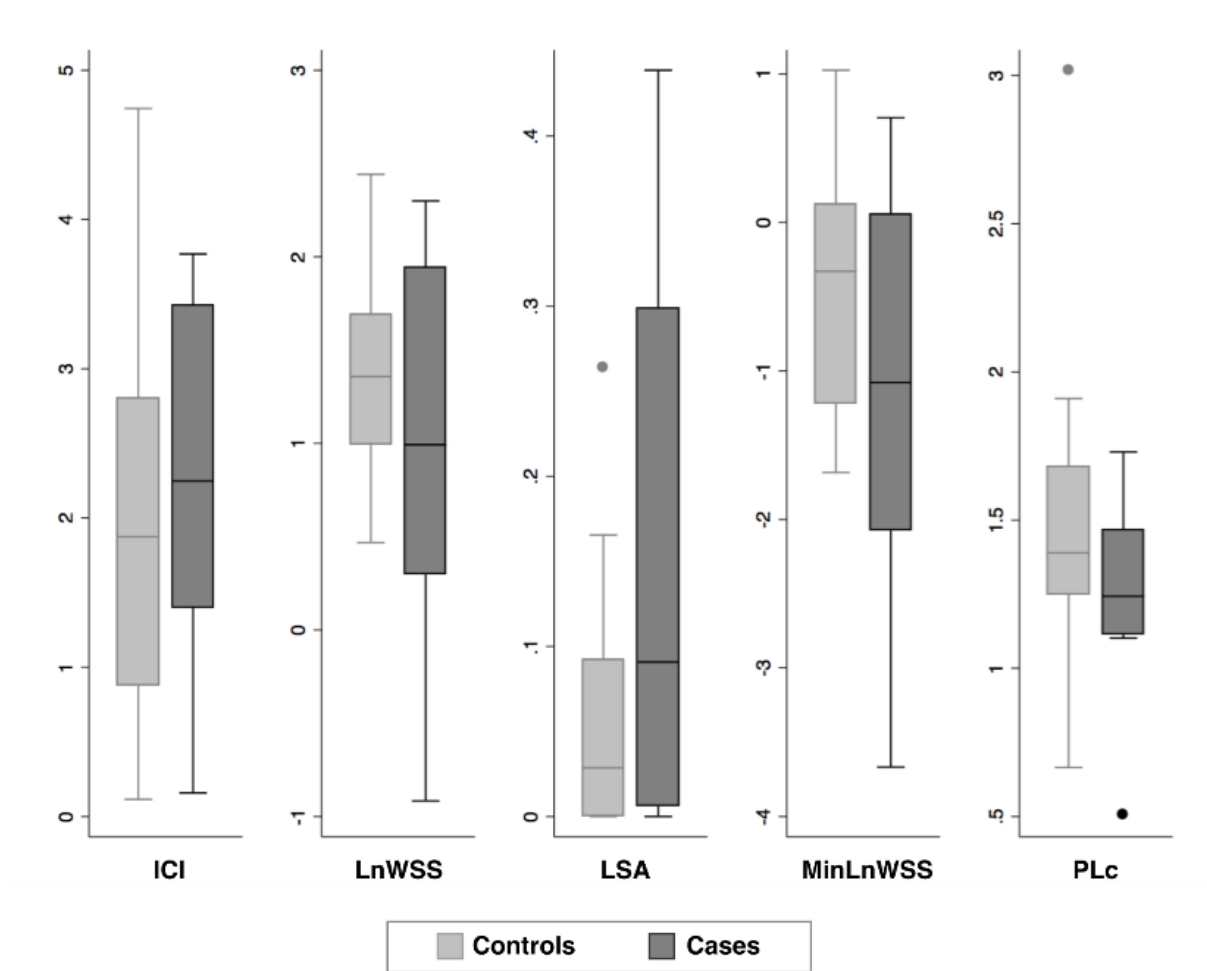


Figure 1. Graphical representation of the distribution of selected hemodynamic parameters in cases and controls. ICI indicates inflow concentration index; LnWSS, averaged logarithmic wall shear stress; LSA, low shear area; MinLnWSS, minimal logarithmic wall shear stress; PLc, pressure loss coefficient.

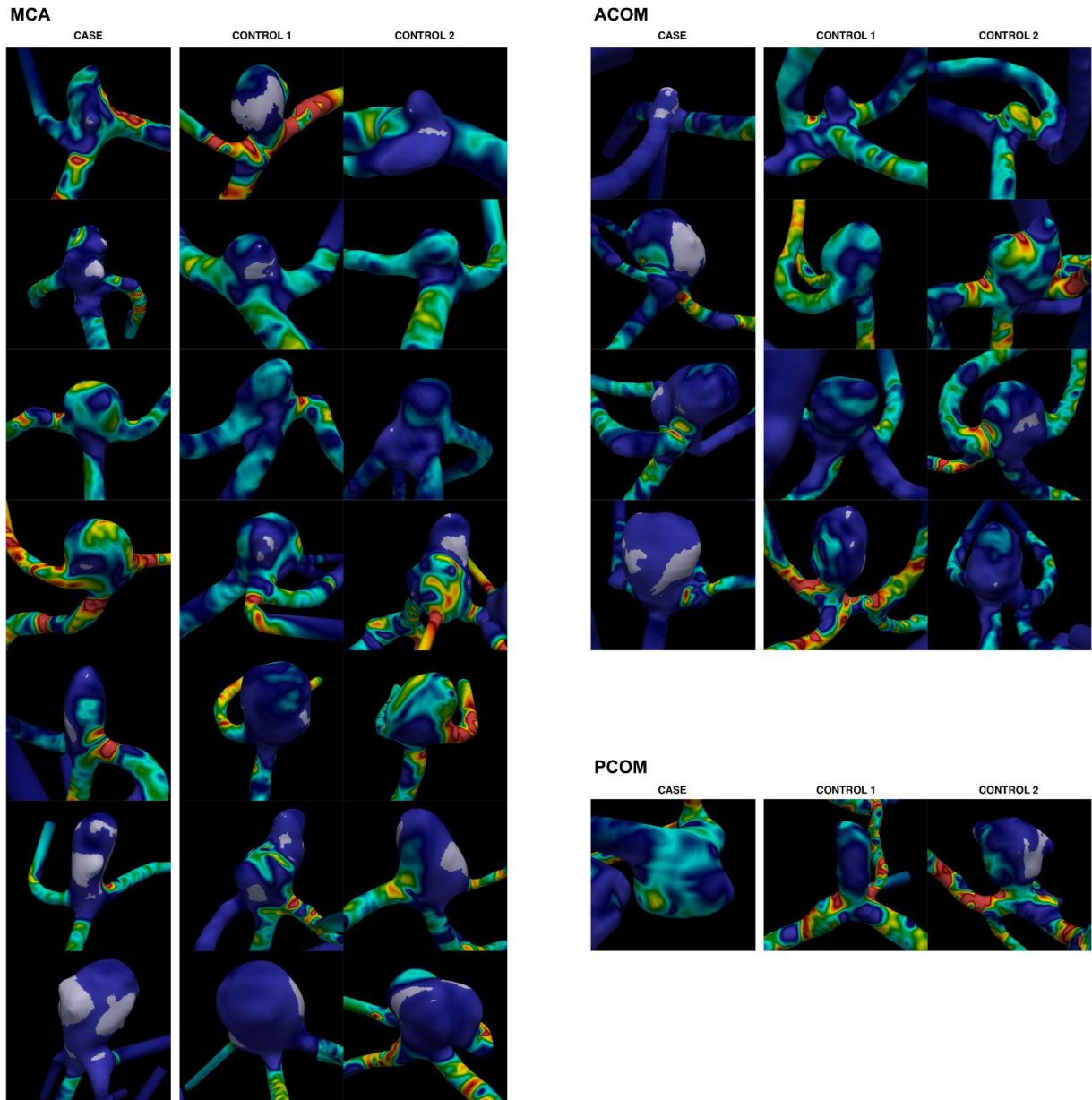


Figure 2. Visualization of wall shear stress (WSS) and low shear area (LSA) for all case and control aneurysms, grouped by location. WSS is represented by a color scale from blue for $WSS < 1.0$ Pa, to red for $WSS > 10$ Pa. Areas of low shear are colored gray, and represent areas of the dome where the average WSS is below 10 % of the average WSS in the parent artery. ACOM indicates anterior communicating artery; MCA, middle cerebral artery; PCOM, posterior communicating artery.

In the univariate analysis, low shear area (LSA) was the only parameter statistically significantly associated with future rupture ($P=0.041$) (Table). Minimal logarithmic WSS, averaged logarithmic WSS, pressure loss coefficient (PLc) and inflow concentration index (ICI) showed a tendency of being associated with rupture (P -values 0.09, 0.14, 0.15 and 0.18, respectively). Figure 1 shows the distribution of these five parameters for cases and controls, and Figure 2 visualizes WSS and LSA for all case and control aneurysms.

In the multivariable analysis, LSA ($\beta=8.72$ [95% confidence interval (CI), 0.85-16.59], $P=0.030$) and ICI ($\beta=1.13$ [95% CI, -0.30-2.55], $P=0.12$) were retained in the conditional logistic regression model. Their P -values remained almost constant when adjusting for the matching variables patient sex, age, aneurysm location and size (data not shown).

Discussion

In this study, we found significantly higher LSA in unruptured aneurysms that later ruptured than in rigorously matched aneurysms that did not rupture. A possible explanation is that low or stagnant blood flow causes an inflammatory response in the vascular wall, promoting atherogenesis and leukocyte infiltration.¹³

Our findings are in accordance with other studies indicating that hemodynamic parameters might predict rupture. Takao et al. found lower PLc in all aneurysms that later ruptured, and lower minimum WSS in a subgroup of these.⁷ Duan et al. observed larger LSA and lower normalized WSS in aneurysms that later ruptured.⁸ Sforza et al. found that increased shear concentration index, low shear ratio, viscous dissipation ratio and vorticity ratio, and a trend

toward elevated LSA, was associated with aneurysm growth and instability.¹⁴ None of these studies were matched both on patient and clinical characteristics.

The study has certain limitations. First, though matching can control for known confounders and increase power, generalizability can be decreased. Second, whether any of the control aneurysms would eventually rupture during further follow-up, causing a dilution bias in which effect sizes are larger in general aneurysm-patients than in our study sample, is unknown. Third, the segmentation process introduces uncertainty, and the computational simulation depends on assumptions of given boundary conditions, fixed walls and rheology model, as well as the numerical methods used.¹⁵

Despite limitations, this study presents long-awaited data from a rare patient material. Larger studies with patient-specific input variables are necessary for more conclusive rupture prediction.

Acknowledgments

We thank valuable coworkers at each institution participating in data collection, discussions and suggestions.

Sources of Funding

Northern Norway Regional Health Authority and UIT The Arctic University of Norway funded the study.

Disclosures

None.

References

1. van Gijn J, Rinkel GJ. Subarachnoid haemorrhage: diagnosis, causes and management. *Brain : a journal of neurology*. 2001;124:249-278
2. Vlak MH, Algra A, Brandenburg R, Rinkel GJ. Prevalence of unruptured intracranial aneurysms, with emphasis on sex, age, comorbidity, country, and time period: a systematic review and meta-analysis. *Lancet neurology*. 2011;10:626-636
3. Can A, Du R. Association of Hemodynamic Factors With Intracranial Aneurysm Formation and Rupture: Systematic Review and Meta-analysis. *Neurosurgery*. 2016;78:510-520
4. Rahman M, Ogilvy CS, Zipfel GJ, Derdeyn CP, Siddiqui AH, Bulsara KR, et al. Unruptured cerebral aneurysms do not shrink when they rupture: multicenter collaborative aneurysm study group. *Neurosurgery*. 2011;68:155-160; discussion 160-151
5. Schneiders JJ, Marquering HA, van den Berg R, VanBavel E, Velthuis B, Rinkel GJ, et al. Rupture-associated changes of cerebral aneurysm geometry: high-resolution 3D imaging before and after rupture. *AJNR. American journal of neuroradiology*. 2014;35:1358-1362
6. Kono K, Tomura N, Yoshimura R, Terada T. Changes in wall shear stress magnitude after aneurysm rupture. *Acta neurochirurgica*. 2013;155:1559-1563
7. Takao H, Murayama Y, Otsuka S, Qian Y, Mohamed A, Masuda S, et al. Hemodynamic differences between unruptured and ruptured intracranial aneurysms during observation. *Stroke; a journal of cerebral circulation*. 2012;43:1436-1439
8. Duan G, Lv N, Yin J, Xu J, Hong B, Xu Y, et al. Morphological and hemodynamic analysis of posterior communicating artery aneurysms prone to

rupture: a matched case-control study. *Journal of neurointerventional surgery*. 2016;8:47-51

9. Pereira VM, Brina O, Bijlenga P, Bouillot P, Narata AP, Schaller K, et al. Wall shear stress distribution of small aneurysms prone to rupture: a case-control study. *Stroke; a journal of cerebral circulation*. 2014;45:261-264
10. Liu J, Fan J, Xiang J, Zhang Y, Yang X. Hemodynamic characteristics of large unruptured internal carotid artery aneurysms prior to rupture: a case control study. *Journal of neurointerventional surgery*. 2016;8:367-372
11. Lauric A, Hippelheuser J, Cohen AD, Kadasi LM, Malek AM. Wall shear stress association with rupture status in volume matched sidewall aneurysms. *Journal of neurointerventional surgery*. 2014;6:466-473
12. Lindekleiv H, Sandvei MS, Romundstad PR, Wilsgaard T, Njolstad I, Ingebrigtsen T, et al. Joint effect of modifiable risk factors on the risk of aneurysmal subarachnoid hemorrhage: a cohort study. *Stroke; a journal of cerebral circulation*. 2012;43:1885-1889
13. Meng H, Tutino VM, Xiang J, Siddiqui A. High WSS or low WSS? Complex interactions of hemodynamics with intracranial aneurysm initiation, growth, and rupture: toward a unifying hypothesis. *AJNR. American journal of neuroradiology*. 2014;35:1254-1262
14. Sforza DM, Kono K, Tateshima S, Vinuela F, Putman C, Cebal JR. Hemodynamics in growing and stable cerebral aneurysms. *Journal of neurointerventional surgery*. 2016;8:407-412
15. Valen-Sendstad K, Steinman DA. Mind the gap: impact of computational fluid dynamics solution strategy on prediction of intracranial aneurysm hemodynamics and rupture status indicators. *AJNR. American journal of neuroradiology*. 2014;35:536-543

Appendix

Supplemental Methods	13
<i>Patient Selection</i>	13
<i>Background for the use of Computational Fluid Dynamics</i>	14
<i>Computational Simulation</i>	15
<i>Parameter Definitions</i>	19
Supplemental Results	20
<i>Study Population and Case Matching</i>	20
References	21

Supplemental Methods

Patient Selection

We searched electronic health records using codes from the International Classification of Diseases, version 10 (ICD-10), for patients diagnosed with nonruptured CA, code I67.1, between October 1, 2003 and October 1, 2013.

For cases, we identified CA patients from the four hospitals that were hospitalized with I60.0-I60.9 (non-traumatic subarachnoid hemorrhage) after I67.1. For controls, we identified CA patients from one of the hospitals, that were not subsequently registered with codes corresponding to SAH (I60.0-I60.9), nor surgical or endovascular prophylactic aneurysm treatment codes (Nordic Medico-Statistical Committee Classification of Surgical Procedures (NCSP) codes AAC00, AAC10, AAC15, AAL00 and AAL99).

For the identified patients, we appraised their electronic health records to verify that right codes were registered. The initial matching factor was location; if this factor could not be matched, the patient was excluded. Further matching was done in the following order: Aneurysm size, patient sex, and patient age.

We recorded date of birth, date of diagnosis for unruptured aneurysm, aneurysm location and parent artery relation (bifurcation/sidewall aneurysm), date admitted for SAH for cases, the reason for the aneurysm being conservatively managed, and known risk factors for SAH such as

hypertension, smoking, connective tissue disease, polycystic kidney disease, family history or prior SAH. We retrieved the first available cerebral angiography of each patient. Patients were excluded if they had previous treatment of the aneurysm of interest, or if the image quality precluded segmentation. Furthermore, cases were excluded if they had multiple aneurysms of which the ruptured aneurysm was difficult to identify, and controls were excluded if they died from an unknown cause during follow-up.

Background for the use of Computational Fluid Dynamics

Hemodynamics have received increasing attention as a possible way of discriminating ruptured aneurysms from unruptured aneurysms. This has typically been done using computational fluid dynamics (CFD).¹⁻⁵ The main focus has been on the tangential traction on the wall, the wall shear stress (WSS), due to its proven effect on the endothelium⁶ and its role in the pathophysiology of cardiovascular diseases such as atherosclerosis.⁷ This has resulted in numerous hemodynamic indicators, such as the average WSS, the oscillatory shear index (OSI) and area of low shear (LSA). Other indicators have also been related to the flow phenotype,⁸ such as the inflow concentration index (ICI) and the viscous dissipation ratio (VDR).²

Because of the unavoidable assumptions that needs to be made when modeling the aneurysmal blood flow, several studies have been done to investigate the effects of these assumptions. The typical assumption of Newtonian viscosity of blood have been shown to be sufficient in the

current paradigm,^{9, 10} as have the simplification of assuming the walls to be rigid.¹¹ The lack of patient specific boundary conditions has been highlighted as a main source of error in computational studies,¹² and also how to account for intercohort variability. This has been addressed by e.g. Valen-Sendstad et al, who propose inlet flow rates to be scaled with the area in the internal carotid artery.¹³ The outlet boundary conditions are also known to be a source of error, where many possible choices are possible, including resistance boundary conditions, traction free outlet, or prescribing flow at the outlets following the principle of minimal work (Murray's law). Several indicators have been shown to have a strong correlation under varying boundary conditions.⁹ Furthermore, increased complexity in the model leads to additional parameters, not readily available, or “may come with sufficiently large uncertainties as to render any perceived improvement in the predictive capability of the hemodynamic model”.¹¹

Computational Simulation

The simulations performed in this study were performed on the Abel Cluster (project NN9279K), owned by the University of Oslo and the Norwegian metacenter for High Performance Computing (NOTUR), and operated by the Department for Research Computing at USIT, the University of Oslo IT-department (<http://www.hpc.uio.no/>). Segmentation and meshing was performed using the Vascular Modeling ToolKit (<http://www.vmtk.org>).

Segmentation

All geometries were segmented from MRA or CTA images to include the ICA and/or basilar artery upstream of the aneurysm, and cylindrical extensions were added to both inlets and outlets. In cases where the segmentation process failed to include arteries visible on the original angiography, these arteries were created manually and attached to the segmented models.

Meshing

The meshing was done adaptively, with the mesh being finest in the vicinity of the aneurysm, where the distance between mesh nodes are approximately 0.135 mm, increasing to approximately 0.25 mm in the remote parts of the domain. In addition, we added four boundary layers to properly resolve the velocity gradients at the wall, with a total thickness of half the average nodal distance, and a thickness factor of 0.6 between the layers. In addition, the meshing was done radius-adaptive, to ensure a sufficient resolution even in the smallest segmented vessels.

Simulation

The Navier-Stokes equations were solved using the open source software packages cbcflow and cbcpost. As reported in the main Methods section, the software packages relied on the open source finite element library FEniCS.¹⁴ The equations were solved using piecewise linear approximation of the pressure, and quadratic approximations of the velocity, effectively halving the nodal distance. The equivalent mesh sizes¹⁵ ranged from 6.4 million to 62 million linear tetrahedral elements.

We imposed a fully developed pulsatile Womersley flow profile at the model inlets at a heart rate of 63 bpm, obtained from Hoi et al.¹⁶ The flow rate was scaled with the area¹³ with a mean velocity of 36.5 cm/s, to obtain a mean flow rate of 245 ml/min (± 100 ml/min).¹⁶ At the outlets, we scaled the flow according to the principle of minimal work (Murray's law). In segmented models where the posterior communicating artery (PCOM) was not merged to the posterior circulation, we assumed zero flux. Walls were assumed rigid and impermeable. We assumed blood to behave as a Newtonian fluid with a viscosity of 0.00345 Pa·s and a density of 1060 kg/m³.⁹ The Navier-Stokes simulation equations were solved and postprocessed with the open source softwares cbcflow and cbcpost (https://bitbucket.orgsimula_cbc/), based on the open source finite element library (FEniCS).¹⁴ To properly resolve the high frequency flow dynamics, we resolved the simulations with a temporal resolution of 0.04 milliseconds.

Table I. Definitions and Explanations of the Studied Hemodynamic Parameters.

Parameter name (Abbreviation)	Definition	Explanation
Time- and space-averaged WSS (AWSS)	$\frac{1}{A_a} \int_{\Gamma_a} \bar{\boldsymbol{\tau}} dS$	Average magnitude of the time-averaged WSS over the aneurysm wall. ^{1, 2}
Maximum WSS (MWSS)	$\max_{x \in \Gamma_a} \bar{\boldsymbol{\tau}} $	The maximal time-averaged WSS in the aneurysm dome. ^{1, 2}
Minimum WSS (MinWSS)	$\min_{x \in \Gamma_a} \bar{\boldsymbol{\tau}} $	The minimal time-averaged WSS in the aneurysm dome.
Logarithmic WSS (LnWSS)	$\frac{1}{A_a} \int_{\Gamma_a} \overline{\ln \boldsymbol{\tau} } dS$	Time-and space average logarithmic WSS magnitude over the aneurysm wall. ¹⁷
Min. logarithmic WSS (MinLnWSS)	$\min_{x \in \Gamma_a} \overline{\ln \boldsymbol{\tau} }$	Minimal time-averaged logarithmic WSS in the aneurysm. ¹⁷
Oscillatory shear index (OSI)	$\frac{1}{A_a} \int_{\Gamma_a} \frac{1}{2} \left(1 - \frac{ \bar{\boldsymbol{\tau}} }{ \boldsymbol{\tau} } \right) dS$	Measurement of the directional change of the WSS vector, averaged over the aneurysm dome. ¹
Low shear area (LSA)	$\frac{1}{A_a} \int_{\Gamma_a} \begin{cases} 1, \text{ if } \bar{\boldsymbol{\tau}} < 0.1 \text{AWSS}_{pa} \\ 0, \text{ otherwise} \end{cases} dS$	Areas of the aneurysm wall exposed to a WSS below 10% of the mean parent arterial WSS, normalized by dome area. ¹ AWSS _{pa} is computed as AWSS, over the parent artery domain.
Pressure loss coefficient (PLC)	$\overline{\left(\frac{(\frac{1}{2}\rho \mathbf{u}_{in} ^2 + p_{in}) - (\frac{1}{2}\rho \mathbf{u}_{out} ^2 + p_{out})}{(\frac{1}{2}\rho \mathbf{u}_{in} ^2)} \right)}$	Pressure loss associated with the aneurysm domain, relative to the kinetic energy in the parent artery. ⁴
Inflow concentration index (ICI)	$\overline{\left(\frac{Q_{in}/Q_{pa}}{A_{in}/A_{neck}} \right)}$	Concentration of inflow into the aneurysm, relative to the flow rate in the parent artery. ²
Shear concentration index (SCI)	$\overline{\left(\frac{F_h/F_a}{A_h/A_a} \right)}$	Amount of shear that is concentrated in the high-shear region of the aneurysm dome. ²
Viscous dissipation ratio (VDR)	$\overline{\left(\frac{\frac{1}{V_a} \int_{\Omega_a} 2\nu \boldsymbol{\varepsilon} ^2 dV}{\frac{1}{V_{nv}} \int_{\Omega_{nv}} 2\nu \boldsymbol{\varepsilon} ^2 dV} \right)}$	Amount of energy dissipation in the aneurysm domain, relative to the energy dissipation in the near vessel domain. ²

$\boldsymbol{\tau}$ indicates instantaneous wall shear stress vector; $\bar{\cdot}$, a time-averaged quantity over one heartbeat; Γ_a , the aneurysm wall with corresponding area A_a ; $|\cdot|$, a vector magnitude; \mathbf{u}_{in}/p_{in} , the velocity/pressure in the plane one diameter upstream from the aneurysm; \mathbf{u}_{out}/p_{out} , the velocity/pressure in the plane one diameter downstream from the aneurysm; Q_{in} , the flow into the aneurysm; Q_{pa} , the parent artery flow rate; A_{in} , the area of inflow into the aneurysm; A_{neck} , the total neck area; A_h , the area of high shear (1 SD above the average WSS in the near vessel domain); F_h , the total shear over A_h ; F_a , the total shear over the aneurysm; Ω_a , the aneurysm domain with corresponding volume V_a ; Ω_{nv} , the near vessel domain (<1cm from the aneurysm) with corresponding volume V_{nv} ; ν , the kinematic viscosity; $\boldsymbol{\varepsilon}$, the strain-rate tensor; and $\|\cdot\|$, the Frobenius norm.

Table II. Comparison of Baseline Characteristics Between Cases and Matched Controls *

	Cases (<i>n</i> = 12) no. (%)	Controls (<i>n</i> = 24) no. (%)	<i>P</i> -value †
Patient Characteristics			
Sex, male	4 (33.3)	9 (37.5)	0.81 ‡
Age (y), mean (±SD)	64.4 (8.9)	63.5 (10.1)	0.80 ‡
Current smoker	6 (50)	10 (41.7)	0.64
Medical history			
Hypertension	9 (75.0)	19 (79.2)	0.08
Family history of aneurysms or SAH	1 (8.3)	3 (12.5)	0.71
Previous SAH	1 (8.3)	0 (0.0)	0.15
Multiple aneurysms	3 (25.0)	8 (33.3)	0.61
Treatment of another aneurysm	1 (8.3)	1 (4.2)	0.61
Median time from diagnosis to SAH or end of follow-up, y (IQR)	3.4 (1.6-6.3)	4.5 (3.7-8.2)	N/A
Aneurysm Characteristics			
Location			1.0 ‡
Anterior communicating artery	4 (33.3)	8 (33.3)	
Middle cerebral artery	7 (58.3)	14 (58.3)	
Posterior communicating artery	1 (8.3)	2 (8.3)	
Maximal diameter (mm), mean (±SD)	8.34 (3.41)	8.15 (3.40)	0.87 ‡
Volume (mm ³), mean (±SD)	177.9 (219.4)	168.8 (250.8)	0.92 ‡

SAH indicates subarachnoid hemorrhage; SD, standard deviation; and IQR, interquartile range.

* Continuous, parametric variables are reported as mean ± standard deviation. Continuous, non-parametric variables are reported as median (interquartile range). Dichotomous and categorical variables are reported as *n* (per cent)

† A *P*-value of < 0.05 was considered statistically significant.

‡ Matched variables.

Parameter Definitions

Table I specifies abbreviations, mathematical definitions and pragmatic explanations for each studied parameter. Oscillatory shear index (OSI) and low shear area (LSA) are derivatives of wall

shear stress (WSS).⁶ Pressure loss coefficient (PLc), inflow concentration index (ICI) and viscous dissipation rate (VDR) are related to the flow phenotype.^{4, 8}

Supplemental Results

Study Population and Case Matching

The initial search identified 43 patients with confirmed aneurysmal subarachnoid hemorrhage, originating from saccular aneurysms that were known prior to rupture and had been treated conservatively. 20 cases were excluded because matching was not accomplished, of which 18 had aneurysms larger than 10 mm. Eight cases were excluded because of insufficient image quality, and three cases were excluded because of insufficient image quality in the available controls. Each of the remaining 12 patients were successfully matched to two control patients with a confirmed saccular CA that neither was treated nor ruptured during follow-up.

Table II provides baseline characteristics of cases and matched controls.

References

1. Xiang J, Natarajan SK, Tremmel M, Ma D, Mocco J, Hopkins LN, et al. Hemodynamic-morphologic discriminants for intracranial aneurysm rupture. *Stroke; a journal of cerebral circulation*. 2011;42:144-152
2. Cebal JR, Mut F, Weir J, Putman C. Quantitative characterization of the hemodynamic environment in ruptured and unruptured brain aneurysms. *AJNR. American journal of neuroradiology*. 2011;32:145-151
3. Shojima M, Oshima M, Takagi K, Torii R, Hayakawa M, Katada K, et al. Magnitude and role of wall shear stress on cerebral aneurysm: Computational fluid dynamic study of 20 middle cerebral artery aneurysms. *Stroke; a journal of cerebral circulation*. 2004;35:2500-2505
4. Takao H, Murayama Y, Otsuka S, Qian Y, Mohamed A, Masuda S, et al. Hemodynamic differences between unruptured and ruptured intracranial aneurysms during observation. *Stroke; a journal of cerebral circulation*. 2012;43:1436-1439
5. Miura Y, Ishida F, Umeda Y, Tanemura H, Suzuki H, Matsushima S, et al. Low wall shear stress is independently associated with the rupture status of middle cerebral artery aneurysms. *Stroke; a journal of cerebral circulation*. 2013;44:519-521
6. Chien S. Mechanotransduction and endothelial cell homeostasis: The wisdom of the cell. *American journal of physiology. Heart and circulatory physiology*. 2007;292:H1209-1224
7. Malek AM, Alper SL, Izumo S. Hemodynamic shear stress and its role in atherosclerosis. *JAMA : the journal of the American Medical Association*. 1999;282:2035-2042
8. Cebal JR, Castro MA, Burgess JE, Pergolizzi RS, Sheridan MJ, Putman CM. Characterization of cerebral aneurysms for assessing risk of rupture by using patient-specific computational hemodynamics models. *AJNR. American journal of neuroradiology*. 2005;26:2550-2559
9. Evju O, Valen-Sendstad K, Mardal KA. A study of wall shear stress in 12 aneurysms with respect to different viscosity models and flow conditions. *Journal of biomechanics*. 2013;46:2802-2808
10. Castro MA, Ahumada Olivares MC, Putman CM, Cebal JR. Unsteady wall shear stress analysis from image-based computational fluid dynamic aneurysm models under newtonian and casson rheological models. *Medical & biological engineering & computing*. 2014;52:827-839

11. Steinman DA. Assumptions in modelling of large artery hemodynamics. In: Ambrosi D, Quarteroni A, Rozza G, eds. *Modeling of physiological flows*. Milano: Springer Milan; 2012:1-18.
12. Kallmes DF. Point: CFD--computational fluid dynamics or confounding factor dissemination. *AJNR. American journal of neuroradiology*. 2012;33:395-396
13. Valen-Sendstad K, Piccinelli M, KrishnankuttyRema R, Steinman DA. Estimation of inlet flow rates for image-based aneurysm CFD models: Where and how to begin? *Annals of biomedical engineering*. 2015;43:1422-1431
14. Logg A, Mardal K-A, Wells GN, eds. *Automated solution of differential equations by the finite element method*. Springer Science+Business Media; 2012.
15. Valen-Sendstad K, Steinman DA. Mind the gap: Impact of computational fluid dynamics solution strategy on prediction of intracranial aneurysm hemodynamics and rupture status indicators. *AJNR. American journal of neuroradiology*. 2014;35:536-543
16. Hoi Y, Wasserman BA, Xie YJ, Najjar SS, Ferruci L, Lakatta EG, et al. Characterization of volumetric flow rate waveforms at the carotid bifurcations of older adults. *Physiological measurement*. 2010;31:291-302
17. Lauric A, Hippelheuser J, Cohen AD, Kadasi LM, Malek AM. Wall shear stress association with rupture status in volume matched sidewall aneurysms. *Journal of neurointerventional surgery*. 2014;6:466-473